

3D Reconstruction of Optical Diffraction Tomography Based on a Neural Network Model

THÈSE N° 8737 (2018)

PRÉSENTÉE LE 9 NOVEMBRE 2018

À LA FACULTÉ DES SCIENCES ET TECHNIQUES DE L'INGÉNIEUR

LABORATOIRE D'OPTIQUE

PROGRAMME DOCTORAL EN PHOTONIQUE

ÉCOLE POLYTECHNIQUE FÉDÉRALE DE LAUSANNE

POUR L'OBTENTION DU GRADE DE DOCTEUR ÈS SCIENCES

PAR

Morteza HASANI SHOREH

acceptée sur proposition du jury:

Prof. C. Moser, président du jury

Prof. D. Psaltis, directeur de thèse

Prof. C. Sheppard, rapporteur

Dr Y. Cotte, rapporteur

Prof. M. Unser, rapporteur



ÉCOLE POLYTECHNIQUE
FÉDÉRALE DE LAUSANNE

Suisse
2018

Acknowledgements

I would like to thank the following people who contributed to the success of this work:

- My thesis advisor, Prof. Demetri Psaltis, for giving me the opportunity to learn the job of a researcher in a dynamic team. During these three years, Prof. Psaltis gave me numerous ideas, some of which have evolved into fruitful projects.
- My parents, siblings and especially my beloved wife who helped me a lot for preparation of this thesis,
- Phelps Edward Allen, Valérian CR Dormoy, Marcin Zielinski and Thomas Lanvin for sample preparation,
- Ulugbek Kamilov, Ioannis Papadopoulos, Nicolino Stasio, Donald Conkey, Ye Pu, Gregoire Laporte, Ahmed Bassam, JooWon Lim, Mohammad Hashemi, Elizabeth Antoine, Pooria Hadikhani, Eirini Kakkava and Marilisa Romito for their helpful suggestions, helping in projects and their teaching of tools and devices usage,
- Carole Berthet, Silke Jan and Anne De Witte for their help in administrative tasks,
- Michael Unser, YongKeun (Paul) Park and Kyoohyun Kim for providing the code and assistance for optical diffraction tomography,
- All jury members for their keen ideas and helpful suggestions

I thank also all my colleagues and friends with whom I had fruitful discussions that contributed to stimulate my interest in research.

Resumé

La tomographie optique a été largement étudiée pour des applications d'imagerie biomédicale. Au cours des dernières années, il a été combiné avec l'holographie numérique et a été utilisé pour produire des images de haute qualité d'objets de phase tels que des cellules. Dans cette thèse, nous examinons certaines des techniques les plus récentes de tomographie par diffraction pour résoudre les problèmes de reconstruction tridimensionnelle (3D) et discutons et comparons certaines des idées et des articles les plus importants. Ensuite, nous proposons un algorithme basé sur un réseau neuronal pour résoudre ce problème et l'appliquer sur des échantillons synthétiques et biologiques. La tomographie en phase conventionnelle avec un enregistrement de lumière cohérente et hors axe est effectuée. La méthode de propagation par faisceau (BPM) est utilisée pour modéliser la diffusion et chaque plan x-y est modélisé par une couche de neurones dans le MPM. La sortie du réseau (données simulées) est comparée aux mesures expérimentales et l'erreur est utilisée pour corriger les poids des neurones (indices de réfraction des nœuds) en utilisant des techniques standards de rétropropagation d'erreur. L'algorithme proposé est détaillé et étudié. Ensuite, nous examinons la régularisation conservatrice de la résolution et discutons d'une méthode de sélection des paramètres de régularisation. En outre, les minima locaux et les problèmes de déballage de phase sont discutés et les moyens de les éviter sont étudiés. Il est montré que la tomographie d'apprentissage proposée (LT) atteint de meilleures performances que d'autres techniques telles que, DT en particulier lorsque nombre insuffisant ou un ensemble incomplet de mesures est disponible. Nous explorons également le rôle de la régularisation dans l'obtention d'images de plus haute fidélité sans perdre de résolution. Il a été montré expérimentalement qu'en raison du dépassement de la diffusion multiple, la reconstruction LT surpasse considérablement la DT lorsque l'échantillon contient deux ou plusieurs couches de cellules ou de billes. Ensuite, la reconstruction en utilisant des mesures d'intensité est étudiée. La reconstruction 3D d'une cellule vivante pendant l'apoptose est présentée dans un format temporel. À la fin, nous présentons une comparaison finale avec les principaux papiers et les systèmes disponibles dans le commerce. On montre que, par rapport à d'autres algorithmes existants, les résultats de la méthode proposée sont de meilleure qualité. En particulier, les structures granulaires parasites et l'artefact de cône manquant sont améliorés. Dans l'ensemble, les perspectives de notre approche sont assez riches pour l'imagerie tomographique à haute résolution dans une gamme d'applications pratiques.

mots clés: Tomographie par cohérence optique, reconstruction d'indice de réfraction 3D, réseau de neurones, microscopie interférentielle, imagerie biomédicale, holographie numérique, techniques de reconstruction d'image, méthode de propagation de faisceau, régularisation de variation totale, problèmes inverses, objets de phase 3D

Abstract

Optical tomography has been widely investigated for biomedical imaging applications. In recent years, it has been combined with digital holography and has been employed to produce high quality images of phase objects such as cells. In this Thesis, we look into some of the newest optical Diffraction Tomography (DT) based techniques to solve Three-Dimensional (3D) reconstruction problems and discuss and compare some of the leading ideas and papers. Then we propose a neural-network-based algorithm to solve this problem and apply it on both synthetic and biological samples. Conventional phase tomography with coherent light and off axis recording is performed. The Beam Propagation Method (BPM) is used to model scattering and each x-y plane is modeled by a layer of neurons in the BPM. The network's output (simulated data) is compared to the experimental measurements and the error is used for correcting the weights of the neurons (the refractive indices of the nodes) using standard error back-propagation techniques. The proposed algorithm is detailed and investigated. Then, we look into resolution-conserving regularization and discuss a method for selecting regularizing parameters. In addition, the local minima and phase unwrapping problems are discussed and ways of avoiding them are investigated. It is shown that the proposed learning tomography (LT) achieves better performance than other techniques such as, DT especially when insufficient number or incomplete set of measurements is available. We also explore the role of regularization in obtaining higher fidelity images without losing resolution. It is experimentally shown that due to overcoming multiple scattering, the LT reconstruction greatly outperforms the DT when the sample contains two or more layers of cells or beads. Then, reconstruction using intensity measurements is investigated. 3D reconstruction of a live cell during apoptosis is presented in a time-lapse format. At the end, we present a final comparison with leading papers and commercially available systems. It is shown that -compared to other existing algorithms- the results of the proposed method have better quality. In particular, parasitic granular structures and the missing cone artifact are improved. Overall, the perspectives of our approach are pretty rich for high-resolution tomographic imaging in a range of practical applications.

Keywords: Optical diffraction tomography, 3D refractive index reconstruction, neural network, interference microscopy, biomedical imaging, digital holography, image reconstruction techniques, beam propagation method, total variation regularization, inverse problems, 3D phase objects

Symbols and definitions

All the quantities are defined in SI system of units.

Mathematical notations

$\Delta_{\perp} = \frac{\partial^2}{\partial x^2} + \frac{\partial^2}{\partial y^2}$	transverse Laplacian in x and y
$\Delta = (\partial^2/\partial x^2 + \partial^2/\partial y^2 + \partial^2/\partial z^2)$	the Laplacian
$\mathcal{F}[f]$ and \tilde{f}	Fourier transform of f
$\mathcal{F}^{-1}[f]$	inverse Fourier transform of f

- We use the following definitions of the Fourier transform and its inverse:

$$F(\omega) = \int_{-\infty}^{\infty} f(t) e^{-j\omega t} dt, \quad f(t) = \frac{1}{2\pi} \int_{-\infty}^{\infty} F(\omega) e^{j\omega t} d\omega$$

- For discretized data, we define the fast Fourier transform $U_{pq} = \text{FFT}(u_{mn})$ as:

$$U_{pq} = \sum_{m=0}^{N_x-1} \sum_{n=0}^{N_y-1} u_{mn} \exp \left[-2\pi j \left(\frac{mp}{N_x} + \frac{nq}{N_y} \right) \right],$$

- The inverse transform is given by:

$$u_{mn} = \frac{1}{N_x N_y} \sum_{p=0}^{N_x-1} \sum_{q=0}^{N_y-1} U_{pq} \exp \left[2\pi j \left(\frac{mp}{N_x} + \frac{nq}{N_y} \right) \right],$$

where N_x and N_y are the number of mesh grid points, Δx and Δy are the step size and $L_x = N_x \Delta x$, $L_y = N_y \Delta y$ are the dimensions of the computation window in X and Y respectively.

- The discretized Fresnel diffraction kernel is:

$$e^{j\pi[(n_l^2 - n_{l+1}^2)\delta^2 + (m_l^2 - m_{l+1}^2)\delta^2] / \lambda \delta_z}$$

where n_l and m_l are integers and λ is the wavelength of light. δ is the sampling interval in the transverse coordinates (x, y) whereas δ_z is the sampling interval along the propagation direction z .

Electromagnetic quantities

ϵ_0	vacuum permittivity $\approx 8.8542 \cdot 10^{-12}$ F/m
c	speed of light in vacuum = 299,792,458 m/s

Optics-related quantities

λ_0	wavelength in vacuum [m]
λ	wavelength in the medium [m]
k_0	wave vector in vacuum [rad/m], $k_0 = 2\pi/\lambda_0$
k	wave vector in the medium [rad/m], $k = 2\pi/\lambda$
n	refractive index
n_0	linear refractive index as it appears in the optical Kerr law: $n = n_0 + n_2 I + n_4 I^2 + \dots$
I	light intensity [W/m ²], $I = \frac{ \mathbf{E} ^2}{2\eta}$

- In the context of waves propagation, the z coordinate corresponds to the direction of propagation, which is usually the optical axis in microscopy. We use the following convention for the harmonic dependence of wave: $\exp[i(kz - \omega t)]$. We consider that the phase increases with z .

Acronyms

3D	Three-Dimensional
BPM	Beam Propagation Method
CMOS	Complementary Metal-Oxide-Semiconductor
DFT	Discrete Fourier Transform
DPS	Dispersion-relation Phase Spectroscopy
DT	Diffraction Tomography
FBP	Filtered Back-Projection
FTIR	Fourier Transform InfraRed
FTLS	Fourier Transform Light Scattering
GA	Goldstein's Algorithm
IRLS	Iteratively Reweighted Least-Squares
IRTV	Iteratively Reweighted Total Variation
ISAM	Interferometric Synthetic Aperture Microscopy
LS	Least-Squares
LT	Learning Tomography
LCI	Low-Coherence Interferometry
MCF7	Michigan Cancer Foundation seven
NA	Numerical Aperture
OCT	Optical Coherence Tomography
PBS	Phosphate Buffer Saline
QPI	Quantitative Phase Imaging
RTPM	Regularized Tomographic Phase Microscope
SLIM	Spatial Light Interference Microscopy
SLM	Spatial Light Modulator
SNR	Signal to Noise Ratio
SSF	Split-Step Fourier
TDM	Tomographic Diffractive Microscopy
TPM	Tomographic Phase Microscopy
TV	Total Variation
WDT	White-light Diffraction Tomography

Contents

1	Introduction	1
1.1	Structure	1
1.2	Contribution	4
1.3	Journal publications	4
2	Literature Review	5
2.1	Literature review	5
2.2	Recently proposed methods	8
2.3	Bibliography	14
3	Proposed Method	17
3.1	Introduction	17
3.2	Experimental setup	18
3.3	Methodology	19
3.4	Results	21
3.5	Discussions and conclusions	28
3.6	Bibliography	28
4	Algorithm	31
4.1	Introduction	31
4.2	Forward model	33
4.2.1	Fourier beam-propagation	34
4.2.2	Numerical implementation	34
4.3	Proposed method	35
4.3.1	Problem formulation	37
4.3.2	Computation of the gradient	38
4.3.3	Iterative reconstruction	40
4.4	Numerical evaluation	41
4.5	Conclusion	47
4.6	Bibliography	48
5	Imaging Thick Samples	51
5.1	Introduction	51
5.2	Experimental apparatus and sample preparation	53
5.3	Results	54
5.4	Conclusion	58
5.5	Bibliography	60

6	Initialization, Local Minima and Phase Unwrapping	63
6.1	Initialization and local minima	63
6.2	Phase unwrapping	67
6.3	Conclusion	70
6.4	Bibliography	70
7	Multiple Scattering	73
7.1	Introduction	73
7.2	Results	74
7.3	Conclusion	78
7.4	Bibliography	78
8	Other Results and Comparisons	79
8.1	Intensity measurments	79
8.2	3D movie reconstruction	80
8.3	Comparison with existing imaging techniques	82
8.4	Comparing with commercially available imaging techniques	85
8.5	Comparison of computation costs	87
8.6	Conclusion	89
8.7	Bibliography	89
9	Conclusions and Future Works	91
9.1	Conclusions	92
9.2	Future works	93
A	Appendix	95
A.1	Comparison between different methods	95
A.1.1	Limited angles reconstruction	95
A.2	Fourier Beam-Propagation Method	98
A.2.1	Paraxial Helmholtz equation	99
A.2.2	Fourier beam-propagation	100
A.3	Total variation minimization	101
A.3.1	Two variants of TV	102
A.3.2	Minimization of TV	103
A.4	Bibliography	105

Introduction

Contents

1.1 Structure	1
1.2 Contribution	4
1.3 Journal publications	4

In this Thesis, we propose a neural-network-inspired algorithm to solve Three-Dimensional (3D) tomographic reconstruction problems. We apply it on both synthetic and biological samples using conventional phase tomography with coherent light and off axis recording. The Beam Propagation Method (BPM) is used to model scattering and each x-y plane is modeled by a layer of “*neurons*” in the BPM. The network’s output (simulated data) is compared to the experimental measurements (see Figure 1.1), and the error is used for correcting the weights of the neurons (the refractive indices of the nodes) using standard error back-propagation techniques. Resolution-conserving regularization, local minima and phase unwrapping problems are discussed and ways of avoiding them are investigated. The results show that the proposed learning tomography (LT) achieves better performance than other techniques such as, diffraction tomography (DT) especially with a smaller number of measurements or when the sample contains two or more layers of cells or beads. Also the role of regularization in obtaining higher fidelity images without losing resolution is explored. Reconstruction using only intensity measurements is investigated and discussed. 3D reconstruction of a live cell during apoptosis is presented in a time-lapse format. Finally, comparison with leading existing and commercially available devices is presented. In this chapter, the structure of the thesis is provided, contributions and collaborators are presented and related journal publications are listed.

1.1 Structure

The structure of the thesis is as follows:

The **First Chapter** provides an overview of the following chapters, their relationship and their contribution to the fulfillment of the desired goal.

Chapter 2 looks into some of the recent optical reconstruction techniques that exist in the technical literature, and discusses some of the leading ideas and papers.

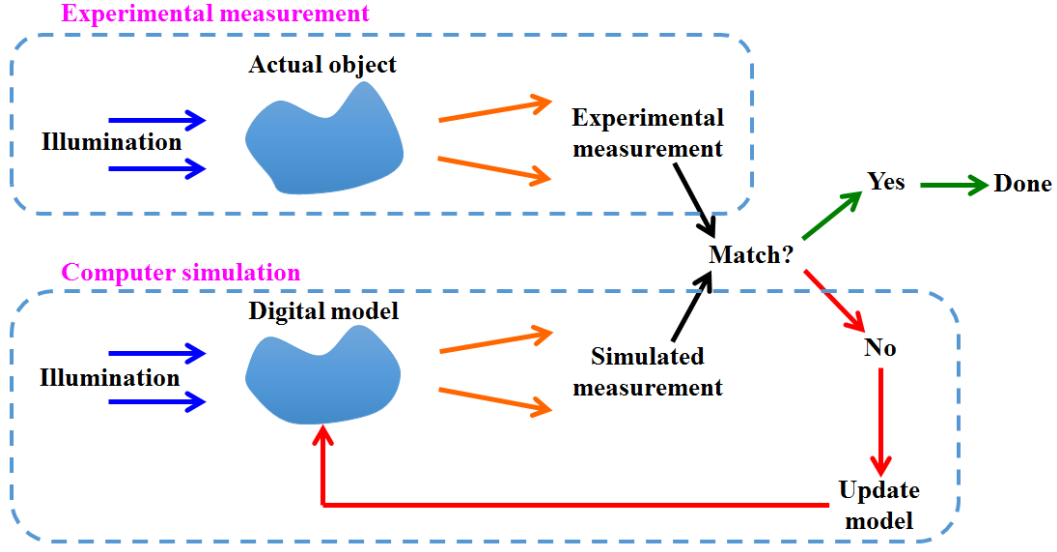


Figure 1.1: Schematic diagram of the proposed method

These are the state of the art existing algorithms which we are going to compare with ours and show that the results of our algorithm have better quality.

In **Chapter 3**, we describe a method for imaging 3D phase objects in a tomographic configuration implemented by training a neural network-like structure to reproduce the complex amplitude of the experimentally measured scattered light. The network is designed such that the voxel values of the refractive index of the 3D object are the variables that are adapted during the training process. We demonstrate the method experimentally by forming images of the 3D refractive index distribution of Hela cells. We show some primary results on cells and beads and compare them with some other leading techniques. The results of all comparisons show better performance of our proposed LT method.

Optical tomographic imaging requires an accurate forward model as well as regularization to mitigate missing-data artifacts and to suppress noise. Nonlinear forward models can provide more accurate interpretation of the measured data than their linear counterparts, but they generally result in computationally prohibitive reconstruction algorithms. Although sparsity-driven regularizers significantly improve the quality of the reconstructed image, they further increase the computational burden of imaging. In **Chapter 4**, we present the algorithm of a novel iterative imaging method for optical tomography that combines a nonlinear forward model based on the beam propagation method (BPM) with an edge-preserving 3D Total Variation (TV) regularizer. The central element of our approach is a time-reversal scheme, which allows for an efficient computation of the derivative of the transmitted wave-field with respect to the distribution of the refractive index. This time-reversal scheme together with our stochastic proximal-gradient algorithm makes it possible to optimize under a nonlinear forward model

in a computationally tractable way, thus enabling a high-quality imaging of the refractive index throughout the object. We demonstrate the effectiveness of our method through several experiments on simulated and experimentally measured data.

The vast majority of Optical Diffraction Tomography (ODT) experiments reported to date have been 3D images of single cells or beads demonstrating excellent image quality and sectioning capability. The sample thickness in these experiments is 10 to 20 μm and the accumulated phase is generally well below 2π . In **Chapter 5**, we explore ODT when the sample consists of multiple layers of cells. We assess experimentally the impact of sample thickness for the different ODT reconstruction algorithms and describe a strategy that allows us to image, for the first time, multi-cell clusters.

Since the energy function in LT is generally non-convex, the solution it obtains is not guaranteed to be globally optimal. In **Chapter 6**, we investigate the influence of the initialization on the convergence of the algorithm. In particular, we show that using initial condition is essential for high-quality imaging in strongly scattering scenarios. We present the landscape of the cost function between the estimated and true solutions showing the local minima problem for two different accumulated phase scenarios with and without regularization. We provide experimental results for different initialization and show their convergences. At the end, we look into the phase unwrapping problem and compare different phase unwrapping methods for an experimental data set.

In almost all microscopy techniques, including wide field and confocal imaging single scattering is assumed. This imposes strong limitations on the resolution that can be achieved, in particular, in biological tissues that are highly scattering. Learning-based algorithms for optical tomography have recently received significant attention from researchers as a way of taking into account multiple scattering. In **Chapter 7**, we experimentally demonstrate that LT can handle multiple scattering and show cases where linear methods such as DT fail. We compare the reconstruction of the two beads and cells stacked in z with the superposition of the individual ones added together which shows there is a significant left over due to multiple scattering for DT, whereas in the case of LT, the superposition of the individual reconstructions overlaps almost perfectly with the reconstruction of the two beads together.

In **Chapter 8**, the LT technique based on intensity measurements is investigated on the previously presented HeLa cells. Considering that the proposed method is based on phase contrast and does not use any kind of staining, it can be applied to analyze in-vivo cell behavior. To illustrate this, we investigate a live MCF7 cell blebbing as it is dying. Then we show some final comparisons with the existing techniques such as Born, Rytov, Refocused Rytov, as well as, the commercially available techniques such as fluorescent, reflection and transmission confocal. At the end, the complexity and cost of the proposed LT method is investigated and compared with existing methods.

Chapter 9 presents the conclusion of the results. Potential research and devel-

opment threads are discussed for the future studies. Some of these threads are being pursued by other Lab members.

1.2 Contribution

Some colleagues and collaborators (students and postdocs) must be credited for their collaboration in different studies presented here. The roles of these people are discussed below:

- **Chapter 3** originated from the original paper⁽¹⁾ coauthored with Ulugbek S. Kamilov and Ioannis N. Papadopoulos.
- **Chapter 4** reflects part of the published paper⁽²⁾ coauthored with Ulugbek S. Kamilov and Ioannis N. Papadopoulos.
- **Chapter 5** present results of another paper⁽³⁾ coauthored with Alexandre Goy.
- **Chapter 6-8** reports on other projects fulfilled with the help of Alexandre Goy.

1.3 Journal publications

1. Ulugbek S. Kamilov, Ioannis N. Papadopoulos, Morteza H. Shoreh, Alexandre Goy, Cedric Vonesch, Michael Unser, and Demetri Psaltis, "Learning approach to optical tomography," *Optica* 2, 517-522 (2015)
2. Ulugbek S. Kamilov, Ioannis N. Papadopoulos, Morteza H. Shoreh, Alexandre Goy, Cedric Vonesch, Michael Unser, and Demetri Psaltis, "Optical Tomographic Image Reconstruction Based on Beam Propagation and Sparse Regularization," in *IEEE Transactions on Computational Imaging*, vol. 2, no. 1, pp. 59-70, March 2016.
3. Alexandre Goy, Morteza H. Shoreh, JooWon Lim, Michael Unser, and Demetri Psaltis. "Imaging thick samples with optical tomography." arXiv preprint arXiv:1711.03714 (2017).
4. U. S. Kamilov, Ioannis N. Papadopoulos, Morteza H. Shoreh, Demetri Psaltis, and Michael Unser, "Isotropic inverse-problem approach for two-dimensional phase unwrapping," *J. Opt. Soc. Am. A* 32, 1092-1100 (2015)
5. JooWon Lim, Alexandre Goy, Morteza H. Shoreh, Michael Unser, and Demetri Psaltis. "Assessment of learning tomography using Mie theory." arXiv preprint arXiv:1705.10410 (2017).

Literature Review

Contents

2.1 Literature review	5
2.2 Recently proposed methods	8
2.3 Bibliography	14

In this chapter, we look into some of the newest optical reconstruction techniques in the technical literature, and discuss some of the base and leading ideas and papers in more details. These are the state of the art exiting algorithms which we are going to compare with ours and show that the results of our algorithm have better quality.

2.1 Literature review

The interaction of electromagnetic fields with inhomogeneous objects will change the wavefront and the amplitude of the field which is called scattering [1]. This scattered light carries information on both amplitude and phase. For weak scattering we can use first order Born approximation to describe the problem linearly, hence, the measurements of the scattered field can be used to reconstruct the object directly [1]. This is called the inverse scattering problem and is widely used to reconstruct the object in tomographic imaging techniques. The far field measurement data can be also used to solve inverse scattering problem. The first influential work for solving the inverse scattering problem was done by Bragg which was about X-ray diffraction [2]. Although it was used for determining crystal structures, the solution method is pretty close for both problems. However, in X-ray diffraction problem, achieving the phase information using field measurements is difficult, in other words, the reconstruction is non-unique which is known as "the phase problem" [3]. To overcome this problem some prior knowledge is used in an iterative manner to converges to an unambiguous solution [3].

In 1969, Wolf come up with a theoretical formulation to solve the inverse problem for tomographic imaging of phase objects [4]. Nowadays, Wolf's solution of the inverse problem is known as Optical Diffraction Tomography (ODT) [4]. One year later he comes up with another publication extracting complex amplitude distribution of scattered fields from the intensity [5] which makes it possible to calculate the exact refractive index distribution of the object. Recently, there are some publication on using ODT theory for 3D reconstruction of transparent objects

which clearly shows the experimental feasibility of scanning by rotating either the object or the source, and measuring in the far field [6–14]. Since this approach is based on laser illumination, due to speckle, it cannot be used to reach high contrast and resolution [15].

In [9], the authors present a microscopy technique for measuring the wavefront after it is scattered by an optically transparent microscopic object. They proposed a slice-by-slice object-scatter extraction algorithm to reduce the computational complexity. In [10], the Authors discussed the basic theory of Tomographic Diffractive Microscopy (TDM) using an electromagnetism framework and compared it with conventional widefield microscopes. Also various implementations of TDM are described and their resolution is compared. In [11], the authors report a technique for quantitative mapping of refractive index in 3D manner for live cells and tissues using interferometric microscope and illuminating in variable angles. The authors mostly focus on demonstrating time-dependent changes in cell structure using tomographic imaging. In [12], the authors proposed a Regularized Tomographic Phase Microscope (RTPM) to overcome lack of 3D resolution in conventional methods without losing the ability to observe a sample in its natural condition. In addition, they show chromosomal imaging illustrating the potential to determine the molecular composition of live cells. In [13], the inverse Radon transform is used to calculate three-dimensional refractive index distribution using transmission phase images with nanometric axial accuracy. In [14], the authors use non-invasive optical nanoscopy to achieve a lateral resolution of 90 nm which is achieved using a quasi- 2π -holographic detection scheme and complex deconvolution.

In 1991, Huang et al. used Low-Coherence Interferometry (LCI) based tomography known as OCT [16–18] for imaging tissues. In OCT, the sample is imaged at a depth specified by the reference of the interferometer, hence the axial resolution is determined by the coherence length of the source rather than the numerical aperture (NA) of the objectives [18]. To maximize the depth of imaging, OCT systems employ low NA objectives therefore tend to have poor lateral resolution. By adjusting the delay of the reference field we obtain the depth information, and using raster scanning the transverse information is obtained. Specially, having low temporal coherence in OCT is useful for removing the scattered light outside the region of interest which reduces the degrading effect caused by the interference. OCT systems use intensity-based measurements of the light which is backscattered from various depths to gain information about the 3D object structure. In 2006, Ralston et al. try to solve the inverse scattering problem by developing a computational technique using the amplitude and phase of the OCT data [19]. This method which is called Interferometric Synthetic Aperture Microscopy (ISAM) improves the lateral resolution and makes it possible to maintain it across the whole OCT imaging volume [19].

Quantitative Phase Imaging (QPI) [20] which combines holography method proposed by Gabor in 1948 [21] and phase sensitive microscopy proposed by Zernike [22, 23] is getting more and more attention. Holography measures the interference between reference field and the main scattered field instead of the in-

tensity to record phase information. Modifications of the main field contain quantitative information about the phase difference caused by the sample at each point in space, hence, allows us to measure the complex scattered field. Recent advances in light sources and detectors providing sufficient pixel counts, high acquisition speed, and enough light sensitivity to acquire images help the growth of QPI applications. These advances cause significant improvement in solving the inverse problem because they allow us to work with the complex field itself not just the intensity [24, 25].

The earliest idea of using digital Fourier holography for measuring the angular light scattering spectrum and reconstructing object using that was proposed by Alexandrov et al, in 2005 [26]. In 2008, Ding et al. proposed the applications of QPI to inverse scattering problems [27]. This method is the spatial equivalent of Fourier Transform InfraRed (FTIR) spectroscopy, hence it is called Fourier Transform Light Scattering (FTLS). In FTLS, the angular scattering information is obtained by taking the numerical Fourier transform of spatial-domain complex field measurement but in FTIR time-domain measurements are used to do that. Therefore, using quantitative phase images for studying inhomogeneous and dynamic media makes this method ultrasensitive [27]. Considering the fact that the technique is based on imaging not scattering measurements, all the scattering angles and every spatial frequency are measured simultaneously at each point, resulting in higher sensitivity of the technique. Since this technique is based on the relation between quantitative phase imaging and light scattering [28], it is significantly more useful in Dispersion-relation Phase Spectroscopy (DPS) topics [29].

Using ODT and 3D inverse scattering to image biological samples was studied in depth for the past decade. First, filtered back-projection methods were used for 3D refractive index mapping [11, 13]. Then, Wolf's theory on optical diffraction was used to improve the resolution and the quality in 3D reconstruction [12, 30]. Recently the synthetic aperture laser QPI approach and the complex deconvolution of the system point spread function was used by Y. Cotte et al. for high resolution tomographic imaging [14]. In 2014, a new method of solving inverse scattering in the wave vector space was developed by Kim et al. and the reconstruction of transparent 3D objects was demonstrated which they called White-light Diffraction Tomography (WDT) [25]. In general, they extend Wolf's diffraction tomography to broadband illumination and give an accurate solution, without any far-field approximation. Then Spatial Light Interference Microscopy (SLIM), which is the combination of QPI and WDT techniques was introduced [31]. SLIM was able to successfully reconstruct unlabelled live cells in 3D providing sub-micron resolution in all three directions. The wave vector space method used in WDT can also be used to solve other problems, such as, inverse scattering using OCT [32]. Since QPI is a label-free method, the specimen is viable for extended periods of time, thus, it is ideal for imaging live cells that can be sensitive to subtle perturbations [33]. Recently, applications of QPI for non-invasive studies of cell dynamics, such as, blood testing, cell growth, tissue diagnosis, and 3D cell imaging are investigated. Tremendous progress in biomedical imaging specially quantitative methods suit-

able for studying live, unstained cells make us able to quantify the cell's size, 3D shape, etc. by measuring the light the cell scatters along particular directions.

In 1985, Snyder et al. [34], followed up Byer's group work on optical absorption tomography [35] by scanning the incident laser beam from 0° to 360° using a rotating mirror and measuring the far field. Their experiment backed up using optical diffraction tomography for 3D object reconstruction. In 1993, an iterative method, based on a priori object support was proposed by Schatzberg et al. which obtains the tomogram by measuring the scattered field intensity in the far field [36]. Although due to some difficulties, in its early years, ODT did not make a good impact, nowadays, camera technologies and processing power improvements make it a very hot area of research. Recently, laser based DT was increasingly used to demonstrate label-free 3D imaging of biological samples. In the next part, we investigate, discuss and compare some of the leading approaches.

2.2 Recently proposed methods

The use of laser diode based digital holographic microscope for tomographic imaging was firstly proposed by Charriere et al in 2006 [13]. In Figure 2.1 (adapted from [13]), part (1) illustrates a cut in the middle of the pollen cell 3D reconstruction, while parts (2) and (3) show cuts of the cell along the y-z and x-z plane, respectively.

Since fixing the object rotation axis is problematic and perturbing to the sample. In 2007, Choi et al. presented another method for diffraction tomography which is referred to as Tomographic Phase Microscopy (TPM) [11]. This method was unable to scan incident beam angles over a range of 60 degree due to finite numerical aperture of the optical devices used. To examine their method the authors imaged single HeLa cells in culture medium. A 3D index tomogram of a single cell is shown in Figure 2.2 (a) and (b) which is adopted from [11]. The x-y tomographic slices of the same cell at $z = 12, 9.5, 8.5, 7.5, 6.5$ and $5.5 \mu\text{m}$ above the substrate are presented in Figure 2.2 (c) to (h) indicating the inhomogeneity of the refractive index, varying from 1.36 to 1.40. Figure 2.2 (i) and (j) present the wide field images which is obviously related to the slices in terms of cell boundary, nuclear boundaries and size and shape of the nucleoli.

In 2014, Kim et al. provided an angle scanning ODT for imaging red blood cells in which reconstructions from the DT method and the projection method were compared. The authors claim that in their method the refractive index distribution is calculated more accurately than the projection method by taking diffraction into account. Considering the effect of diffraction, challenges like limited spatial resolution and low image quality are addressed.

Figure 2.3 (taken from [37]) explains the reconstruction processes of the two algorithms schematically. Figure 2.3 (a) presents quantitative phase images (left) and corresponding spectrum in Fourier space (right) of a *Plasmodium falciparum* red blood cell measured at various illumination angles. Figure 2.3 (b) shows object

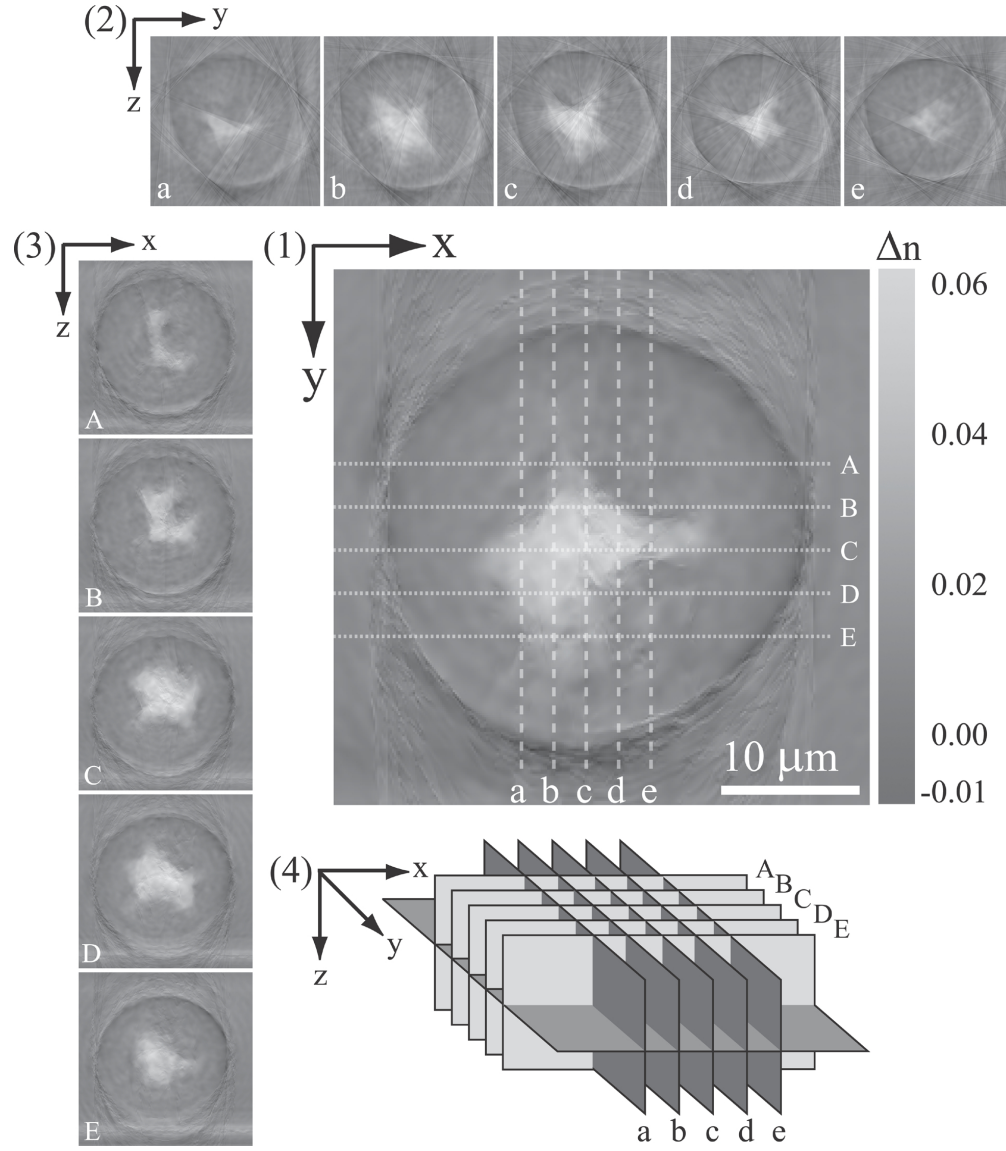


Figure 2.1: A pollen cell refractive index: (1) A cut in $x-y$ plane in the middle of the pollen cell, (2) cuts at different x along the $y-z$ plane, (3) cuts at different y along the $x-y$ plane, and (4) schematic of the presented cuts. Figure is taken from [13].

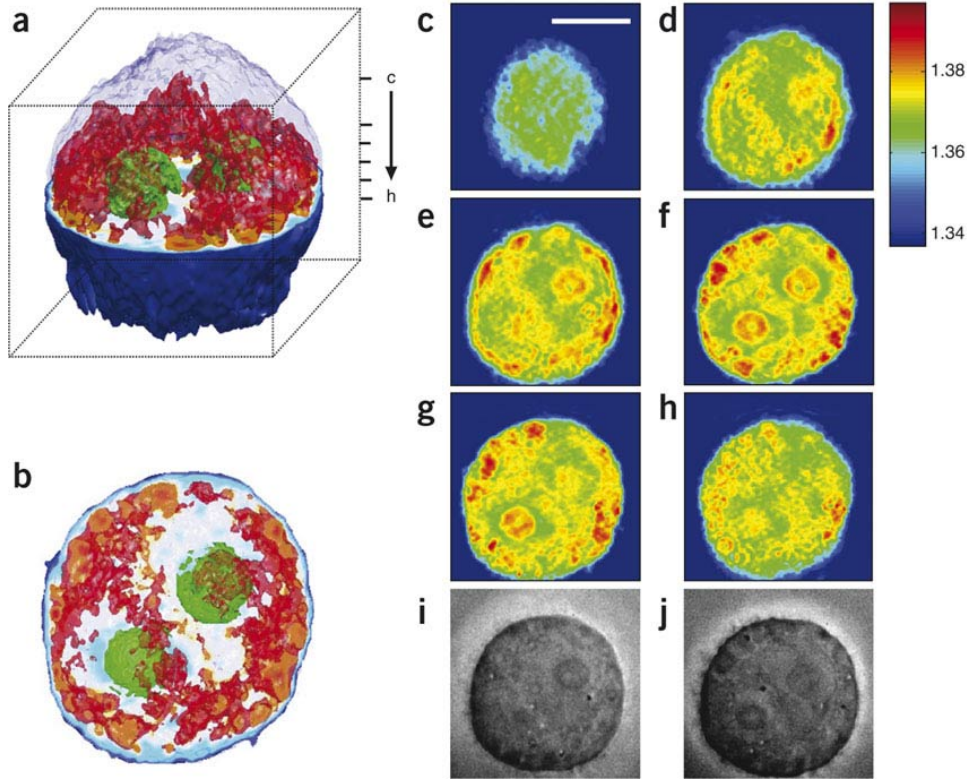


Figure 2.2: (a) 3D rendering of a HeLa cell. Each side of the cube is $20\mu m$. (b) Top view of (a). (c)-(h) Slices of the tomogram at $z = 12, 9.5, 8.5, 7.5, 6.5$ and $5.5\mu m$ above the substrate (indicated in (a)). Scale bar is $10\mu m$. (i) and (j) are white-field images of focus corresponding to (e) and (f), respectively. Figure taken from [11].

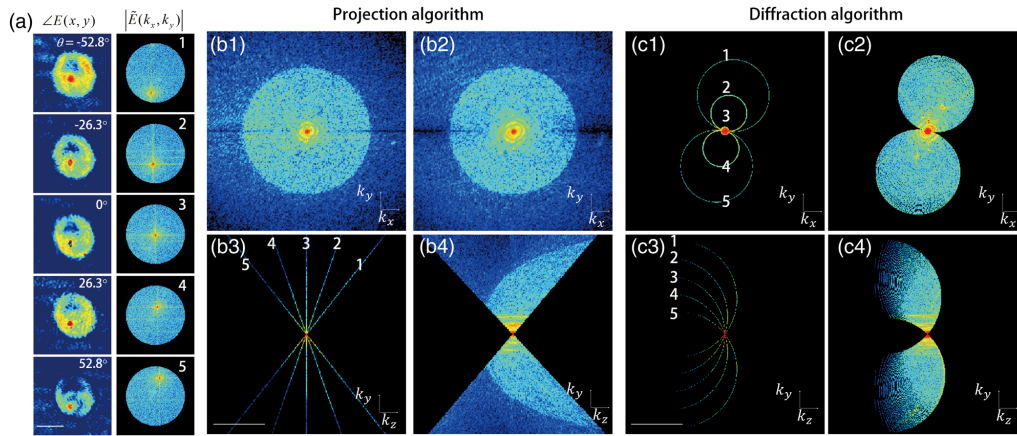


Figure 2.3: (a) Quantitative phase images (left) and corresponding spectrum in Fourier space (right) of a red blood cell measured at various illumination angles. (b) Object functions in Fourier space reconstructed by the projection algorithm and (c) the diffraction algorithm. Amplitude distributions reconstructed by the projection algorithm in $k_x - k_y$ plane with (b1), (c1) five illuminations angles and (b2), (c2) the full illumination angles. (b3), (c3) and (b4), (c4) present amplitude distributions in the $k_z - k_y$ plane, respectively. Image taken from [37].

functions in Fourier space reconstructed by the projection algorithm and Figure 2.3 (c) shows the same thing for the diffraction algorithm. Figure 2.3 (b) and (c) are divided to the following sub-figures; Amplitude distributions reconstructed by the projection algorithm in $k_x - k_y$ plane with (b1), (c1) five illumination angles and (b2), (c2) the full illumination angles. The corresponding amplitude distributions in the $k_z - k_y$ plane are shown in (b3), (c3) and (b4), (c4), respectively.

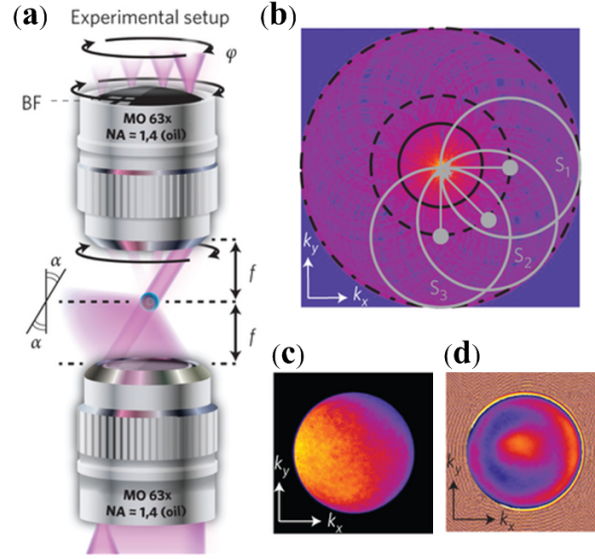


Figure 2.4: (a) The best scanning concept for such a synthetic aperture which is a beam illuminating the specimen from various directions in a circle shape. (b) Synthesized k_x, k_y plane measurement expanding frequency space signal coverage by a factor of two. (c), (d) Experimental measurement of the two-dimensional projected amplitude and phase, respectively. Figure adapted from [14].

Due to the laser speckle phenomena and the limited coverage of the scanning angle, the laser based angle-scanning ODT system do not have good sensitivity and the resolution is limited to $\lambda/2$. In 2013, Cotte et al. proposed a synthetic aperture digital holographic microscopy approach using the whole aperture of the upright objective (63x/NA = 1.4 oil immersion) [14]. Since they use high NA objective, their system could collect the scattered light with angle coverage close to 2π (they call it quasi- 2π -digital holographic microscopy). The scattered light beyond the numerical aperture of the objectives can be detected by rotational illumination. Figure 2.4 (a) presents the best scanning concept for such a synthetic aperture which is a beam illuminating the specimen from various directions in a circular shape. Figure 2.4 (b) shows how k_x, k_y expands in frequency space signal coverage by a factor of two. The complex deconvolution algorithm is used in 3D reconstruction to achieve transverse imaging resolution higher than two times better than the diffraction limit. Figure 2.4 (c) and (d) present experimental measurement of the two-dimensional amplitude and phase, respectively. In the 3D reconstruction, the complex deconvolution algorithm is used achieving transverse

imaging resolution more than twice better than the diffraction limit.

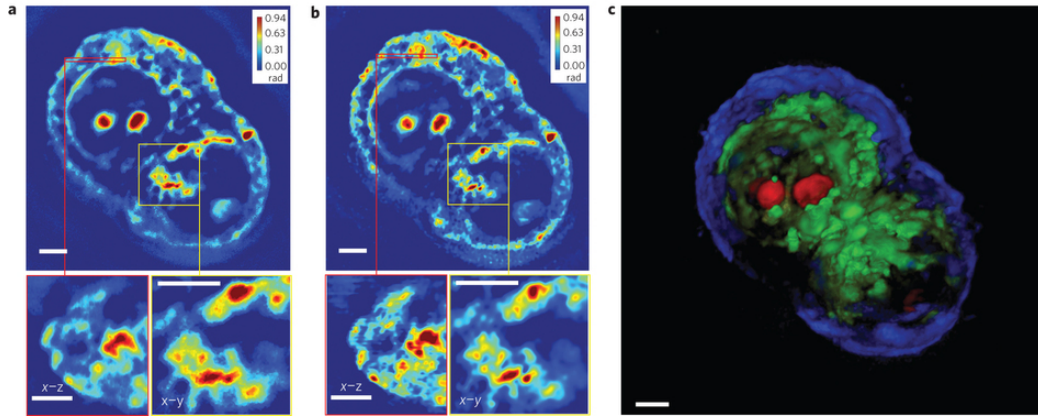


Figure 2.5: (a) A measured z-slice at the top, a cross-section at the area indicated by the red box in the bottom left and a zoomed-in image of the area indicated by the yellow box in bottom right. (b) A deconvolved z-slice corresponding to the presented measurement. (c) 3D rendering of the deconvolution result using 140 images. Scale bars = $5\mu\text{m}$. Image taken from [25].

In [25], WDT with spatially coherent and temporally incoherent light has been used to retrieve 3D structures of unlabeled cells. In WDT the depth information is obtained by scanning the focus through the object along the optical axis. The WDT theory is a generalization of the Wolf's diffraction tomography describing the light-matter interaction for broadband light and weakly scattering objects. WDT is label-free and uses visible light which is highly stable for 3D imaging over time, making it a possible candidate for become a standard 3D imaging modality in cell biology in near future. In [25], the authors used the deconvolved z-stack to generate the 3D rendering of the HT-29 cell. Figure 2.5 (a) presents a measured z-slice at the top, a cross-section at the area indicated by the red box in the bottom left and a zoomed-in image of the area indicated by the yellow box in bottom right. Figure 2.5 (b) shows a deconvolved z-slice of the same measurement. Comparing (a) and (b) clearly shows the resolution increase. Figure 2.5 (c) presents 3D rendering of the deconvolution result using 140 images with a dimension of 640×640 which took an hour for running [25].

Time-resolved tomography which is extending WDT to 4D imaging in which the 4th dimension is time is getting popular as well [38]. Using the commercial phase contrast microscopes with environmental control and cell incubating chamber makes this feasible. High-precision microscope stage ensures imaging at specific positions in space without drifting over time. Figure 2.6 present a HeLa cell during 24 hours period with active movements and even increase in the number of nucleoli indicating the capacity of WDT imaging over an extended period of time.

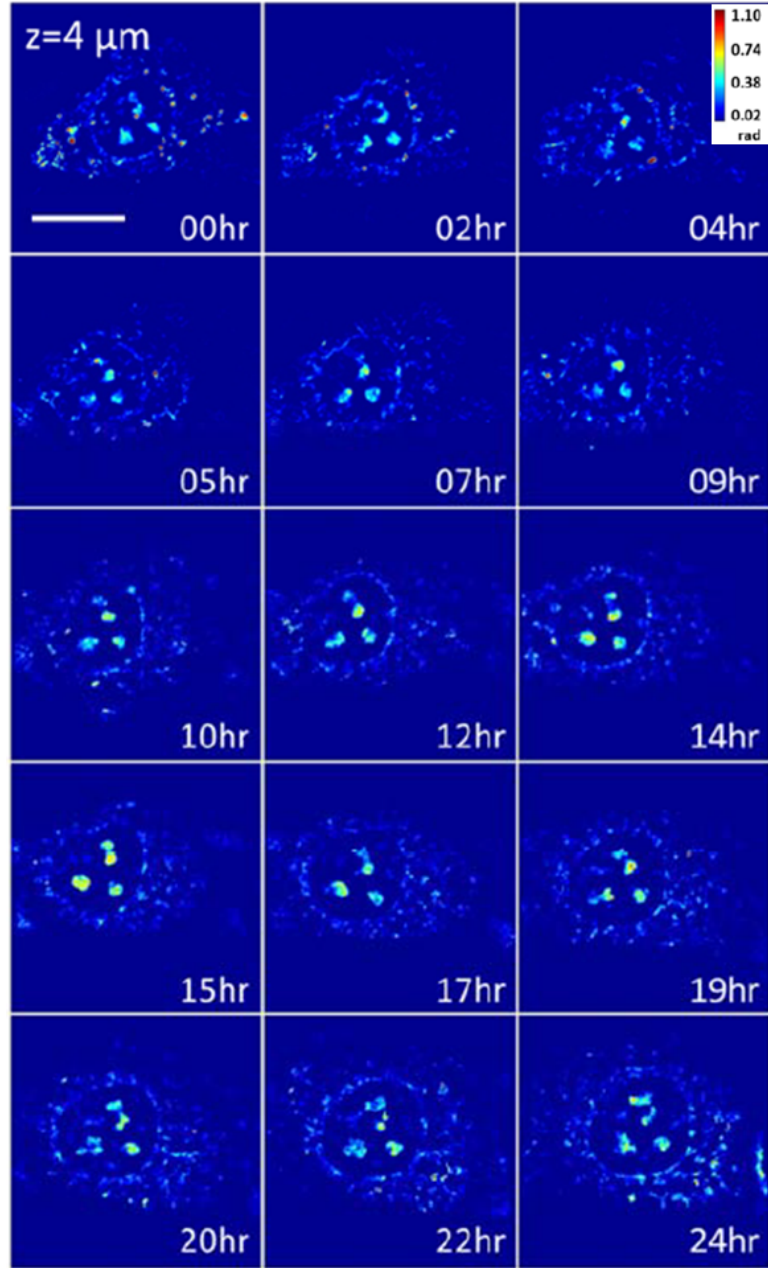


Figure 2.6: A HeLa cell $x - y$ section of WDT images taken at $z = 4 \mu\text{m}$ from the bottom of the cell, where the nucleoli is clearly observable. Scale bar = 20μ . Figures adapted from [38].

2.3 Bibliography

- [1] Saleh, Bahaa EA, Malvin Carl Teich, and Bahaa E. Saleh. "Fundamentals of photonics," Vol. 22. New York: Wiley, 1991.
- [2] W. L. Bragg, "The structure of some crystals as indicated by their diffraction of x-rays," *P R Soc Lond a-Conta* 89(610), 248-277(1913).
- [3] E. Wolf, "History and solution of the phase problem in the theory of structure determination of crystals from X-ray diffraction measurements," *Adv Imag Elect Phys* 165, 283-325 (2011).
- [4] E. Wolf, "Three-dimensional structure determination of semi-transparent objects from holographic data," *Opt Commun* 1(4), 153(1969).
- [5] E. Wolf, "Determination of the amplitude and the phase of scattered fields by holography," *J. Opt. Soc. Am.* 60, 18-20 (1970).
- [6] K. Iwata, and R. Nagata. "Calculation of three-dimensional refractive-index distribution from interferograms." *JOSA* 60, no. 1 (1970): 133-135.
- [7] R. Dandliker, and K. Weiss. "Reconstruction of the three-dimensional refractive index from scattered waves." *Optics communications* 1, no. 7 (1970): 323-328.
- [8] D. W. Sweeney, and C. M. Vest. "Reconstruction of three-dimensional refractive index fields from multidirectional interferometric data." *Applied Optics* 12, no. 11 (1973): 2649-2664.
- [9] R. Fiolka, K. Wicker, R. Heintzmann, and A. Stemmer, "Simplified approach to diffraction tomography in optical microscopy". *Optics Express* 17(15), 12407-12417 (2009).
- [10] O. Haeberle, K. Belkebir, H. Giovaninni, and A. Sentenac, "Tomographic diffractive microscopy: basics, techniques and perspectives," *Journal of Modern Optics* 57(9), 686-699 (2010).
- [11] W. Choi, et al. "Tomographic phase microscopy," *Nature Methods* 4(9), 717-719 (2007).
- [12] Y. Sung, W. Choi, N. Lue, R. R. Dasari, and Z. Yaqoob, "Stain-free quantification of chromosomes in live cells using regularized tomographic phase microscopy," *Plos One* 7(11), e49502 (2012).
- [13] F. Charriere, et al. "Cell refractive index tomography by digital holographic microscopy," *Opt. Lett.* 31(2), 178-180 (2006).
- [14] Y. Cotte, et al. "Marker-free phase nanoscopy," *Nature Photon.* 7(2), 113-117 (2013).

- [15] J. W. Goodman "Speckle Phenomena in Optics: Theory and Applications," (Roberts & Co, 2007).
- [16] D. Huang, et al. "Optical coherence tomography," *Science* 254(5035), 1178-1181 (1991).
- [17] A. F. Fercher, W. Drexler, C. K. Hitzenberger, and T. Lasser, "Optical coherence tomography - principles and applications," *Rep Prog Phys* 66(2), 239-303 (2003).
- [18] A. F. Fercher, "Optical coherence tomography," *Journal of Biomedical Optics* 1(2), 157-173 (1996).
- [19] T. S. Ralston, D. L. Marks, P. S. Carney, and S. A. Boppart, "Real-time interferometric synthetic aperture microscopy," *Optics Express* 16(4), 2555-2569 (2008).
- [20] G. Popescu, "Quantitative Phase Imaging of Cells and Tissues," (McGraw Hill, 2011).
- [21] D. Gabor, "A new microscopic principle," *Nature* 161, 777 (1948)
- [22] F. Zernike, "Phase contrast, a new method for the microscopic observation of transparent objects, Part 1," *Physica* 9(7), 686-698 (1942).
- [23] F. Zernike, "Phase contrast, a new method for the microscopic observation of transparent objects, Part 2," *Physica* 9, 974-986 (1942).
- [24] M. Mir, et al. "Visualizing Escherichia coli Sub-Cellular Structure Using Sparse Deconvolution Spatial Light Interference Tomography," *PLoS ONE* 7(6), e39816 (2012)
- [25] T. Kim, et al. "White-light diffraction tomography of unlabelled live cells," *Nat Photon* 8(3), 256-263 (2014).
- [26] S. A. Alexandrov, T. R. Hillman, and D. D. Sampson, "Spatially resolved Fourier holographic light scattering angular spectroscopy," *Optics Letters* 30(24), 3305-3307 (2005).
- [27] H. F. Ding, Z. Wang, F. Nguyen, S. A. Boppart, and G. Popescu, "Fourier Transform Light Scattering of Inhomogeneous and Dynamic Structures," *Physical Review Letters* 101(23), 238102 (2008).
- [28] H. Ding, Z. Wang, X. Liang, S. A. Boppart, and G. Popescu, "Measuring the scattering parameters of tissues from quantitative phase imaging of thin slices," *Optics Letters* 36, 2281 (2011).
- [29] R. Wang, et al. "Dispersion-relation phase spectroscopy of intracellular transport," *Opt Express* 19(21), 20571-20579 (2011)

- [30] Y. J. Sung, et al. "Optical diffraction tomography for high resolution live cell imaging," *Opt Express* 17(1), 266-277 (2009).
- [31] Z. Wang, et al. "Spatial light interference microscopy (SLIM)," *Opt Express* 19(2), 1016 (2011).
- [32] R. Zhou, T. Kim, L. L. Goddard, and G. Popescu, "Inverse scattering solutions using low-coherence light," *Optics Letters* 39(15), 4494-4497 (2014).
- [33] P. Marquet, et al. "Digital holographic microscopy: a noninvasive contrast imaging technique allowing quantitative visualization of living cells with sub-wavelength axial accuracy," *Opt. Lett.* 30(5), 468-470 (2005).
- [34] R. Snyder and L. Hesselink, "High-Speed Optical Tomography for Flow Visualization," *Appl Optics* 24(23), 4046-4051 (1985).
- [35] K. Bennett and R. L. Byer, "Optical tomography - experimental-verification of noise theory," *Optics Letters* 9(7), 270-272 (1984).
- [36] A. Schatzberg and A. J. Devaney, "Rough-Surface Inverse Scattering within the Rytov Approximation," *J Opt Soc Am A* 10(5), 942-950 (1993).
- [37] K. Kim, et al. "High-resolution three-dimensional imaging of red blood cells parasitized by *Plasmodium falciparum* and in situ hemozoin crystals using optical diffraction tomography," *Journal of Biomedical Optics* 19(1), 011005-011005 (2013).
- [38] Kim, Taewoo, Renjie Zhou, Lynford L. Goddard, and Gabriel Popescu. "Solving inverse scattering problems in biological samples by quantitative phase imaging," *Laser & Photonics Reviews* 10, no. 1 (2016): 13-39.

Proposed Method

Contents

3.1 Introduction	17
3.2 Experimental setup	18
3.3 Methodology	19
3.4 Results	21
3.5 Discussions and conclusions	28
3.6 Bibliography	28

Optical tomography has been widely investigated for biomedical imaging applications. In recent years, optical tomography has been combined with digital holography and has been employed to produce high-quality images of phase objects such as cells. In this chapter, we describe a method for imaging 3D phase objects in a tomographic configuration implemented by training an artificial neural network to reproduce the complex amplitude of the experimentally measured scattered light. The network is designed such that the voxel values of the refractive index of the 3D object are the variables that are adapted during the training process. We demonstrate the method experimentally by forming images of the 3D refractive index distribution of HeLa cells.

3.1 Introduction

The learning approach to imaging we describe in this chapter is related to adaptive techniques in phased antenna arrays [1], iterative imaging schemes [2, 3], and inverse scattering [4, 5]. In the optical domain, an iterative approach was demonstrated by the Sentenac group [6, 7] who used the coupled dipole approximation [8] for modeling light propagation in inhomogeneous media (a very accurate method but computationally intensive) to simulate light scattering from small objects ($1\mu\text{m} \times 0.5\mu\text{m}$) in a point scanning microscope configuration. Maleki and Devaney in 1993 [9] demonstrated DT using intensity measurements and iterative phase retrieval [10]. Very recently, an iterative optimization method was demonstrated [11] for imaging 3D objects using incoherent illumination and intensity detection. There are similarities but also complementary differences between our method and [11]. Our method uses coherent light and relies on digital holography [12, 13] to record the complex amplitude of the field whereas direct intensity

detection is used in [11]. Both methods use the BPM [14, 15] to model the scattering process and the error back propagation method [16] to train the system. At the end of the training process the network discovers a 3D index distribution that is consistent with the experimental observations. We experimentally demonstrate the technique by imaging polystyrene beads, HeLa and hTERT-RPE1 cells.

The holographic recording employed in the method presented in this thesis is advantageous for imaging phase objects, such as, the cells investigated in the experiments. Moreover, sparsity constraints are included in this optimization algorithm which improves significantly the quality of the reconstructions. We also compared our method to other coherent tomographic reconstruction techniques. The learning approach improved the quality in comparison with all the direct (non-iterative) tomographic reconstruction methods we tried.

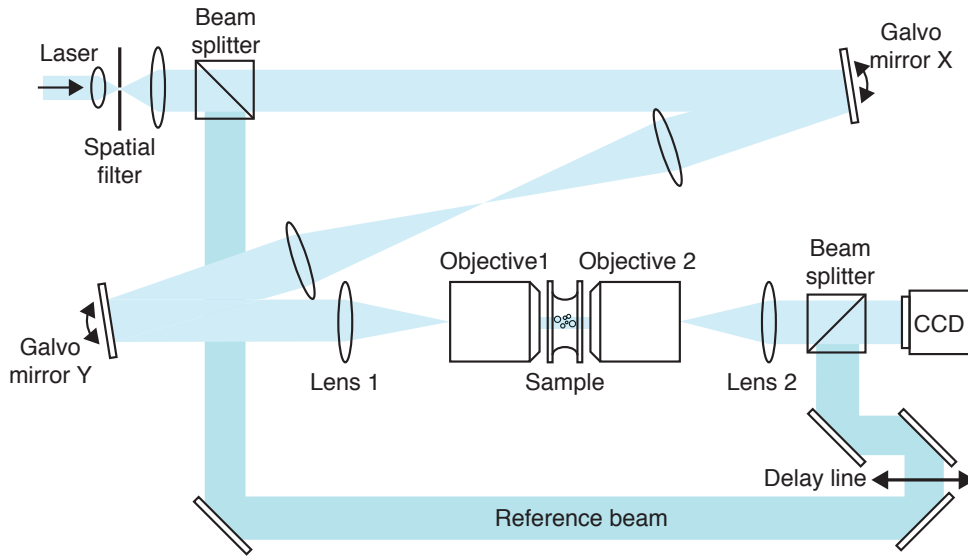


Figure 3.1: **Experimental apparatus.** The laser beam is first expanded and passed through a spatial filter in order to produce a clean plane wave. It is then split into a reference and a signal beam. The signal beam is sent on a first galvo-mirror, the surface of which is imaged onto a second galvo-mirror through a 4f lens system. The beam is focused in the back focal plane of the illumination objective, which leads to a plane wave illumination of the sample. The sample is imaged on a CCD camera using an objective and a tube lens. The surface of the galvo-mirrors, the sample and the camera plane are in conjugate image plane of each other. The reference beam passes in a delay line to adjust the path length and then recombined in order to create an interference pattern on the camera detector.

3.2 Experimental setup

A schematic diagram of the experimental setup is shown in Figure 3.1. It is a holographic tomography system [17], in which the sample is illuminated with multiple angles and the scattered light is holographically recorded. Several variations of the

holographic tomography system have been demonstrated before [18–21]. The optical arrangement we used is most similar to the one described by Choi *et al.* [18]. The first beam splitter divides the laser beam in the reference and signal arms. In the signal arm a rotating mirror varies the angle of illumination of the sample using the 4F system created by Lens 1 and Objective 1. The sample is imaged onto the CCD camera using the 4F system created by Objective 2 and Lens 2. The reference beam is combined with the signal beam via the second beamsplitter to form a hologram. Phase stability is maintained by using a differential measurement between the phase on a portion of the field of view on the detector that does not include the cell and the cell itself. In this way, the system is insensitive to drifts in the relative phase between the reference and signal beams. The NA's are 1.45 and 1.4 for the illumination and imaging portions of the system (Objective 1 and Objective 2), respectively.

The samples to be measured were prepared by placing polystyrene beads and cells between two glass cover slides. The samples were illuminated with a continuous collimated wave at $561nm$ at 80 different angles. The amplitude and phase of the light transmitted through the sample was imaged onto a 2D detector where it was holographically recorded by introducing a reference beam. These recordings constitute the training set with which we train the computational model that simulates the experimental setup. We construct the network using the BPM. The inhomogeneous medium (beads or cells) is divided into thin slices along the propagation direction (z). The propagation through each slice is calculated as a phase modulation due to the local transverse index variation followed by propagation in a thin slice of a homogenous medium having the average value of the index of refraction of the sample.

The transverse (x - y) resolution is limited by the numerical aperture of the imaging system comprised of lenses OBJ2 and L2 in Figure 3.1. This limit can in principle be exceeded because the illumination is not a single plane wave. This idea was explored for conventional tomography in [22] and it could also be used in conjunction with the learning approach we describe here. The longitudinal (z) resolution is limited by the numerical aperture of the illuminating beam [23].

3.3 Methodology

A schematic description of the BPM simulation is shown in Figure 3.2. The straight lines connecting any two circles represent multiplication of the output of the unit located in the l -th layer of the network at $x = n_l\delta, y = m_l\delta$ by the discretized Fresnel diffraction kernel $e^{j\pi[(n_l^2 - n_{l+1}^2)\delta^2 + (m_l^2 - m_{l+1}^2)\delta^2]/\lambda\delta_z}$ where n_l and m_l are integers and λ is the wavelength of light. δ is the sampling interval in the transverse coordinates (x, y) whereas δ_z is the sampling interval along the propagation direction z . The circles in the diagram of Figure 3.2 perform a summation of the complex amplitude of the signals converging to each circle and also multiplication of this sum by $e^{j(2\pi\Delta n\delta_z z)/\lambda}$. $\Delta n(x, y, z)$ is the unknown 3D index perturbation of the object.

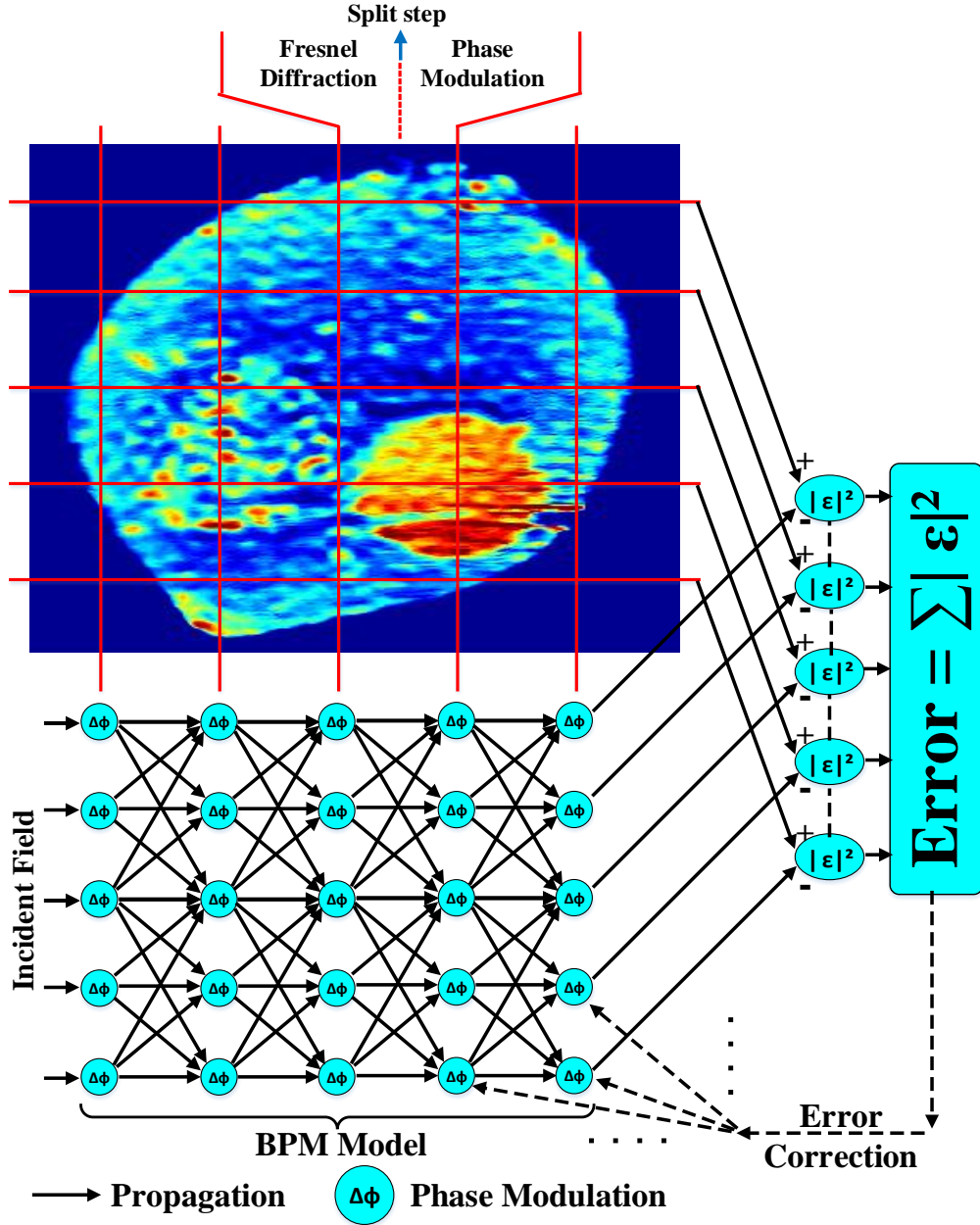


Figure 3.2: Schematic diagram of object reconstruction by learning the 3D index distribution that minimizes the error ϵ , defined at the mean squared difference between the experimental measurement and the prediction of a computational model based on the BPM.

In the experiments, the network has 420 layers with $\Delta n(x, y, z)$ being the adaptable variable. In contrast with a conventional neural network, the output of the layered structure in Figure 3.2 is a linear function of the input complex field amplitude. However, the dependence of the output is nonlinearly related to $\Delta n(x, y, z)$. The BPM can be trained using steepest descent exactly as the back propagation algorithm in neural networks [24–26]. Specifically, the learning algorithm carries out the following minimization:

$$\min_{\Delta \hat{n}} \left\{ \frac{1}{2K} \sum_{k=1}^K \|E_k(\Delta \hat{n}) - M_k(\Delta n)\|^2 + \tau S(\Delta \hat{n}) \right\}$$

subject to $0 \leq \Delta \hat{n}$

In the expression above, $E_k(\Delta \hat{n})$ is the current prediction of the BPM network for the complex field created by estimated refractive index when the system is illuminated with the k -th beam and $M_k(\Delta n)$ is the complex field measured by the experimental setup. $\Delta \hat{n}$ indicates the estimate for the index perturbation due to the object. The term $S(\Delta \hat{n})$ is a sparsity constraint [27–29] to enhance the contrast while τ is a parameter that can be tuned to maximize image quality by systematic search. We assessed the significance of the sparsity constraint by running the learning algorithm with and without this constraint. An example of the results is shown in Figure 4.7 in Chapter 4. The positivity constraint takes advantage of the assumption that the index perturbation is real and positive. The optimization is carried out iteratively by taking the derivative of the error with respect to each of the adaptable parameters following steepest descent;

$$\Delta \hat{n} \leftarrow \Delta \hat{n} - \left(\frac{\alpha}{K} \sum_{k=1}^K \varepsilon_k \frac{\partial \varepsilon_k}{\partial \Delta \hat{n}} + \tau \frac{\partial S(\Delta \hat{n})}{\partial \Delta \hat{n}} \right)$$

where $\varepsilon_k = \|E_k(\Delta \hat{n}) - M_k(\Delta n)\|$ is the error, α is a constant and the change in $\Delta \hat{n}$ is proportional to the error and its derivative. This is achieved efficiently via a recursive computation of the gradient, which is the back propagation part of our learning algorithm. The data acquisition speed of this method is the same as any other optical tomography method. It is determined by the product of the number of illumination angles and the time required capturing each hologram. The processing time to run the learning algorithm (100 iterations) after the data is recorded takes more than an hour on a standard laptop computer but it can be improved dramatically with custom signal processing circuits.

3.4 Results

We first tested the system with polystyrene beads encapsulated between two glass slides in immersion oil. The sample was inserted in the optical system of Figure 3.1 and 80 holograms were recorded by illuminating the sample at 80 distinct angles uniformly distributed in the range -45 degrees to +45 degrees (The angle range is

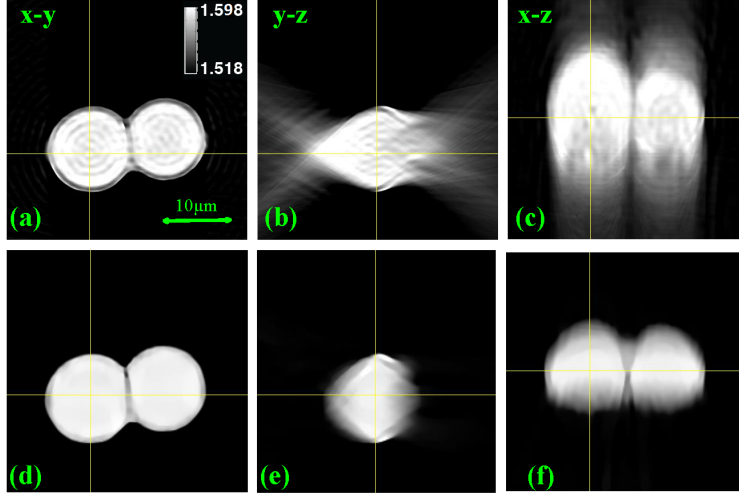


Figure 3.3: Experimental reconstruction of two $10\mu m$ beads of refractive index 1.588 at $\lambda = 561nm$ in immersion oil with $n_0 = 1.516$. (a)-(c) x-y, y-z and x-z slices using the inverse Radon transform reconstruction, (d)-(f) the same slices for our learning based reconstruction method (The lines indicate the location of the slices).

reduced to have insensitive measurement easily replicable with lower NA). The collected data is the training set for the 420-layer BPM network which simulates a physical propagation distance of $30\mu m$ and transverse window $37\mu m \times 37\mu m$ ($\delta_x = \delta_y = 72nm$). The network was initialized with the standard filtered back projection reconstruction algorithm (Radon transform) [30] and the resulting 3D images before and after 100 iterations are shown in Figure 3.3. The final image produced by the learning algorithm is an accurate reproduction of the bead shape.

The power of the presented LT method is that the reconstruction of the refractive index is not limited to the Born approximation. The BPM does not account for reflections but it allows multiple forward scattering events. In case of multiple inhomogeneities, the Born approximation is not valid anymore and the reconstruction based on conventional tomographic techniques become inaccurate. In order to demonstrate this effect, we simulate a refractive index inhomogeneity ($\Delta n = 0.04, D = 5\mu m$) that comprises of two spherical beads on the optical axis at two different z-planes. Considering the center of the computational window to be the center of the x-y plane, the center of the beads are placed at, $x_1 = 0\mu m$, $y_1 = 0\mu m$, $z_1 = 6\mu m$ and $x_2 = 0\mu m$, $y_2 = 5\mu m$, $z_2 = 12\mu m$ at a distance of $6\mu m$ away from each other. Figure 3.4 shows the results of the two different reconstruction schemes. Based on our previous explanation, since the Born approximation is not valid to describe the physical behaviour of light propagation through this sample, the optical DT method is not capable of reconstructing the object. Contrary to that, the proposed LT method is capable of dealing with multiple scattering and therefore correctly reconstructs the object.

A sample containing a single HeLa cell was also prepared and the same pro-

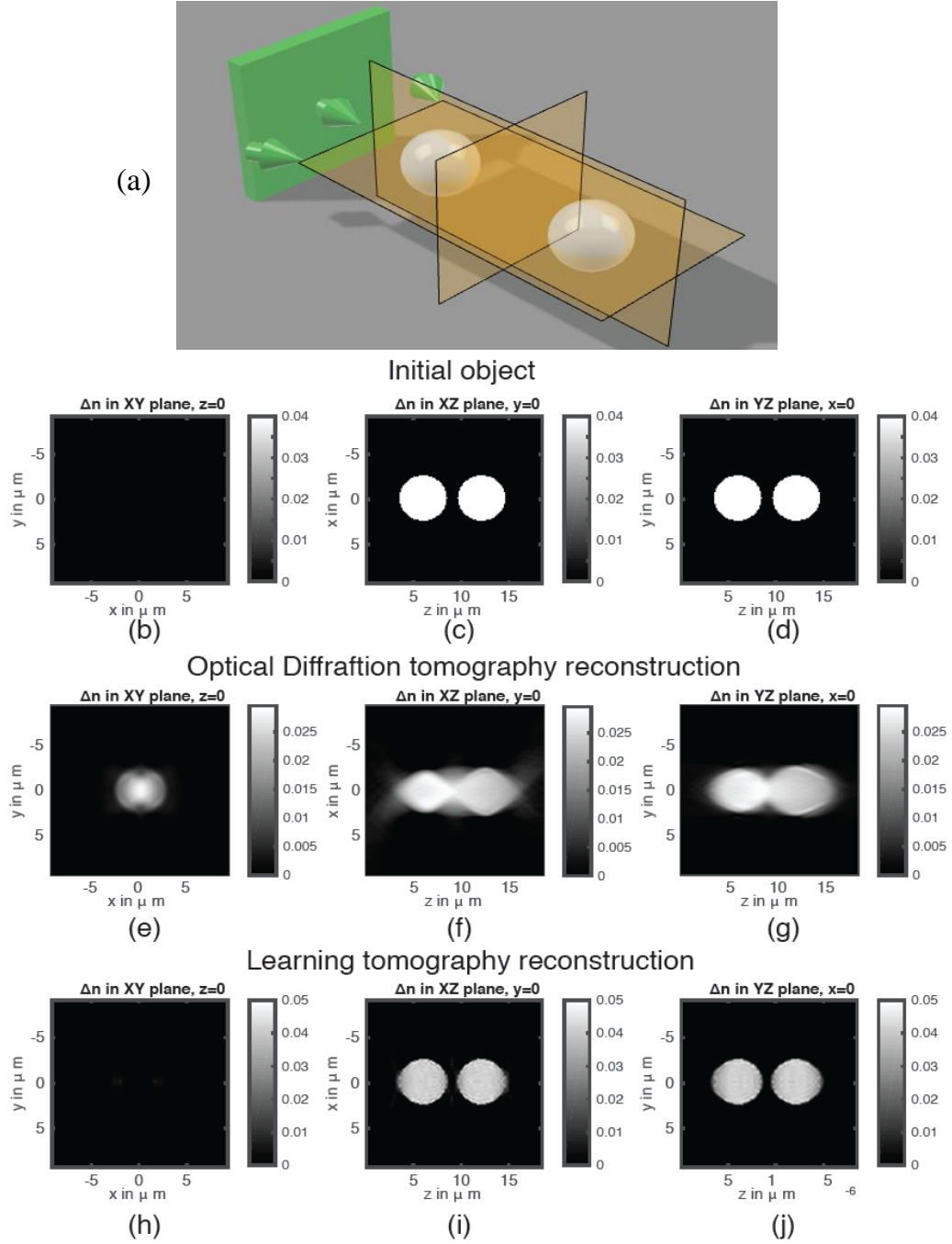


Figure 3.4: Simulation geometry comprises of two spherical beads with a refractive index difference of 0.04 compared to the background. (b)-(j). Cross-sectional views on x-y, x-z and y-z planes of the original refractive index (b)-(d), reconstruction with ODT (e)-(g) and LT (h)-(j). Since the Born approximation (single scattering) is not valid, the DT fails to reconstruct the refractive index inhomogeneity. However, the LT is capable of correctly reconstructing the object.

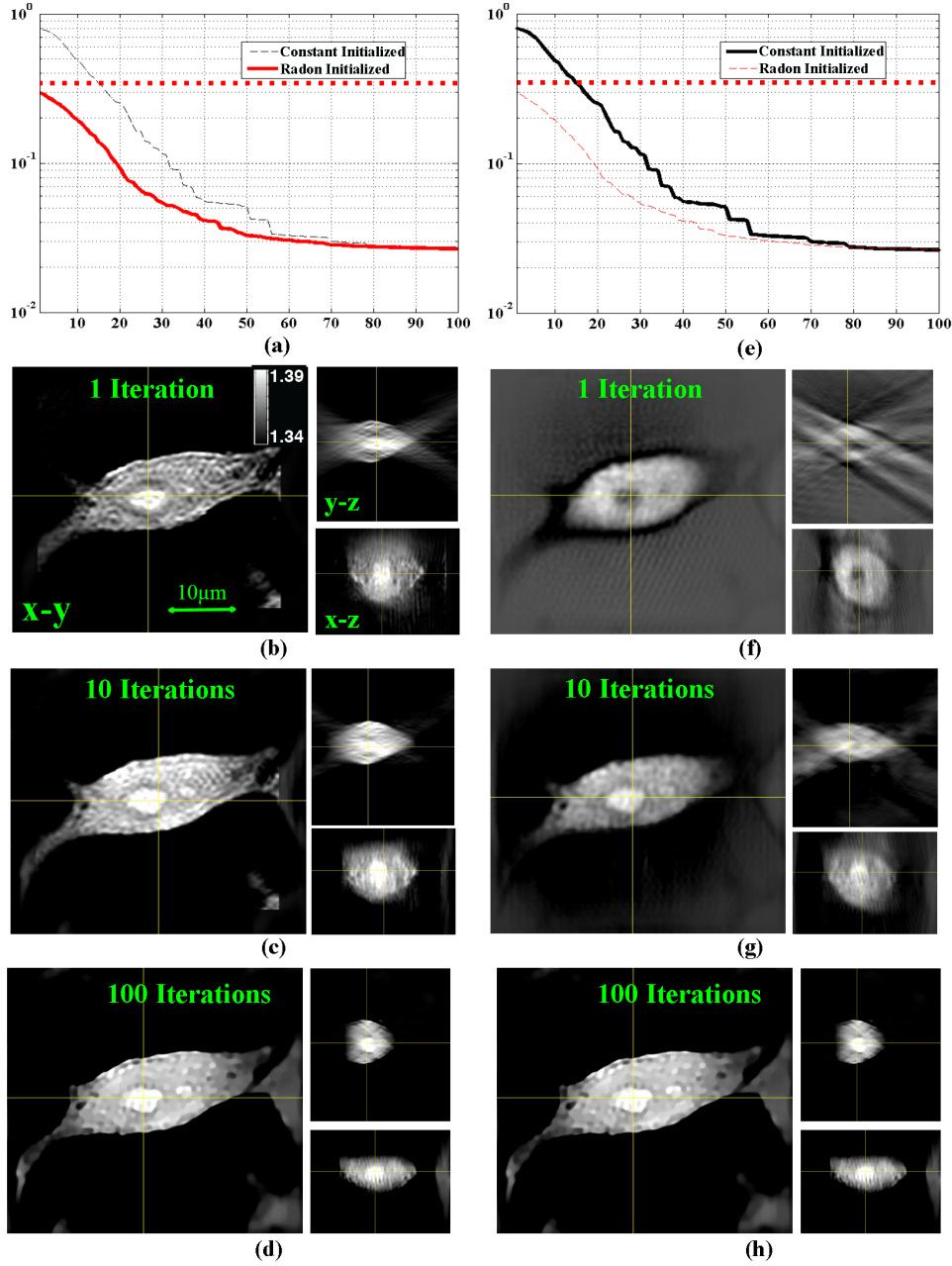


Figure 3.5: Comparison of the proposed method initialized with the inverse Radon transform (left) versus initialization with a constant value ($\Delta\hat{n} = 0.007$) (right). (a) and (e) plot the normalized error on measurement fall-off for 80 illumination angles initialized with the inverse Radon and constant value, respectively. The horizontal dotted line shows the inverse Radon performance for comparison. (b)-(d), x-y, y-z and x-z stacks for respectively the first, tenth and hundredth iteration of the proposed method initialized by inverse Radon. (d)-(f), the same figures for the proposed method initialized by constant value.

cedure was followed to obtain a 3D image. The results are shown in Figure 3.5 where the normalized error on measurement is plotted as a function of iteration number. In this instance, the system was initialized with a constant but nonzero value ($\Delta\hat{n} = 0.007$). Also shown in Figure 3.5 are the results obtained when the system was initialized with the Radon reconstruction from the same data. After 100 iterations both runs yield essentially identical results. Notice that the error in the final image (after 100 iterations) is significantly lower than to the error of the Radon reconstruction. This is also evident by visual inspection of the images in Figure 3.5 where the artifacts due to the missing cone [31] and diffraction [18] are reduced by the learning process.

We use the result of tomographic reconstructions to initialize the learning algorithm. The results are included in Figure 3.6, showing that DT [32] and iterative Radon [18] give smaller initial error than simple Radon reconstructions but the learning algorithm in all cases reduces the error further and improves the quality of the reconstructed image. The four runs corresponding to the four different initial conditions converge to the same final reconstruction. The images corresponding to the three tomographic reconstructions used as initial conditions are presented in Appendix A.1; where results from an experiment with a reduced range of illumination angles is presented as well.

As discussed earlier, optical 3D imaging techniques rely on the assumption that the object being imaged does not significantly distort the illuminating beam. This is assumed for example in Radon or DT. In other words, these 3D reconstruction methods rely on the assumption that the measured scattered light consists of photons that have only been scattered once before they reach the detector. The BPM, on the other hand, allows for multiple forward scattering events. The only simplification is that reflections are not taken into account; these could eventually be incorporated in the network equation without fundamentally altering the approach described here. Since biological tissue is generally forward scattering, BPM can be a good candidate to model propagation of thick biological samples and this may be the most significant advantage of the learning approach. To demonstrate this point, we prepared two glass slides with a random distribution of hTERT-RPE1 cells (immortalized epithelial cells from retina) on each slide. When we attach the two slides together, we can find locations where two cells are aligned in z , one on top of the other. Figure 3.7 (a)-(e) shows the image of such a stack of two cells produced with a direct inversion using the Radon transform. Figure 3.7 (f)-(j) shows the same object imaged with the proposed learning algorithm. The learning method was able to distinguish the two cells where the Radon reconstruction merged the two into a single pattern due to the blurring in z which is a consequence of the missing cone. We believe the origin of the ringing artifacts in the Radon image is due to the multiple scattering of light from one cell to another (as explained earlier).

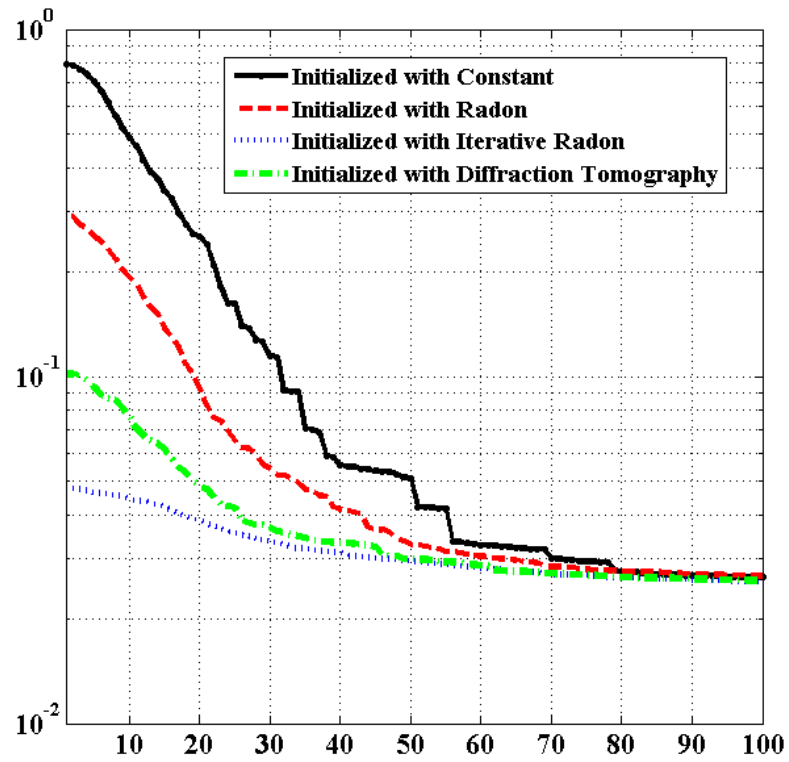


Figure 3.6: The error between the experimental measurements and the predictions of the computational mode plotted as a function of the number of iterations for four different initial conditions: Constant index (black), Radon tomographic reconstruction (red), Diffraction tomography [32] (green) and the iterative method described [18] (blue) .

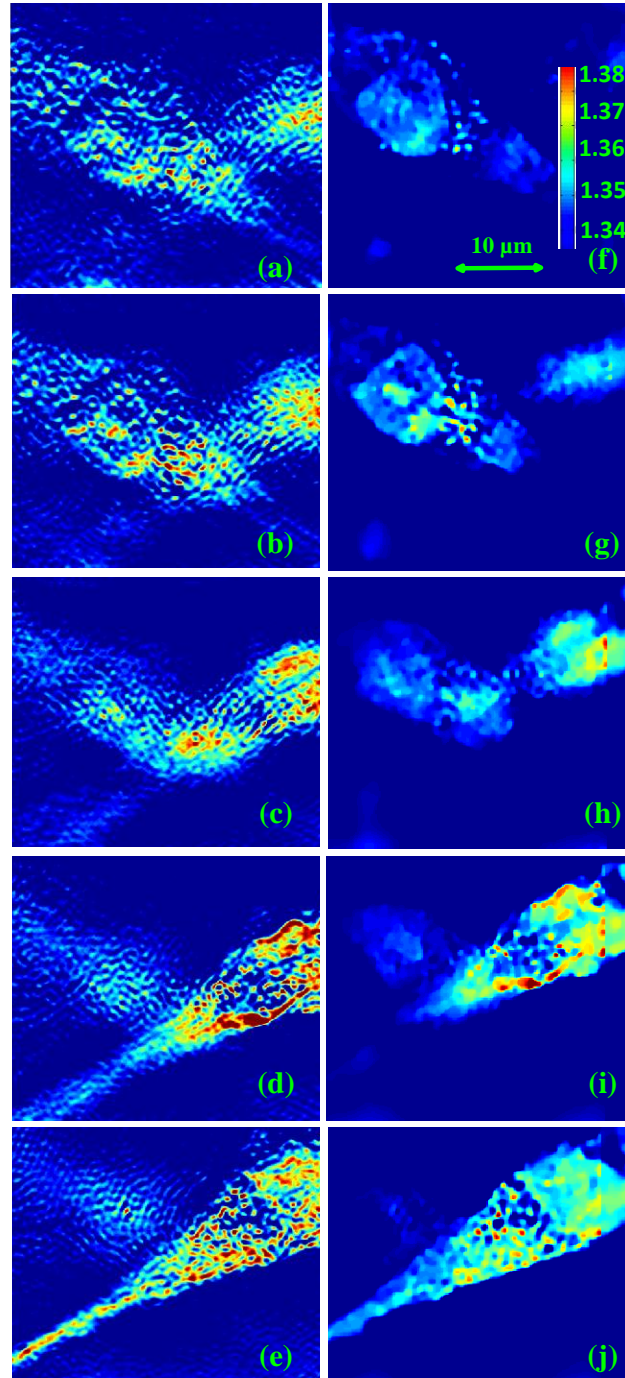


Figure 3.7: Images of two hTERT-RPE1 cells. x-y slices corresponding to different depths of respectively +9, +6, +3, 0 and -3 microns (positive being toward the detector) from the focal plane of the second objective in Figure 3.1 for: (a)-(e) the inverse Radon transform based reconstruction and (f)-(j) the same slices for our learning based reconstruction method.

3.5 Discussions and conclusions

In conclusion, we have demonstrated a neural-network based algorithm to solve the optical phase tomography problem and have applied it to biological (HeLa and hTERT-RPE1 cells) and synthetic (polystyrene beads) samples. The experimental measurements were performed with a conventional collimated illumination phase tomography setup, with coherent light and holograms were recorded off-axis. The sample scattering potential was modeled as a neural network implementing a forward BPM. The network is organized in layers of neurons, each one of them representing an x-y plane in the BPM. The output of the network is compared to the experimental measurements and the error is used to correct the weights (representing the refractive index contrast) in the neurons using standard error back propagation techniques. The algorithm yields images of better quality than other tomographic reconstruction methods. In particular, the missing cone artifact is efficiently reduced, as well as parasitic granular structures. It was shown that whether starting from a constant initial guess for the refractive index or with a conventional Radon tomographic image, the method essentially converges to the same result after 100 iterations. This approach opens rich perspectives for active correction of scattering in biological sample; in particular, it has the potential of increasing the resolution and the contrast in fluorescent and two-photon imaging.

3.6 Bibliography

- [1] B. Widrow, P. E. Mantey, Lloyd Griffiths, and B. Goode, "Adaptive antenna systems," *The Journal of the Acoustical Society of America* 42, no. 5 (1967): 1175-1176.
- [2] J. R. Fienup, "Phase-retrieval algorithms for a complicated optical system," *Applied optics*, vol. 32, no. 10 (1993): 1737-1746.
- [3] W. Van den Broek, and C. T. Koch, "Method for retrieval of the three-dimensional object potential by inversion of dynamical electron scattering," *Physical review letters* vol. 109, no. 24, 245502, 2012.
- [4] N. Joachimowicz, C. Pichot, and J.-P. Hugonin. "Inverse scattering: An iterative numerical method for electromagnetic imaging," *IEEE Transactions on Antennas and Propagation* vol. 39, no. 12 (1991): 1742-1753.
- [5] A. Abubakar, P. M. Van den Berg, and J. J. Mallorqui. "Imaging of biomedical data using a multiplicative regularized contrast source inversion method," *IEEE Transactions on Microwave Theory and Techniques*, vol. 50, no. 7 (2002): 1761-1771.
- [6] G. Maire, F. Drsek, J. Girard, H. Giovannini, A. Talneau, D. Konan, K. Belkebir, P. C. Chaumet, and A. Sentenac, "Experimental demonstration of quantitative

- imaging beyond Abbe's limit with optical diffraction tomography," *Physical review letters* 102, no. 21 (2009): 213905.
- [7] O. Haeberlè, K. Belkebir, H. Giovaninni, and A. Sentenac, "Tomographic diffractive microscopy: basics, techniques and perspectives," *Journal of Modern Optics* 57, no. 9 (2010): 686-699.
- [8] B. T. Draine, and P. J. Flatau, "Discrete-dipole approximation for scattering calculations," *JOSA A* 11, no. 4 (1994): 1491-1499.
- [9] M. H. Maleki and A. J. Devaney, "Phase-retrieval and intensity-only reconstruction algorithms for optical diffraction tomography," *JOSA A* 10(5), (1993): 1086-1092.
- [10] J. R. Fienup, "Phase retrieval algorithms: a comparison," *Appl. Opt.* 21, (1982):2758-2769
- [11] L. Tian and L. Waller, "3D intensity and phase imaging from light field measurements in an LED array microscope," *Optica*, Vol. 2, Issue 2, (2015): 104-111
- [12] U. Schnars, and W. Jueptner, "Digital holography," *Springer Berlin Heidelberg*, 2005.
- [13] Yamaguchi, Ichirou, and Tong Zhang, "Phase-shifting digital holography," *Optics letters* 22, no. 16 (1997): 1268-1270.
- [14] J. V. Roey, J. V. Donk, and P. E. Lagasse, "Beam-propagation method: analysis and assessment," *JOSA* 71, no. 7 (1981): 803-810.
- [15] J. W. Goodman, "Introduction to Fourier Optics," *McGraw-Hill*, 2 ed., 1996.
- [16] D. E. Rumelhart, G. E. Hinton, and R. J. Williams, "Learning representations by back-propagating errors," *Cognitive modeling* 5 (1988).
- [17] E. Wolf, "Three-dimensional structure determination of semi-transparent objects from holographic data," *Optics Communications* 1, no. 4 (1969): 153-156.
- [18] W. Choi, C. Fang-Yen, K. Badizadegan, S. Oh, N. Lue, R. R. Dasari, and M. S. Feld, "Tomographic phase microscopy," *Nat. Methods*, vol. 4, (2007): 717-719.
- [19] W. Choi, C. Fang-Yen, K. Badizadegan, R. R. Dasari, and M. S. Feld, "Extended depth of focus in tomographic phase microscopy using a propagation algorithm," *Optics letters* 33, no. 2 (2008): 171-173.
- [20] Y. Sung, W. Choi, C. Fang-Yen, K. Badizadegan, R. R. Dasari, and M. S. Feld, "Optical diffraction tomography for high resolution live cell imaging," *Opt. Express*, vol. 17, (2009): 266-277.

- [21] F. Charrière, A. Marian, F. Montfort, J. Kuehn, T. Colomb, E. Cuche, P. Marquet, and C. Depeursinge, "Cell refractive index tomography by digital holographic microscopy." *Optics letters* 31, no. 2 (2006): 178-180.
- [22] Y. Cotte, F. Toy, P. Jourdain, N. Pavillon, D. Boss, P. Magistretti, P. Marquet, and C. Depeursinge, "Marker-free phase nanoscopy," *Nat. Photonics*, vol. 7, no. 2, pp. 113-117, Jan. 2013.
- [23] V. Lauer, "New approach to optical diffraction tomography yielding a vector equation of diffraction tomography and a novel tomographic microscope," *Journal of Microscopy*, Vol. 205, Pt 2 February 2002, pp. 165-176
- [24] A. Beck, and M. Teboulle, "Gradient-based algorithms with applications to signal recovery," *Convex Optimization in Signal Processing and Communications* (2009).
- [25] L. Bottou, "Neural Networks: Tricks of the Trade," *ch. Stochastic Gradient Descent Tricks*, Springer, 2 ed., (2012): 421-437.
- [26] C. M. Bishop, "Neural Networks for Pattern Recognition," *Oxford*, 1995.
- [27] E. J. Candes, M. B. Wakin, and S. P. Boyd, "Enhancing sparsity by reweighted ℓ_1 minimization," *J. of Fourier Anal. Appl.*, vol. 14, (2008): 877-905.
- [28] E. Y. Sidky, M. A. Anastasio, and X. Pan, "Image reconstruction exploiting object sparsity in boundary-enhanced X-ray phase-contrast tomography," *Optics express* vol. 18, no. 10 pp. 10404-10422, 2010.
- [29] Lustig, Michael, David Donoho, and John M. Pauly. "Sparse MRI: The application of compressed sensing for rapid MR imaging," *Magnetic resonance in medicine* 58, no. 6 (2007): 1182-1195.
- [30] R. M. Lewitt, "Reconstruction algorithms: transform methods," *Proceedings of the IEEE*, vol. 71, no. 3 (1983): 390-408.
- [31] V. Lauer, "New approach to optical diffraction tomography yielding a vector equation of diffraction tomography and a novel tomographic microscope," *Journal of Microscopy* 205, no. 2 (2002): 165-176.
- [32] K. Kim, H. Yoon, M. Diez-Silva, M. Dao, R. R. Dasari, and Y. Park, "High-resolution three-dimensional imaging of red blood cells parasitized by *Plasmodium falciparum* and in situ hemozoin crystals using optical diffraction tomography," *J. Biomed. Opt.*, vol. 19, p. 011005, 2014

CHAPTER 4

Algorithm

Contents

4.1	Introduction	31
4.2	Forward model	33
4.2.1	Fourier beam-propagation	34
4.2.2	Numerical implementation	34
4.3	Proposed method	35
4.3.1	Problem formulation	37
4.3.2	Computation of the gradient	38
4.3.3	Iterative reconstruction	40
4.4	Numerical evaluation	41
4.5	Conclusion	47
4.6	Bibliography	48

Optical tomographic imaging requires an accurate forward model as well as regularization to mitigate missing-data artifacts and to suppress noise. Nonlinear forward models can provide more accurate interpretation of the measured data than their linear counterparts, but they generally result in computationally prohibitive reconstruction algorithms. Although sparsity-driven regularizers significantly improve the quality of reconstructed image, they further increase the computational burden of imaging. In this chapter, we present a novel iterative imaging method for optical tomography that combines a nonlinear forward model based on the BPM with an edge-preserving 3D total variation (TV) regularizer. The central element of our approach is a time-reversal scheme, which allows for an efficient computation of the derivative of the transmitted wave-field with respect to the distribution of the refractive index. This time-reversal scheme together with our stochastic proximal-gradient algorithm makes it possible to optimize under a nonlinear forward model in a computationally tractable way, thus enabling a high-quality imaging of the refractive index throughout the object. We demonstrate the effectiveness of our method through several experiments on simulated and experimentally measured data.

4.1 Introduction

Optical tomography is a popular and widely investigated technique for 3D quantitative imaging of biological samples. In a typical setup, the sample is illuminated with a laser over multiple angles and the scattered light is holographically

recorded giving access to both the amplitude and the phase of the light-field at the camera plane. The refractive index distribution of the sample is then numerically reconstructed from the scattered light-field by relying on a model describing the interaction between the sample and the light. Quantitative reconstruction of the refractive index is a central problem in biomedical imaging as it enables the visualization of the internal structure, as well as physical properties, of nearly transparent objects such as cells.

Most approaches for estimating the refractive index rely on various approximations to linearize the relationship between the refractive index and the measured light-field. For example, one approach is based on the straight-ray approximation and interprets the phase of the transmitted light-field as a line integral of the refractive index along the propagation direction. The reconstruction under straight-ray approximation can be performed efficiently by using the Filtered Back-Projection (FBP) algorithm [1]. Another popular approach is diffraction tomography that was proposed by Wolf [2] and later refined by Devaney [3]. DT establishes a Fourier transform-based relationship between the measured field and the refractive index, which enables the recovery of the refractive index via a single numerical application of the inverse Fourier transform. These linear approaches are typically valid only for objects that are weakly scattering; their application on highly contrasted or large objects often results in images of poor spatial resolution.

Regularization is a standard approach for improving the resolution in ODT. It provides effective means for mitigating various artifacts and for suppressing noise. For example, Choi *et al.* [4] demonstrated that, under the straight-ray approximation, the missing cone artifact, which results in elongation of the reconstructed shape and underestimation of the value of the refractive index, can be significantly reduced by iteratively imposing positivity on the refractive index. The benefits of this iterative approach was further demonstrated in the weakly-scattering regime by Sung *et al.* [5]. In recent years, sparsity-promoting regularization, which is an essential component of compressive sensing theory [6, 7], has provided more dramatic improvements in the quality of tomographic imaging [8, 9]. The basic motivation is that many optical tomographic images are inherently sparse in some transform domain and can be reconstructed with high accuracy even with low amount of measured data.

In this chapter, we present a novel iterative imaging method for optical tomography that combines sparsity-driven regularization with a *nonlinear* forward physical model of the propagation of the light-field. Specifically, our model is based on a popular technique in optics called BPM, which is extensively used for modeling diffraction and propagation effects of light-waves [10–14]. Accordingly, BPM provides a more accurate model than its linear counterparts, especially when scattering effects cannot be neglected. Unlike other nonlinear alternatives, such as the ones based on the coupled dipole approximation [15, 16], BPM has the advantage that it is reasonably fast to implement and that it can be efficiently optimized via a *time-reversal scheme*. This scheme allows computing the derivative of the transmitted light field with respect to the distribution of refractive index by simple error

backpropagation. This allows us to develop a fast iterative algorithm based on stochastic version of the proximal-gradient descent that uses measurements in an online fashion and thus, significantly reduces the memory requirements for the reconstruction. Our results demonstrate that the proposed method can reconstruct high-quality images of the refractive index even when missing significant amounts of data.

In Chapter 3, we have presented the optical and conceptual aspects of our BPM-based imaging framework [17]. Here, we complement it by providing the algorithmic details of the reconstruction and by presenting additional validations on simulated, as well as, on experimentally measured data. Our work is also related to the recent iterative optimization method by Tian and Waller [18] that was demonstrated for imaging 3D objects using incoherent illumination and intensity detection. The primary difference is that these authors use intensity measurements directly while our method relies on digital holography [19, 20] to record the complex amplitude of the field. The other improvement is on the signal processing side with the introduction of sparse regularization in order to achieve high-quality imaging with undersampled data. An interesting future work would be testing the proposed algorithm for imaging phase objects directly from their intensity measurements.

This chapter, First, in Section 4.2, we present our forward model based on BPM. Then in Section 4.3, we present our algorithmic framework for the recovery of the refractive index from the measurements of the light field. Specifically, our algorithm estimates the refractive index by minimizing a cost functional, where the data-term is based on BPM and the regularizer promotes solutions with a sparse gradient. Fundamentally, the algorithm relies on the computation of the derivatives of the forward model with respect to the refractive index, which will be presented in a great detail. In Section 4.4, we present some experimental results illustrating the performance of our algorithm on experimental as well as simulated data.

4.2 Forward model

This section presents the BPM forward model, whose complete derivation can be found in Appendix A.2. Although, BPM is a standard technique in optics for modeling propagation of light in inhomogeneous media [10–14], it is less known in the context of signal reconstruction and inverse problems. We shall denote our nonlinear forward model by $\mathbf{y} = \mathbf{S}(\mathbf{x})$, where the vector $\mathbf{y} \in \mathbb{C}^M$ contains the samples of the measured light-field, $\mathbf{x} \in \mathbb{R}^N$ is the discretized version of the refractive index, and $\mathbf{S} : \mathbb{R}^N \rightarrow \mathbb{C}^M$ is the nonlinear mapping. Note that the nonlinearity of BPM refers to the relationship between the refractive index and the measured light-field, not to the relationship between input and output light-fields, which is linear.

4.2.1 Fourier beam-propagation

The scalar inhomogeneous Helmholtz equation implicitly describes the relationship between the refractive index and the light field everywhere in space.

$$(\Delta + k^2(\mathbf{r}) \mathbf{I}) u(\mathbf{r}) = 0, \quad (4.1)$$

where $\mathbf{r} = (x, y, z)$ denotes a spatial position, u is the total light-field at \mathbf{r} , $\Delta = (\partial^2/\partial x^2 + \partial^2/\partial y^2 + \partial^2/\partial z^2)$ is the Laplacian, \mathbf{I} is the identity operator, and $k(\mathbf{r}) = \omega/c(\mathbf{r})$ is the wavenumber of the light field at \mathbf{r} . The spatial dependence of the wavenumber k is due to variations of the speed of light c induced by the inhomogeneous nature of the medium under consideration. Specifically, the wavenumber in (4.1) can be decomposed as follows

$$k(\mathbf{r}) = k_0 n(\mathbf{r}) = k_0 (n_0 + \delta n(\mathbf{r})), \quad (4.2)$$

where $k_0 = \omega/c_0$ is the wavenumber in the free space, with $c_0 \approx 3 \times 10^8$ m/s being the speed of light in free space. The quantity n is the spatially varying refractive index of the sample, which we have written in terms of the refractive index of the medium n_0 and the perturbation δn due to inhomogeneities. We assume that the refractive index is real, which is an accurate approximation when imaging weakly absorbing objects such as biological cells.

BPM is a class of algorithms designed for calculating the optical field distribution in space or in time given initial conditions. By considering the complex envelope $a(\mathbf{r})$ of the paraxial wave $u(\mathbf{r}) = a(\mathbf{r}) \exp(jk_0 n_0 z)$, one can develop BPM as an evolution equation for a in which z plays the role of evolution parameter

$$a(x, y, z + \delta z) = e^{jk_0(\delta n(\mathbf{r}))\delta z} \times \mathcal{F}^{-1} \left\{ \mathcal{F} \{a(\cdot, \cdot, z)\} \times e^{-j \left(\frac{\omega_x^2 + \omega_y^2}{k_0 n_0 + \sqrt{k_0^2 n_0^2 - \omega_x^2 - \omega_y^2}} \right) \delta z} \right\}. \quad (4.3)$$

Therefore, BPM allows to obtain the wave-field in space via alternating evaluation of diffraction and refraction steps handled in the Fourier and space domains, respectively (see Appendix A.2 for more details).

It is important to note that BPM ignores reflections. This can be seen from the fact that if the solution exists for an arbitrary initial condition $a_0 \triangleq a(x, y, z = 0)$, then a_0 does not depend on $a(\mathbf{r})$.

4.2.2 Numerical implementation

We consider a 3D volume $[-L_x/2, L_x/2] \times [-L_y/2, L_y/2] \times [0, L_z]$ that we refer to as computational domain. The domain is sampled with steps δx , δy , and δz , which will result in N_x , N_y , and K samples, respectively. We will additionally use the following matrix-vector notations

- \mathbf{x} : samples of the refractive-index distribution δn in the computational domain.
- \mathbf{y} : samples of the complex light-field a .
- \mathbf{S} : nonlinear forward operator that implements BPM and maps the refractive index distribution into the complex light-field $\mathbf{y} = \mathbf{S}(\mathbf{x})$.

We use the index k to refer to the quantities described above at the k th slice along the optical axis z . For simplicity, we assume that all 2D quantities at the k th slice are stored in a vector. Then, given the initial input field $\mathbf{y}_0 = \mathbf{S}_0(\mathbf{x})$ and the refractive index distribution \mathbf{x} , the total field $\{\mathbf{y}_k\}_{k \in [1 \dots K]}$ can be computed recursively as follows

$$\mathbf{S}_k(\mathbf{x}) = \text{Diag}(\mathbf{p}_k(\mathbf{x}_k)) \mathbf{H} \mathbf{S}_{k-1}(\mathbf{x}), \quad (4.4)$$

where the operator $\text{Diag}(\mathbf{u})$ creates a square matrix with the elements of the input vector \mathbf{u} the main diagonal. The matrix \mathbf{H} denotes the diffraction operator; it is implemented by taking the Discrete Fourier Transform (DFT) of the input field, multiplying it by a frequency-domain phase mask, and taking the inverse DFT. The vector $\mathbf{p}_k(\mathbf{x}_k) = \exp(jk_0 \delta z \mathbf{x}_k)$, which depends on the k th slice of the refractive index \mathbf{x}_k , accounts for a phase factor corresponding to the implementation of the refraction step. Finally, the measured data \mathbf{y} corresponds to the light-field at the K th slice of the computational domain, i.e., $\mathbf{y} = \mathbf{y}_K = \mathbf{S}_K(\mathbf{x})$. Note that from (4.4), one can readily evaluate the computational complexity of BPM, which roughly corresponds to $2K$ evaluations of FFT or $O(N \log(N/K))$ with $N = N_x N_y K$.

Figure 4.1 illustrates a simulation where a plane-wave of $\lambda = 561$ nm with a Gaussian amplitude is propagated in an immersion oil ($n_0 = 1.518$ at $\lambda = 561$ nm) with an angle of $\pi/32$ with respect to the optical axis z . The computational domain of dimensions $L_x = L_y = L_z = 36.86 \mu\text{m}$ is sampled with steps $\delta x = \delta y = \delta z = 144$ nm. In Figure 4.1 (a)-(c), we illustrate the propagation of the light-field in immersion oil, while in Figure 4.1 (d)-(f), we illustrate the propagation when a spherical bead of diameter $10 \mu\text{m}$ with refractive index $n = 1.548$ is immersed in the oil. As we can see in Figure 4.1 (f) even for a relatively weak refractive index contrast of $\delta n = 0.03$, one can clearly observe the effects of scattering on the magnitude of the light-field.

4.3 Proposed method

In practice, the input field \mathbf{y}_0 is known and the output field \mathbf{y}_K is measured using a holographic technique that gives access to the full complex-valued light-field. Our goal is to recover \mathbf{x} from a set of L views $\{\mathbf{y}_K^\ell\}_{\ell \in [1 \dots L]}$ corresponding to input fields $\{\mathbf{y}_0^\ell\}_{\ell \in [1 \dots L]}$. We shall denote with M the total number of measurements in a single view \mathbf{y}^ℓ and with N the total number of voxels in \mathbf{x} .

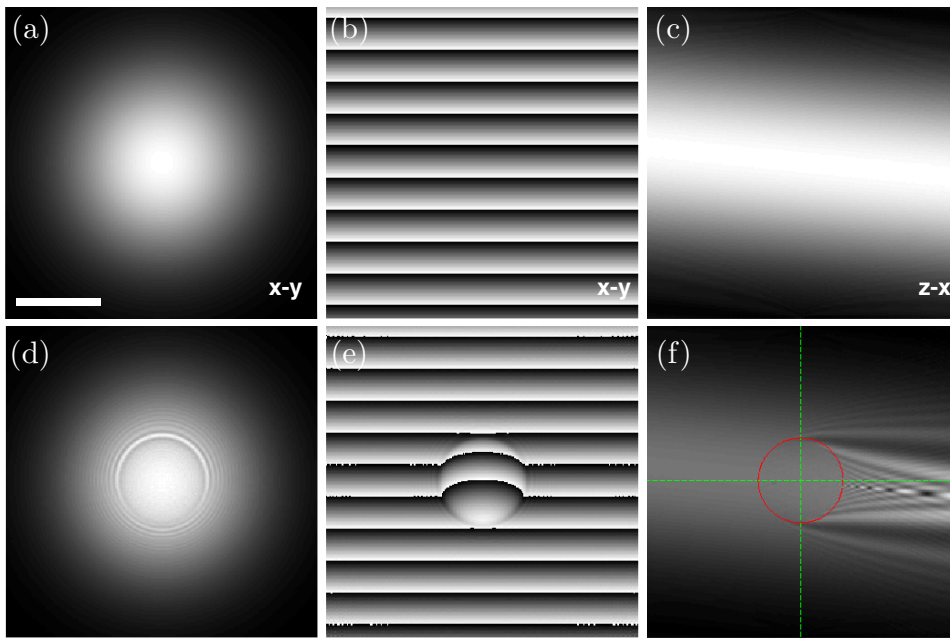


Figure 4.1: Propagation of a plane-wave of $\lambda = 561$ nm in an immersion oil with $n_0 = 1.518$ simulated with BPM. (a–c) Propagation in oil. (d–f) Immersion of a $10\ \mu\text{m}$ bead of $n = 1.548$. (a, d) x - y slice of the beam magnitude at $z = L_z/2$. (b, e) x - y slice of the beam phase at $z = L_z/2$. (c, f) x - z slice of the beam magnitude at $y = 0$. The circle in (f) illustrates the boundary of the bead at $y = 0$. Scale bar, $10\ \mu\text{m}$.

4.3.1 Problem formulation

We formulate the reconstruction task as the following minimization problem

$$\hat{\mathbf{x}} = \arg \min_{\mathbf{x} \in \mathcal{X}} \{\mathcal{C}(\mathbf{x})\} \quad (4.5a)$$

$$= \arg \min_{\mathbf{x} \in \mathcal{X}} \{\mathcal{D}(\mathbf{x}) + \tau \mathcal{R}(\mathbf{x})\}, \quad (4.5b)$$

where \mathcal{D} is the data-fidelity term and \mathcal{R} is the regularization term to be discussed shortly. The convex set $\mathcal{X} \subseteq \mathbb{R}^N$ is used to enforce certain physical constraints on the refractive index such as its non-negativity. The parameter $\tau > 0$ controls the amount of regularization.

The data fidelity term in (4.5) is given by

$$\mathcal{D}(\mathbf{x}) \triangleq \frac{1}{L} \sum_{\ell=1}^L \mathcal{D}_{\ell}(\mathbf{x}) \quad (4.6a)$$

$$\triangleq \frac{1}{2L} \sum_{\ell=1}^L \left\| \mathbf{y}_K^{\ell} - \mathbf{S}_K^{\ell}(\mathbf{x}) \right\|_{\ell_2}^2, \quad (4.6b)$$

where L denotes the number of measured views. For a given view ℓ , the forward operator \mathbf{S}_K^{ℓ} can be computed recursively via equation (4.4).

As a regularization term in (4.5), we propose to use the 3D isotropic total variation (TV) [21] of the refractive index distribution

$$\mathcal{R}(\mathbf{x}) \triangleq \sum_{n=1}^N \left\| [\mathbf{D}\mathbf{x}]_n \right\|_{\ell_2} \quad (4.7)$$

$$= \sum_{n=1}^N \sqrt{([\mathbf{D}_x \mathbf{x}]_n)^2 + ([\mathbf{D}_y \mathbf{x}]_n)^2 + ([\mathbf{D}_z \mathbf{x}]_n)^2} \quad (4.8)$$

where $\mathbf{D} : \mathbb{R}^N \rightarrow \mathbb{R}^{N \times 3}$ is the discrete counterpart of the gradient operator. The matrices \mathbf{D}_x , \mathbf{D}_y , and \mathbf{D}_z denote the finite difference operations along the x , y , and z directions, respectively (see Appendix A.3 for more details). The TV prior on images has been originally introduced by Rudin *et al.* [21] as a regularization approach capable of preserving image edges, while removing noise. It is often interpreted as a sparsity-promoting ℓ_1 -penalty on the magnitudes of the image gradient [22]. TV regularization has proven to be successful in a wide range of applications in the context of sparse recovery of images from incomplete or corrupted measurements [6, 23].

The minimization in (4.5) is a nontrivial optimization task. Keeping the regularization aside, the primary difficulty resides in the fact that the data term \mathcal{D} is based on a nonlinear forward operator \mathbf{S} . The other challenging aspects are the massive quantity of data that need to be processed and the presence of a nonsmooth regularization term \mathcal{R} . We next present a novel algorithm based on iterative stochastic proximal-gradient descend that is made tractable via the time-reversal scheme that allows for an efficient computation of the gradient of \mathcal{D} with respect to \mathbf{x} .

Algorithm 1 Time-reversal scheme for computing $\nabla \mathcal{D}^H$ **input:** input field \mathbf{y}_0 , output field \mathbf{y}_K ,and current estimate of the refractive-index distribution $\hat{\mathbf{x}}$.**output:** the gradient $[\nabla \mathcal{D}(\hat{\mathbf{x}})]^H$.**algorithm:**

1. Compute the total field $\hat{\mathbf{y}} = \mathbf{S}(\hat{\mathbf{x}})$ using the BPM recursion (4.4), keeping all the intermediate light-fields $\hat{\mathbf{y}}_k = \mathbf{S}_k(\hat{\mathbf{x}})$ in memory.
2. Compute the residual $\mathbf{r}_K = \hat{\mathbf{y}}_K - \mathbf{y}_K$ and set $\mathbf{s}_K = 0$.
3. Compute $\mathbf{s}_0 = \left[\frac{\partial}{\partial \mathbf{x}} \mathbf{S}_K(\hat{\mathbf{x}}) \right]^H \mathbf{r}_K$ using the following iterative procedure for $m = K, \dots, 1$
 - (a) $\mathbf{s}_{m-1} = \mathbf{s}_m + \left[\frac{\partial}{\partial \mathbf{x}} \mathbf{p}_m(\hat{\mathbf{x}}_m) \right]^H \text{Diag} \left(\overline{\mathbf{H} \hat{\mathbf{y}}_{m-1}} \right) \mathbf{r}_m$.
 - (b) $\mathbf{r}_{m-1} = \mathbf{H}^H \text{Diag} \left(\overline{\mathbf{p}_m(\hat{\mathbf{x}}_m)} \right) \mathbf{r}_m$.
4. Return $[\nabla \mathcal{D}(\hat{\mathbf{x}})]^H = \text{Re}\{\mathbf{s}_0\}$.

4.3.2 Computation of the gradient

The crucial component of our method is recursive computation of the gradient of \mathcal{D} with respect to \mathbf{x} , summarized in Algorithm 1, which is explained next. For notational simplicity, we consider the scenario of a single view and thus drop the indices ℓ from the subsequent derivations. The generalization of the final formula to an arbitrary number of views L is straightforward.

We start by expanding the quadratic term as

$$\begin{aligned} \mathcal{D}(\mathbf{x}) &= \frac{1}{2} \|\mathbf{y}_K - \mathbf{S}_K(\mathbf{x})\|_{\ell_2}^2 \\ &= \frac{1}{2} \langle \mathbf{y}_K, \mathbf{y}_K \rangle - \text{Re} \{ \langle \mathbf{S}_K(\mathbf{x}), \mathbf{y}_K \rangle \} + \frac{1}{2} \langle \mathbf{S}_K(\mathbf{x}), \mathbf{S}_K(\mathbf{x}) \rangle, \end{aligned} \quad (4.9)$$

where $\langle \mathbf{x}, \mathbf{z} \rangle = \mathbf{z}^H \mathbf{x}$, where the Hermitian transposition H is due to the complex nature of the quantities. We adopt the convention

$$\frac{\partial}{\partial x_j} \mathbf{S}(\mathbf{x}) = \begin{bmatrix} \frac{\partial}{\partial x_j} [\mathbf{S}(\mathbf{x})]_1 \\ \vdots \\ \frac{\partial}{\partial x_j} [\mathbf{S}(\mathbf{x})]_M \end{bmatrix}. \quad (4.10)$$

Then, the gradient is given by

$$\nabla \mathcal{D}(\mathbf{x}) = \left[\frac{\partial \mathcal{D}(\mathbf{x})}{\partial x_1} \dots \frac{\partial \mathcal{D}(\mathbf{x})}{\partial x_N} \right] \quad (4.11)$$

$$= \text{Re} \left\{ (\mathbf{S}_K(\mathbf{x}) - \mathbf{y}_K)^H \left[\frac{\partial}{\partial \mathbf{x}} \mathbf{S}_K(\mathbf{x}) \right] \right\}, \quad (4.12)$$

where

$$\begin{aligned}\frac{\partial}{\partial \mathbf{x}} \mathbf{S}_K(\mathbf{x}) &= \left[\frac{\partial}{\partial x_1} [\mathbf{S}_K(\mathbf{x})] \dots \frac{\partial}{\partial x_N} [\mathbf{S}_K(\mathbf{x})] \right] \\ &= \begin{bmatrix} \frac{\partial}{\partial x_1} [\mathbf{S}_K(\mathbf{x})]_1 & \dots & \frac{\partial}{\partial x_N} [\mathbf{S}_K(\mathbf{x})]_1 \\ \vdots & \vdots & \vdots \\ \frac{\partial}{\partial x_1} [\mathbf{S}_K(\mathbf{x})]_M & \dots & \frac{\partial}{\partial x_N} [\mathbf{S}_K(\mathbf{x})]_M \end{bmatrix}.\end{aligned}$$

In practice, we are interested in a column vector

$$[\nabla \mathcal{D}(\mathbf{x})]^H = \text{Re} \left\{ \left[\frac{\partial}{\partial \mathbf{x}} \mathbf{S}_K(\mathbf{x}) \right]^H (\mathbf{S}_K(\mathbf{x}) - \mathbf{y}_K) \right\}. \quad (4.13)$$

Therefore, we need to derive a tractable algorithm to compute (4.13). The recursive BPM formula (4.4) allows us to write

$$\begin{aligned}\frac{\partial}{\partial \mathbf{x}} \mathbf{S}_k(\mathbf{x}) &= \frac{\partial}{\partial \mathbf{x}} [\text{Diag}(\mathbf{p}_k(\mathbf{x}_k)) \mathbf{H} \mathbf{S}_{k-1}(\mathbf{x})] \\ &= \text{Diag}(\mathbf{H} \mathbf{S}_{k-1}(\mathbf{x})) \left[\frac{\partial}{\partial \mathbf{x}} \mathbf{p}_k(\mathbf{x}_k) \right] \\ &\quad + \text{Diag}(\mathbf{p}_k(\mathbf{x}_k)) \mathbf{H} \left[\frac{\partial}{\partial \mathbf{x}} \mathbf{S}_{k-1}(\mathbf{x}) \right].\end{aligned}$$

Then, we have the following equality

$$\begin{aligned}\left[\frac{\partial}{\partial \mathbf{x}} \mathbf{S}_k(\mathbf{x}) \right]^H &= \left[\frac{\partial}{\partial \mathbf{x}} \mathbf{S}_{k-1}(\mathbf{x}) \right]^H \mathbf{H}^H \text{Diag}(\overline{\mathbf{p}_k(\mathbf{x}_k)}) \\ &\quad + \left[\frac{\partial}{\partial \mathbf{x}} \mathbf{p}_k(\mathbf{x}_k) \right]^H \text{Diag}(\overline{\mathbf{H} \mathbf{S}_{k-1}(\mathbf{x})}),\end{aligned} \quad (4.14)$$

where the vector $\bar{\mathbf{v}}$ contains complex conjugated elements of vector \mathbf{v} . Also, note that since the input field is known and does not depend on \mathbf{x} , for $k = 0$, we have

$$\left[\frac{\partial}{\partial \mathbf{x}} \mathbf{S}_0(\mathbf{x}) \right]^H = \mathbf{0}. \quad (4.15)$$

Based on the recursion (4.14) with the boundary condition (4.15), we obtain a practical implementation of (4.13), which is summarized in Algorithm 1. Conceptually, our method is similar to the *error backpropagation algorithm* extensively used in deep learning for neural networks [24]. Similarly, to backpropagation, we compute the gradient by propagating the error in a *time-reversed* fashion. Computational complexity of the time-reversal scheme is of the same order as that of BPM and essentially corresponds to a constant number of K FFTs of $N_x \times N_y$ images.

Algorithm 2 Minimizes: $\mathcal{C}(\mathbf{x}) = \mathcal{D}(\mathbf{x}) + \tau\mathcal{R}(\mathbf{x})$

input: light-field data $\{\mathbf{y}^\ell\}_{\ell \in [1 \dots L]}$, initial guess $\hat{\mathbf{x}}^0$, steps $\{\gamma_t\}_{t \in \mathbb{N}}$, regularization parameter $\tau > 0$, and parameter $\tilde{L} \in [1 \dots L]$.

set: $t \leftarrow 1, \mathbf{s}^0 \leftarrow \hat{\mathbf{x}}^0, q_0 \leftarrow 1$

repeat

Select randomly with equal probability a subset of \tilde{L} views. We index them with $\{\ell_i\}_{i \in [1 \dots \tilde{L}]}$

$\mathbf{z}^t \leftarrow \mathbf{s}^{t-1} - (\gamma_t / \tilde{L}) \sum_{i=1}^{\tilde{L}} \nabla \mathcal{D}_{\ell_i}(\mathbf{s}^{t-1})$

$\hat{\mathbf{x}}^t \leftarrow \text{prox}_{\mathcal{R}}(\mathbf{z}^t, \gamma_t \tau)$

$q_t \leftarrow \frac{1}{2} \left(1 + \sqrt{1 + 4q_{t-1}^2} \right)$

$\mathbf{s}^t \leftarrow \hat{\mathbf{x}}^t + ((q_{t-1} - 1) / q_t)(\hat{\mathbf{x}}^t - \hat{\mathbf{x}}^{t-1})$

$t \leftarrow t + 1$

until stopping criterion

return estimate of the refractive index $\hat{\mathbf{x}}^t$

4.3.3 Iterative reconstruction

By relying on the time-reversal scheme, we propose a novel algorithm, summarized in Algorithm 2, that reconstructs the refractive index \mathbf{x} from optical tomographic measurements $\{\mathbf{y}_K^\ell\}_{\ell \in [1 \dots L]}$. Conceptually, the algorithm is similar to the *Fast Iterative Shrinkage/Thresholding Algorithm (FISTA)* [25], which is a popular approach for minimizing cost-functions that consist of sums between smooth and nonsmooth terms. One notable difference of Algorithm 2 with respect to FISTA, summarized in Algorithm 3 of Appendix A.3 is that the gradient is only computed with respect to $\tilde{L} \leq L$ measurements selected with equal probability, at each iteration, from the complete set of measurements $\{\mathbf{y}_K^\ell\}_{\ell \in [1 \dots L]}$. For $\tilde{L} \ll L$, this *incremental proximal-gradient* approach [26] reduces the per-iteration cost of reconstruction significantly; moreover, since gradient computation for our BPM model is highly parallelizable the number \tilde{L} can be adapted to match the number of available processing units. Also, the overall convergence of Algorithm 2 can be substantially faster to that of full FISTA in Algorithm 3. To understand this, consider an example where the measured views of the object are the same or very similar. Then, the partial gradient in Algorithm 2 will require $(L - \tilde{L})$ times less computation, but will still point to the right direction. A more detailed discussion on the benefits of incremental algorithms for solving very large scale optimization problems can be found in the recent work by Bertsekas [26].

A crucial step in Algorithm 2 is the proximal operator for the regularizer \mathcal{R}

$$\text{prox}_{\mathcal{R}}(\mathbf{z}, \tau) \triangleq \arg \min_{\mathbf{x} \in \mathcal{X}} \left\{ \frac{1}{2} \|\mathbf{x} - \mathbf{z}\|_{\ell_2}^2 + \tau \mathcal{R}(\mathbf{x}) \right\}. \quad (4.16)$$

The proximal operator corresponds to the regularized solution of the denoising problem with the forward operator corresponding to identity. Note that although our proximal operator for 3D TV regularizer does not admit a closed form, it can be

efficiently computed [25, 27–29]. Here, we rely on the dual minimization approach that was proposed by Beck and Teboulle [25], which we review in Appendix A.3 and summarize in Algorithm 4.

The theoretical convergence of our algorithm is difficult to analyze due to non-linear nature of \mathbf{S} . However, in practice, we found that by providing the algorithm with a warm initialization and by setting the steps of the algorithm γ_t proportional to $1/\sqrt{t}$, the algorithm achieves excellent results as reported in Section 4.4. The progressive reduction in γ_t is commonly done for ensuring the convergence of incremental proximal-gradient algorithms [26]. One practical approach for finding a warm initializer is to use the standard FBP algorithm that assumes a straight ray approximation. When imaging semi-transparent objects such as cells, even simpler but sufficient initialization is a constant value. Additionally, we fix the maximal number of iterations for the algorithm to t_{\max} and select an additional stopping criterion based on measuring the relative change of the solution in two successive iterations as

$$\frac{\|\hat{\mathbf{x}}^t - \hat{\mathbf{x}}^{t-1}\|_{\ell_2}}{\|\hat{\mathbf{x}}^{t-1}\|_{\ell_2}} \leq \delta, \quad (4.17)$$

where we use $\delta = 10^{-4}$ in all the experiments.

4.4 Numerical evaluation

Based on the above developments, we report the results of our iterative reconstruction algorithm in simulated and experimental configurations. The specifics of our experimental setup were discussed in Chapter 3. Essentially, the setup is holographic, which means that a laser source of $\lambda = 561$ nm is split into the reference and sample beams that are combined into a hologram, which is subsequently used to extract the complex light field at the measurement plane [30].

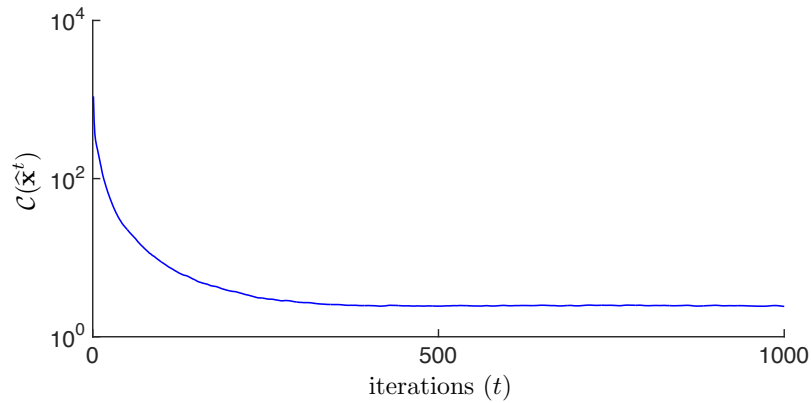


Figure 4.2: Evolution of the cost $\mathcal{C}(\hat{\mathbf{x}}^t)$ during the reconstruction over 1000 iterations for a $10\ \mu\text{m}$ bead in immersion oil.

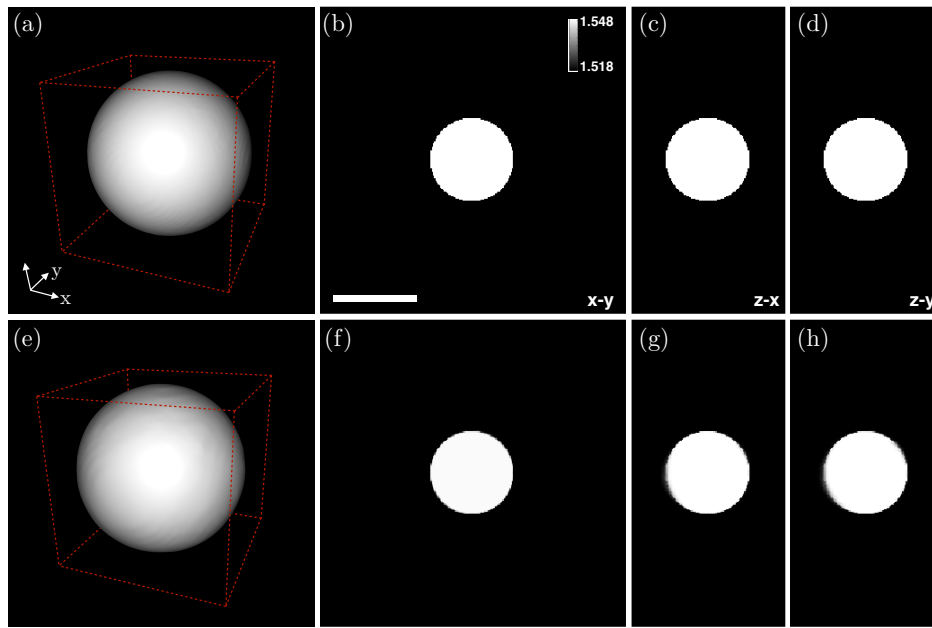


Figure 4.3: Reconstruction of a $10\ \mu\text{m}$ bead of refractive index 1.548 in an immersion oil with $n_0 = 1.518$ from BPM simulated measurements. (a–d) True refractive index distribution. (e–h) Reconstructed refractive index distribution: SNR = 22.74 dB. (a, e) A 3D rendered image of the bead. (b, f) x - y slice of the bead at $z = L_z/2$. (c, g) z - x slice of the bead at $y = 0$. (d, h) z - y slice of the bead at $x = 0$. Scale bar, $10\ \mu\text{m}$.

We first tested our BPM-based reconstruction algorithm on simulated data. In particular, we considered the reconstruction of a simple $10\ \mu\text{m}$ bead of refractive index $n = 1.548$ immersed into oil of refractive index $n_0 = 1.518$. We simulated $L = 61$ measurements with equally spaced angles in $[-\pi/8, \pi/8]$ with BPM. The illumination beam is tilted perpendicular to the y axis, while the angle is specified with respect to the optical axis z . The dimension of computational domain is set to $L_x = L_y = 36.86\ \mu\text{m}$ and $L_z = 18.45\ \mu\text{m}$ and it is sampled with steps $\delta x = \delta y = \delta z = 144\ \text{nm}$. The reconstruction is performed via the proposed approach in Algorithm 2 with $\mathcal{X} = \{\mathbf{x} \in \mathbb{R}^N : 0 \leq \mathbf{x} \leq 0.1\}$, $\tilde{L} = 8$, and $\tau = 0.01$. In Figure 4.2, we illustrate the convergence of the algorithm by plotting the cost \mathcal{C} for 1000 iterations. In Figure 4.3, we show the true and reconstructed refractive index distributions. The final SNR of the solution is 22.74 dB. The visual quality of the reconstruction is excellent; we can observe that on simulated data, the method corrects the missing cone due to limited angle of illumination and yields a sharp image along the z -axis.

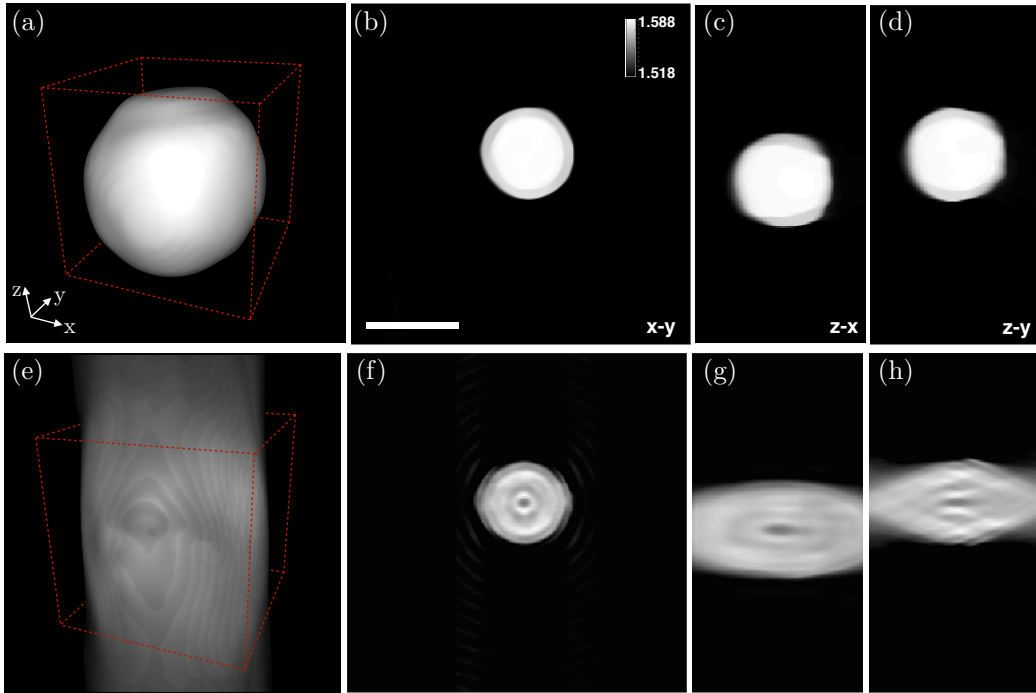


Figure 4.4: Reconstruction of a $10\ \mu\text{m}$ bead of refractive index 1.588 in an immersion oil with $n_0 = 1.518$ from experimentally measured data. (a–d) Reconstruction using our algorithm. (e–h) Reconstruction using the FBP algorithm. (a, e) A 3D rendered image of the bead. (b, f) x - y slice of the bead at $z = 21.17\ \mu\text{m}$. (c, g) z - x slice of the bead at $y = -2.30\ \mu\text{m}$. (d, h) z - y slice of the bead at $x = 0.58\ \mu\text{m}$. Scale bar, $10\ \mu\text{m}$.

We next validate the BPM forward model and our reconstruction algorithm on a similar dataset that was obtained experimentally. The sample is a $10\ \mu\text{m}$ polystyrene bead of refractive index $n = 1.588$ immersed in oil with a refractive

index of $n_0 = 1.518$ so that the refractive index contrast is $\delta n = 0.07$. The data was obtained by collecting $L = 61$ measurements with equally spaced angles in the range $[-32.16^\circ, 30.80^\circ]$. We perform reconstruction with the regularization parameter $\tau = 10$. In Figure 4.4 (a)–(d), we show the result that was obtained by initializing our algorithm with the solution of the standard FBP performed on the phase of the measured wave field. The FBP approach assumes a straight ray approximation and its results are illustrated in Figure 4.4 (e)–(h). Note that such a warm initialization is useful due to the non-convex nature of our optimization problem. In the x - y slice at $z = 21.17 \mu\text{m}$, the bead reconstructed with our method has the diameter of approximately $10.08 \mu\text{m}$ and an average refractive index of 0.067. As we can see, one of the major benefits of using the proposed method is the correction of the missing cone that is visible in Figures 4.4 (g) and (h).

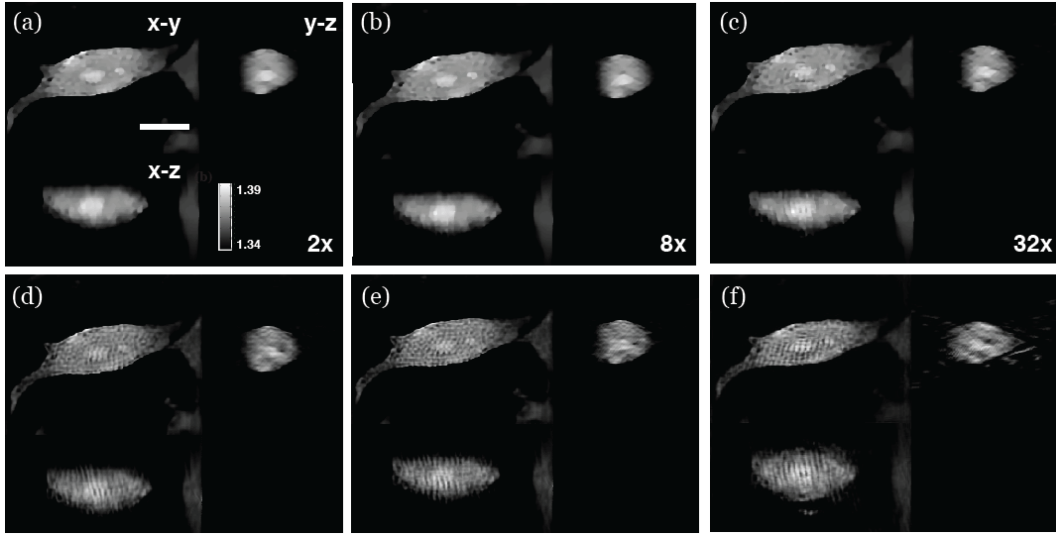


Figure 4.5: Reconstruction with a proposed method of a $37 \times 37 \times 30 \mu\text{m}$ sample containing a HeLa cell for various values of the data-reduction factor. (a–c) Reconstruction with gradient-sparsity and positivity. (d–f) Reconstruction only with positivity. (a, d) $2\times$ data reduction. (b, e) $8\times$ data reduction. (c, f) $32\times$ data reduction. Scale bar, $10 \mu\text{m}$.

Next, we investigated the ability of our method to reconstruct real biological samples from limited amounts of data. Specifically, we illuminated a sample containing a HeLa cell at 161 distinct angles uniformly distributed in the range $[-45^\circ, 45^\circ]$. The data was used for imaging a volume of size $37 \times 37 \times 30 \mu\text{m}$ ($\delta x = \delta y = \delta z = 72 \text{ nm}$). In this experiment, the data-reduction or undersampling factor refers to the ratio between the total number of holograms 161 and the actual number used for reconstruction. In particular, data-reduction factors 2, 4, 8, 16, and 32 correspond to 81, 41, 21, 11, and 6 holograms used for reconstruction, respectively. We illustrate the reconstruction results in Figure 4.5, where we compare the results of the proposed BPM-based method with and without TV regularization. We again initialize the algorithms with the volume that was obtained by running

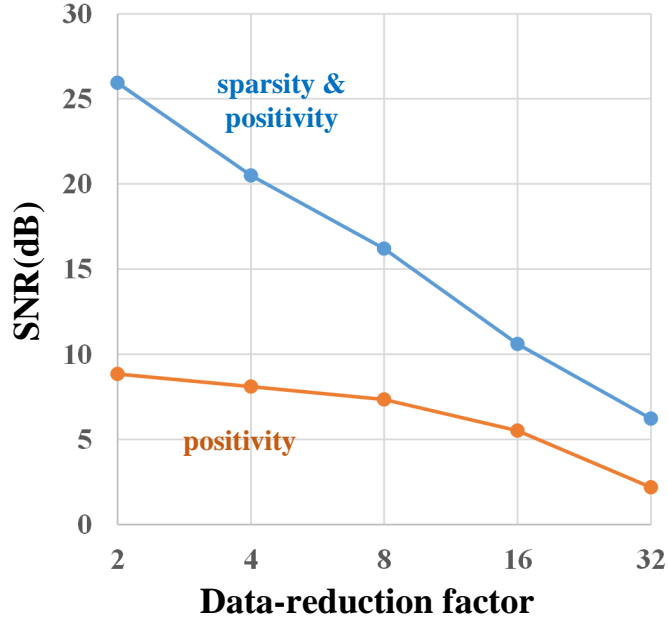


Figure 4.6: The SNR (see text) versus the data-reduction factor for the proposed learning tomography reconstruction method with and without sparsity constraint.

the standard FBP algorithm that assumes straight ray propagation. However, we observed that the algorithm is robust in the sense that it typically converges to the same solution independently of the initializer (also see Figure 4.5). To quantify the quality of the reconstructed volume as a function of data-reduction factor, we also defined

$$\text{SNR (dB)} \triangleq 10 \log_{10} \left(\frac{\|\mathbf{x}_{\text{ref}}\|_{\ell_2}^2}{\|\mathbf{x}_{\text{ref}} - \hat{\mathbf{x}}\|_{\ell_2}^2} \right),$$

where \mathbf{x}_{ref} is the reconstructed volume from all the 161 possible measurements. Figure 4.6 illustrates the evolution of the SNR with undersampling rate. As it can be seen, the sparse-regularization plays a critical role and significantly boosts the quality of the solution at all undersampling rates. Also note that the result in Figure 4.6 (c) was obtained by using only 6 holograms of size 512×512 for reconstructing a signal of size $512 \times 512 \times 400$ voxels, which corresponds to data-to-parameter ratio of 1.5/100.

In Figure 4.7, we highlight the importance of sparsity-driven iterative reconstruction. Specifically, we compare our algorithm, where the TV proximal operator is applied at each iteration, against an algorithm that first reconstructs the refractive index only with positivity constraints and then applies 3D TV denoising to the final result. Although both algorithm rely on BPM, by imposing the gradient sparsity at every iteration our algorithm converges to a visibly higher-quality solution.

In Figure 4.8, we compare the performance of our algorithms against two stan-

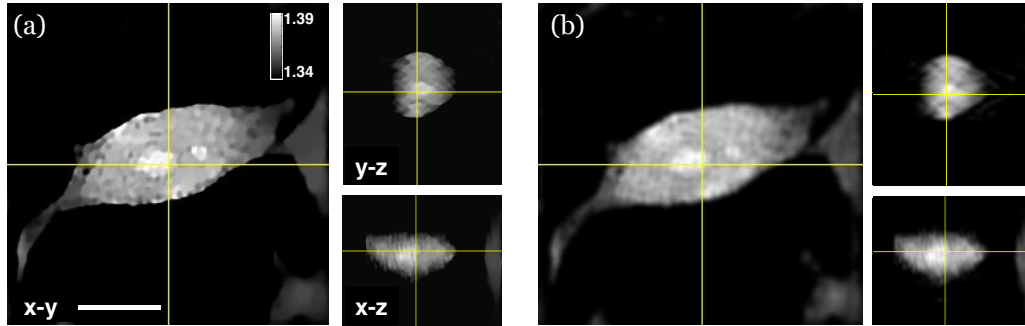


Figure 4.7: Comparison of the proposed method on a HeLa cell when applying the proximal operator (a) at every iteration, (b) only once at the end for denoising purposes. The proximal operator imposes sparsity on the gradient of the image. This figure illustrates the benefits of imposing sparsity which influences the convergence to a better solution. Scale bar, $10\ \mu\text{m}$.

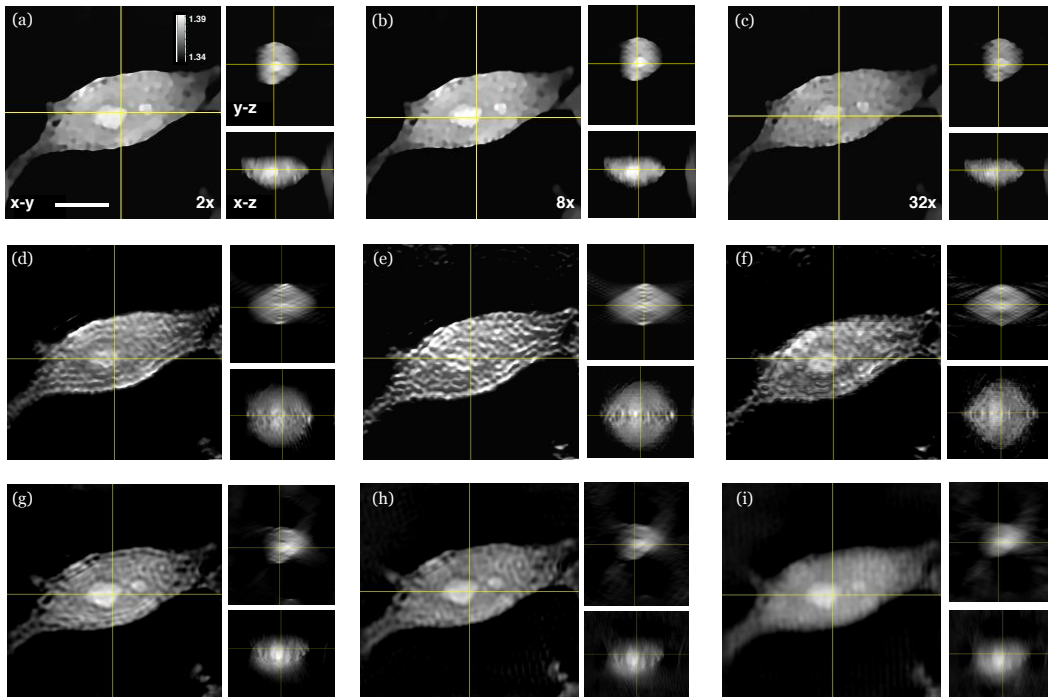


Figure 4.8: Comparison of three reconstruction algorithms for various levels of data-reduction on a sample of size $37 \times 37 \times 30\ \mu\text{m}$ containing a HeLa cell. (a–c) Proposed method. (d–f) Iterative reconstruction based on a straight ray approximation [4]. (g–i) Iterative reconstruction based on diffraction tomography [31]. (a, d, g) $2\times$ data reduction. (b, e, h) $8\times$ data reduction. (c, f, i) $32\times$ data reduction. Scale bar, $10\ \mu\text{m}$.

dard iterative algorithms that are commonly used in practice. The first one, whose results are shown in Figure 4.8 (d)-(f), is based on the algorithm that was proposed by Choi *et al.* [4]. It assumes a straight ray propagation of the light through the medium and iteratively minimizes the quadratic distance between the true and predicted phase measurements under positivity constraints. This iterative approach is an improvement over FBP and was shown to yield high quality results when imaging biological samples [4]. The second method, whose results are shown in Figure 4.8 (g)-(i), was proposed by Kim *et al.* [31] and is based on DT. DT improves over the straight ray approximation by incorporating diffraction effects due to inhomogeneities in the sample into the forward model. As can be seen, our proposed method yields sharper and higher-quality images with a significant reduction in the missing cone artifacts.

4.5 Conclusion

We have presented the algorithm of a novel computational method for the estimation of the refractive index distribution of a 3D object from the measurements of the transmitted light-field. Our method relies on a nonlinear forward model, which is based on simulating the physical propagation of electromagnetic waves with BPM. We compensated the ill-posedness of the inverse problem, by imposing positivity as well as the gradient-sparsity to the solution. The method is computationally efficient due to the time-reversal scheme for computing the gradients and the fact that only a subset of gradients are evaluated at every iteration. Overall, we believe that our approach opens rich perspectives for high-resolution tomographic imaging in a range of practical setups. We have demonstrated the use of the method for experimentally reconstructing a polystyrene bead as well as a HeLa cell immersed in oil and water, respectively. Even when the number of measurements is severely restricted, the method can recover images of surprisingly high-quality.

There are several limitations that may be addressed in future work. Although, in practice, we did not encounter any convergence problems, the nonlinear nature of the forward model makes the theoretical convergence of the method difficult to analyze. Since the proposed BPM optimization scheme is similar to the error back-propagation algorithm used for training deep neural networks [32], there may be some benefit in transposing the analysis techniques that are being rapidly developed there to our framework.

In our current experimental setup the measurements are obtained by only changing the illumination angle. However, our forward model can handle arbitrary illumination patterns. This makes it much more general than its linear counterparts that are based on Radon or on diffraction tomography. Accordingly, another avenue of work would be to investigate the performance of the proposed method under different and less standard types of illumination.

4.6 Bibliography

- [1] A. C. Kak and M. Slaney, "*Principles of Computerized Tomography Imaging*". IEEE, 1988.
- [2] E. Wolf, "Three-dimensional structure determination of semi-transparent objects from holographic data," *Opt. Commun.*, vol. 1, no. 4, pp. 153–156, September/October 1969.
- [3] A. J. Devaney, "Inverse-scattering theory within the Rytov approximation," *Opt. Lett.*, vol. 6, no. 8, pp. 374–376, August 1981.
- [4] W. Choi, C. Fang-Yen, K. Badizadegan, S. Oh, N. Lue, R. R. Dasari, and M. S. Feld, "Tomographic phase microscopy," *Nat. Methods*, vol. 4, no. 9, pp. 717–719, September 2007.
- [5] Y. Sung, W. Choi, C. Fang-Yen, K. Badizadegan, R. R. Dasari, and M. S. Feld, "Optical diffraction tomography for high resolution live cell imaging," *Opt. Express*, vol. 17, no. 1, pp. 266–277, December 2009.
- [6] E. J. Candès, J. Romberg, and T. Tao, "Robust uncertainty principles: Exact signal reconstruction from highly incomplete frequency information," *IEEE Trans. Inf. Theory*, vol. 52, no. 2, pp. 489–509, February 2006.
- [7] D. L. Donoho, "Compressed sensing," *IEEE Trans. Inf. Theory*, vol. 52, no. 4, pp. 1289–1306, April 2006.
- [8] M. M. Bronstein, A. M. Bronstein, M. Zibulevsky, and H. Azhari, "Reconstruction in diffraction ultrasound tomography using nonuniform FFT," *IEEE Trans. Med. Imag.*, vol. 21, no. 11, pp. 1395–1401, November 2002.
- [9] Y. Sung and R. R. Dasari, "Deterministic regularization of three-dimensional optical diffraction tomography," *J. Opt. Soc. Am. A*, vol. 28, no. 8, pp. 1554–1561, August 2011.
- [10] H. J. Breaux, "An analysis of mathematical transformations and a comparison of numerical techniques for computation of high-energy CW laser propagation in an inhomogeneous medium," Ballistic Research Laboratories Aberdeen Proving Ground, Maryland, Tech. Rep., June 1974.
- [11] J. Wallace and J. Q. Lilly, "Thermal blooming of repetitively pulsed laser beams," *J. Opt. Soc. Am.*, vol. 64, no. 12, 1974.
- [12] J. A. Fleck, J. R. Morris, and M. D. Feit, "Time-dependent propagation of high energy laser beams through the atmosphere," *Appl. Phys.*, vol. 10, no. 2, pp. 129–160, June 1976.

- [13] W. G. Tam, "Split-step fourier-transform analysis for laser-pulse propagation in particulate media," *J. Opt. Soc. Am.*, vol. 72, no. 10, pp. 1311–1316, October 1982.
- [14] A. Goy, "Imaging and microscopy in linear and nonlinear media using digital holography," Ph.D. dissertation, École polytechnique fédérale de Lausanne, January 2013, thesis number 5617.
- [15] G. Maire, F. Drsek, J. Girard, H. Giovaninni, A. Talneau, D. Konan, K. Belkebir, P. C. Chaumet, and A. Sentenac, "Experimental demonstration of quantitative imaging beyond Abbe's limit with optical diffraction tomography," *Phys. Rev. Lett.*, vol. 102, p. 213905, May 2009.
- [16] O. Haeberlé, K. Belkebir, H. Giovaninni, and A. Sentenac, "Tomographic diffractive microscopy: basic, techniques, and perspectives," *J. Mod. Opt.*, vol. 57, no. 9, pp. 686–699, May 2010.
- [17] U. S. Kamilov, I. N. Papadopoulos, M. H. Shoreh, A. Goy, C. Vonesch, M. Unser, and D. Psaltis, "Learning approach to optical tomography," *Optica*, vol. 2, no. 6, pp. 517–522, June 2015.
- [18] L. Tian and L. Waller, "3D intensity and phase imaging from light field measurements in an LED array microscope," *Optica*, vol. 2, pp. 104–111, 2015.
- [19] I. Yamaguchi and T. Zhang, "Phase-shifting digital horography," *Opt. Lett.*, vol. 22, pp. 1268–1270, 1997.
- [20] U. Schnars and W. Jueptner, "*Digital Horography*," Springer, 2005.
- [21] L. I. Rudin, S. Osher, and E. Fatemi, "Nonlinear total variation based noise removal algorithms," *Physica D*, vol. 60, no. 1–4, pp. 259–268, November 1992.
- [22] M. Unser and P. Tafti, "*An Introduction to Sparse Stochastic Processes*," Cambridge Univ. Press, 2014.
- [23] E. Bostan, U. S. Kamilov, M. Nilchian, and M. Unser, "Sparse stochastic processes and discretization of linear inverse problems," *IEEE Trans. Image Process.*, vol. 22, no. 7, pp. 2699–2710, July 2013.
- [24] C. M. Bishop, "*Neural Networks for Pattern Recognition*," Oxford, 1995.
- [25] A. Beck and M. Teboulle, "Fast gradient-based algorithm for constrained total variation image denoising and deblurring problems," *IEEE Trans. Image Process.*, vol. 18, no. 11, pp. 2419–2434, November 2009.
- [26] D. P. Bertsekas, "Incremental proximal methods for large scale convex optimization," *Math. Program. Ser. B*, vol. 129, pp. 163–195, 2011.

- [27] M. V. Afonso, J. M. Bioucas-Dias, and M. A. T. Figueiredo, "Fast image recovery using variable splitting and constrained optimization," *IEEE Trans. Image Process.*, vol. 19, no. 9, pp. 2345–2356, September 2010.
- [28] U. S. Kamilov, E. Bostan, and M. Unser, "Variational justification of cycle spinning for wavelet-based solutions of inverse problems," *IEEE Signal Process. Lett.*, vol. 21, no. 11, pp. 1326–1330, November 2014.
- [29] Z. Qin, D. Goldfarb, and S. Ma, "An alternating direction method for total variation denoising," *Optim. Method Softw.*, vol. 30, no. 3, pp. 594–615, 2015.
- [30] A. Bourquard, N. Pavillon, E. Bostan, C. Depeursinge, and M. Unser, "A practical inverse-problem approach to digital holographic reconstruction," *Opt. Express*, vol. 21, no. 3, pp. 3417–3433, February 2013.
- [31] T. Kim, R. Zhou, M. Mir, S. Babacan, P. Carney, L. Goddard, and G. Popescu, "White-light diffraction tomography of unlabelled live cells," *Nat. Photonics*, vol. 8, pp. 256–263, March 2014.
- [32] Y. LeCun, Y. Bengio, and G. Hinton, "Deep learning," *Nature*, vol. 521, pp. 436–444, May 28, 2015.

Imaging Thick Samples

Contents

5.1 Introduction	51
5.2 Experimental apparatus and sample preparation	53
5.3 Results	54
5.4 Conclusion	58
5.5 Bibliography	60

The vast majority of ODT experiments reported to date have been 3D images of single cells or beads demonstrating excellent image quality and sectioning capability. The sample thickness in these experiments is 10 to 20 μm and the accumulated phase is generally well below 2π . In this chapter, we explore ODT when the sample consists of multiple layers of cells. We assess experimentally the impact of sample thickness for the different ODT reconstruction algorithms and we describe a strategy that allows us to image, for the first time, multi-cell clusters.

5.1 Introduction

Optical tomography [1–11] and related techniques are unique tools to quantitatively measure the three-dimensional refractive index distributions of weakly absorbing samples. In general, the method relies on the measurement of the optical field scattered from a sample illuminated with a set of known incident fields. The incidence angle of the illumination plane wave is usually the parameter that is varied and the scattered field is measured for each incident wave. In the initial studies [3], the sample was rotated and the scattered field was collected in a transmission geometry. In more recent works, the sample is placed in a conventional microscope and the angle of illumination is changed, within the range of angles allowed by the numerical aperture of the objective lenses [2, 4–6]. In order to reconstruct the object from the collection of the scattered fields, a propagation model has to be assumed. The simplest model relies on the assumption of straight rays along which the phase is equal to the integral of the optical path. In that case, the Radon inverse transform or filtered-back projection can be used [12]. However, in many cases, such as in biological samples, the features of interest have sizes comparable to the optical wavelength used to probe them. Therefore, the

first significant improvement over the straight ray approximation comes by taking the effect of diffraction into account. This idea was introduced in the seminal paper by Emil Wolf [1] and led to the technique that is now widely referred to as ODT. In the paper by Wolf, the forward model was based on the first order Born approximation that assumes the scattered field to be negligible with respect to the incident field. The first order Born approximation is equivalent to the assumption of single scattering and is therefore limited to samples that are weakly scattering. Another significant improvement was brought to the technique by suggesting the use of the Rytov approximation instead of the first Born approximation [8, 9]. Like the first order Born approximation, the first order Rytov approximation is also a linearization of the inverse scattering problem but it has been found to yield superior results for biological cells and has been the most commonly used technique for linear ODT. We believe the main reason for the superiority of the Rytov model over the Born model is the phase unwrapping that is explicit in the Rytov model. This unwrapped phase is used instead of the field in the inversion formula introduced by Wolf (which we refer to as the Wolf transform). However, this substitution is the source of severe defocus-like distortions in the reconstruction for thick objects in sections far from the plane in which the measurement has been taken. In fact, due to this limitation essentially all experimental demonstrations of ODT use thin samples, typically single cells. The solution to correct this distortion is to refocus the measurement to the plane of interest before unwrapping the phase and applying the Wolf transform. This technique, referred to as the hybrid approach [13], has been already described in the field ultrasound imaging [14], but has been only recently characterized in optics [15]. We refer to this method as the Refocused Rytov method in which we digitally propagate the measured complex field to some other depth and do the reconstruction calculation there. A similar work was also published in optics regarding the refocusing of the scattered field when the straight rays approximation is used [16]. The main limitation of both the first order Born and Rytov approximation based models is that they rely on the first order approximation, which is obviously violated in thicker and denser objects. In the Born and Rytov formalism, each slice of the object scatters the light independently. This is of course not true when the field incident on a particular slice is distorted by the slices upstream or, similarly, when the field scattered for the slice is distorted by other slices downstream.

It has been shown recently that it is possible to incorporate multiple scattering by using a nonlinear forward model [17, 18]. In this earlier work [17–19], we introduced LT, a beam propagation based optimization technique that makes use of machine learning concepts. We recently showed that this method is superior in solving the inverse scattering problem posed by strongly scattering objects [20].

In this chapter, we experimentally demonstrate the use of the LT and the refocused Rytov techniques for thick samples consisting of clusters of yeast cells. We used agarose gels to assemble cells into samples of variable optical density and thickness for the purpose of exploring the limit of tomography techniques as thickness and scattering increases. In particular, we show that the LT algorithm

produces well focused images throughout the volume of the sample when the Rytov solution that is refocused on only a subset of planes (one or several) is used as the initial condition. In addition, the LT algorithm generally yields images of superior quality, displaying less background noise than the Rytov solution and sharper features.

5.2 Experimental apparatus and sample preparation

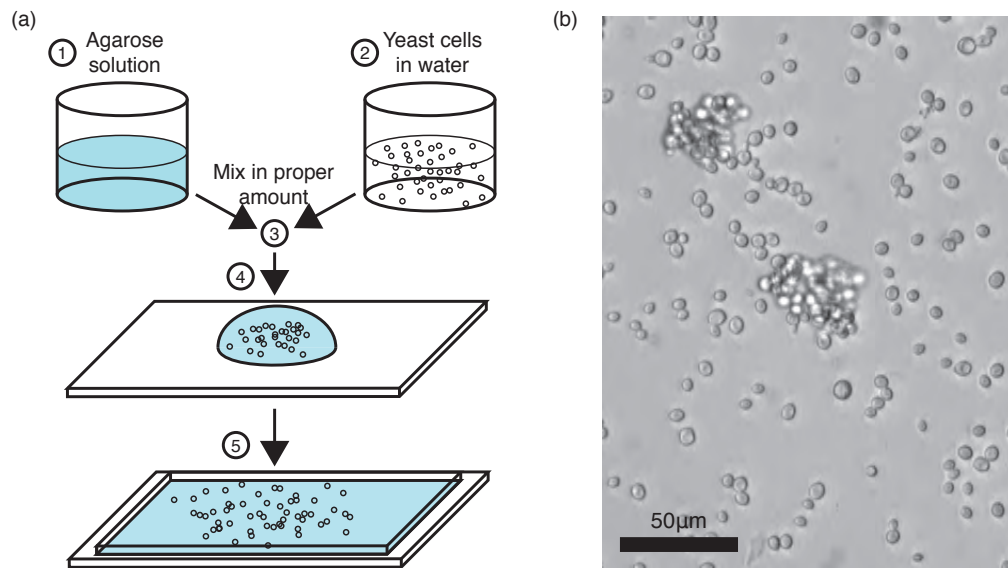


Figure 5.1: **Sample preparation.** (a) Step 1: A solution of typically 1% agarose is prepared and heated to 80°C. Step 2: The yeast cells are dispersed in aqueous solution with the desired concentration. Step 3: the cells are mixed with the agarose solution when the latter has cooled down to a temperature of 35°C. Step 4: A controlled amount of the mixed solution is put on the cover slip using a micro-pipette. The amount of liquid determines the thickness of the finished sample. Step 5: A 150 micron thick cover slip is placed on the solution that spreads in-between the slides. The two slides are then sealed using epoxy glue. (b) Wide field transmission (incoherent white light) image of a typical sample of yeast cells clusters mounted between cover slips.

The samples used in our experiments were live yeast cells dispersed in a three-dimensional agarose gel. The yeast cells are diluted in a Phosphate Buffer Saline (PBS) solution at the desired concentration at room temperature. A water solution containing 0.7% agarose is heated up to 80°C and then left to cool down to 35°C at which point a drop of the PBS solution containing the yeast cells is added. The resulting solution is placed between cover slips and left to cool down to room temperature where it solidifies (becomes like jello). This results in a stable three-dimensional arrangement of cells. Yeast cells remain alive for at least 24 hours in agarose. The distance between the cells can be adjusted by varying the initial concentration of cells. The refractive index of agarose is virtually the same as water

($n=1.34$ at 406nm). The index of refraction of the yeast cells has an index difference to the agarose on the average $\Delta n = 0.07$. In Figure 5.1, we show the process for preparing the cell cluster and a typical sample under wide field illumination in a standard microscope.

The sample is placed between two objectives (Olympus UPlanSApo NA1.40 on the collection side, and Olympus UPlanFI NA1.30 on the detection side) with a working distance in oil of $130\mu\text{m}$ and $200\mu\text{m}$ respectively, not including the cover slips. The thickness of each of cover slips was $150\mu\text{m}$. This leaves enough room for a sample with thickness up to $260\mu\text{m}$ in water (30 microns are accounted for the oil between the lenses and the cover slips). We tested samples of up to $40\mu\text{m}$ in thickness corresponding to 7 or 8 layers of yeast cells.

5.3 Results

The images in Figure 5.2 display the reconstruction of the 3D index of refraction of a sample consisting of 2 layers of yeast cells with a total thickness less than $20\mu\text{m}$. Three different reconstruction methods are shown. The first is based on the Rytov approximation. The second column presents the results obtained with the refocused Rytov method. Finally, the results obtained using LT, a nonlinear forward model accounting for multiple scattering, are also shown in the third column. The results presented in Figure 5.2 demonstrate that refocused Rytov extends the size of the reconstructed object in the z direction (the depth of field). The top row in Figure 5.2 (a, d and g) shows the reconstruction of the slice of the object that was situated in the focal plane of the imaging objective (see Figure 3.1). In other words, the image of this plane was in focus on the detector when the holograms were recorded.

The second row Figure 5.2(b, e and h) presents the reconstruction of a slice of the sample $6.4\mu\text{m}$ away from the plane of best focus. The simple Rytov reconstruction becomes distorted at this position. For ODT algorithms (such as the Born and LT algorithms) which use the detected complex field to form the 3D image of the object, the detected signal can be refocused through post-detection digital propagation. In particular, this is automatically accomplished as part of the LT reconstruction algorithm. The Rytov method on the other hand, requires that the complex phase is extracted from the hologram. For a slice away from $z = 0$, the portion of the detected signal that is due to scattering from this slice is defocused and so is the measured phase. The defocused phase extracted from slices at $z = 0$ cannot be digitally refocused as part of the post-detection image formation step since the phase does not obey the wave equation. This accounts for the distortion observed in the Rytov reconstruction (Figure 5.3) away from the plane of best focus.

The defocusing of the Rytov method can be avoided if we physically refocus the optical system multiple times and record the entire sequence of projections for each position. This allows us to reproduce the entire object by stitching together

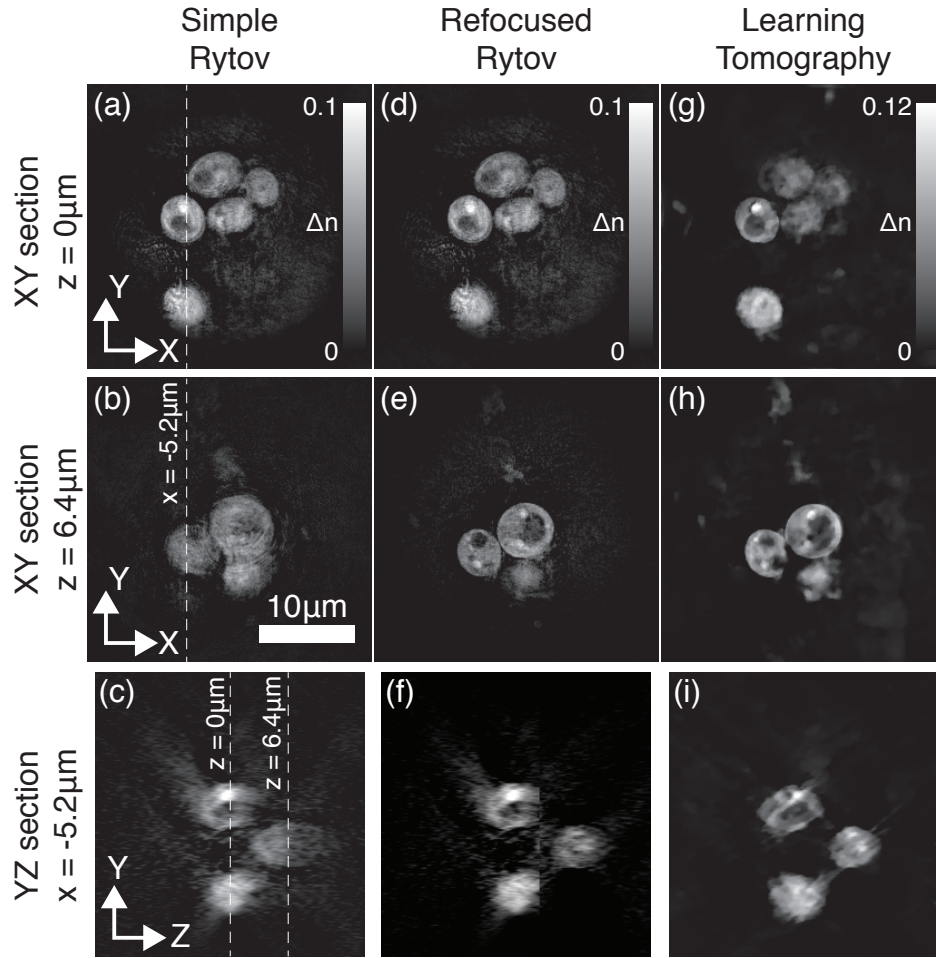


Figure 5.2: Reconstructions of a cell cluster using the Rytov approximation (a-c), the refocused version of Rytov (d-f), and the Learning Tomography method (g-i). The dashed lines in (a and b) indicates the trace of the $y-z$ sections shown in (c, f and i). The two dashed lines in (c) indicate the trace of the $x-y$ planes at two different depth in z , i.e. images (a, d and g) at $z = 0 \mu\text{m}$, and images (b, e and h) at $z = 6.4 \mu\text{m}$.

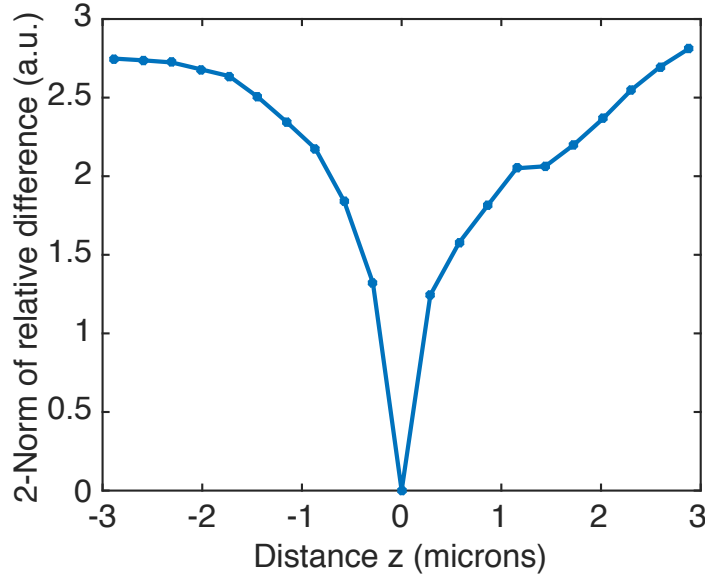


Figure 5.3: Error in the reconstruction using Rytov approximation as the distance with the imaging plane increases, for the sample shown in Figure 5.2. The quantity plotted is $\|R(z) - RR(z)\|^2 / \|RR(z)\|^2$, where $R(z)$ is the Rytov reconstruction (expressed as the refractive index contrast) in slice z (the imaging plane placed at $z = 0$) and $RR(z)$ the Rytov reconstruction refocused in plane z .

the reconstructions from different locations along z with an accompanying increase in the computational cost and the acquisition time of the data. Fortunately, it is not necessary to physically refocus the system since we have access to the complex field from the holographic recording. The refocusing can be done digitally as a post-detection step followed by a complete Rytov reconstruction for each focal position followed by stitching together of the reconstructions. The images shown in the second row of Figure 5.2 were obtained using this refocused Rytov method. We can obtain an empirical estimate for the depth of focus of the simple Rytov reconstruction by calculating the average squared difference between the simple and refocused Rytov reconstructions. The calculation in Figure 5.3 can be used to guide the selection of the number of positions in z that need to be selected for refocusing.

The third column in Figure 5.2 displays the images obtained with the LT method discussed in Chapter 3. Unlike the Rytov method, LT does not use the approximation that the detected signal is the result of a single scattering of the illuminating beam. With reference to Figure 5.3, each slice acts as a thin transparency modulating the light incident on it. The propagation from one slice to another is accounted for by a free space propagation step. Given the current estimate of the 3D complex index of the object, the BPM gives a prediction for the field incident on the detector. This prediction is then compared to the experimental

measurement and an optimization method similar to what is used in multi-layer neural networks gives the estimate for the 3D distribution of the complex index of refraction. The images obtained with LT do not have any defocusing since the propagation model accounts for the entire propagation through the sample.

The conclusions we draw from Figure 5.2 is that for samples consisting of two cells (optical path up to 10 radians and a thickness of 10 microns) refocused Rytov and LT give comparable image quality. For the thickness and complexity (index contrast) of the samples used in the experiments in Figure 5.2 the main difference between the results here and the single cell ODT experiments that have been reported extensively in the literature is the depth of focus limitations observed for the Rytov approximation and the solutions provided by refocused Rytov and LT.

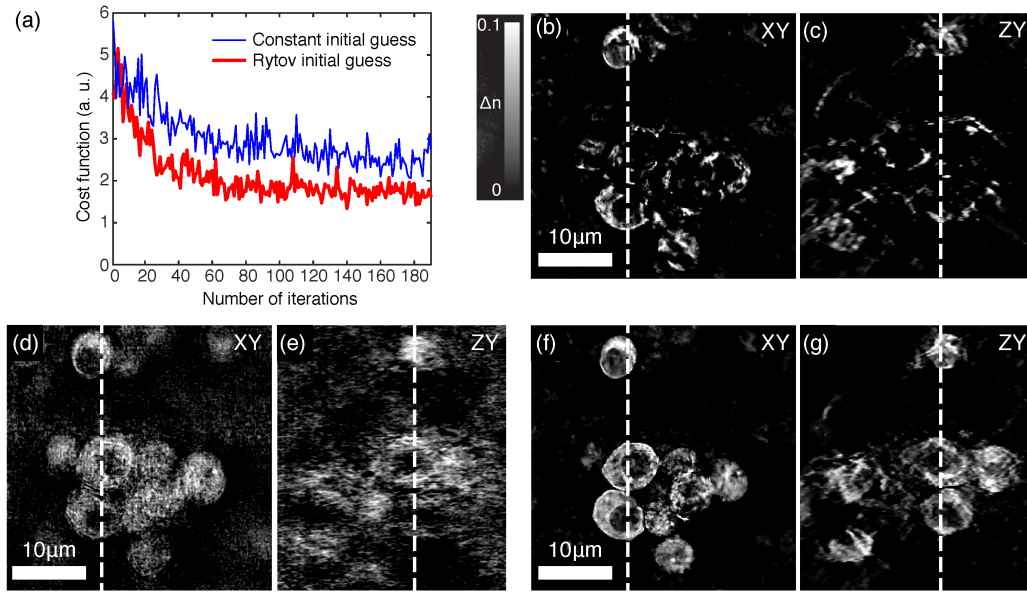


Figure 5.4: **Importance of initial guess.** (a) Cost function as a function of the number of iterations for the LT algorithm initialized with a constant refractive index contrast (thin blue curve) of $\Delta n = 0.03$, and the simple Rytov reconstruction (thick red curve). (b, c) $x - y$, $z - y$ slices through the LT reconstruction initialized with the constant initial guess. (d, e) The same slices through the Rytov reconstruction. (f, g) The same slices through the LT reconstruction initialized with the Rytov reconstruction shown in (d). All slices are at $z = 3.6$ microns from the experimental imaging plane. The vertical dashed lines in each image shows the intersection for the image beside it.

We have shown in a Chapter 4 that LT can be more accurate in imaging complex samples consisting of dielectric spheres and cylinders. Here we explore the sample complexity (thickness and index contrast) that LT can reach with objects consisting of cell clusters. The cluster of yeast cells in the experiment of Figure 5.4 consists of a maximum of 5 layers of cells and has a total thickness of approximately 30 μm . When LT is initialized with an initial guess of a constant refractive index, the algorithm reaches a local minima that is highly distorted. When the same cluster is reconstruction with LT but with the simple Rytov initial guess, the result

is a more complete and sharper image. Yeast cells are known to have vacuoles (compartments filled with water) and these are clearly visible in Figure 5.4(f) but not in Figure 5.4(b). Similarly, the y-z image of the LT reconstruction (Figure 5.4(g)) displays with high definition the cell structure along the depth of the sample. In general, as the sample complexity increases, the quality of the Rytov reconstruction gradually degrades, whereas for LT provided a good initial condition the image quality is conserved.

The Rytov approximation becomes distorted for slices in the z-direction more than $\pm 1\mu\text{m}$ away from the plane of best focus (see Figure 5.3). This can be overcome if we use refocused Rytov which compensates for this effect by digitally refocusing the system for multiple distances in z and stitching together the individual solutions to form a complete reconstruction.

The results shown in Figure 5.5 are images of the same sample as in Figure 5.4. The top row is the simple Rytov reconstruction clearly showing the limited depth of field of the technique. The second row shows the LT images obtained when initialized with the Rytov image of the top row and the third row shows the same slices of the cell cluster produced by the refocused Rytov method. In both cases a dramatic improvement in the clarity and contrast of the images is observed. The LT image (second row) has better contrast, sharpness and segmentation of the cells but artifacts due to the local minima are produced in some cases. Finally, the LT image obtained with the refocused Rytov as the initial condition is displayed in the bottom row. The image in the second row is quite similar to the image in the fourth row demonstrating that initialization of the LT algorithm with the simple Rytov is sufficient. Figure 5.5 (g) (the LT reconstruction with simple Rytov initialization) contains two cells (marked with arrows) that appear edge enhanced. Such artifacts are due to local minima in which the LT algorithm was trapped. This is made evident by observing Figure 5.5 (o) (the LT reconstruction with refocused Rytov as the initial condition). In this case, the proper contrast of one of the edge enhanced cells was restored because its z position happened to coincide with one of the Rytov refocused planes. Once initialized with the proper shape the algorithm stays there, indicating the presence of a strong minima.

5.4 Conclusion

We have experimentally explored the capabilities of the refocused Rytov and the LT algorithms in thick samples consisting of yeast cell clusters. The LT algorithm yields satisfactory results in term of sharpness and background noise both when starting from the single and refocused Rytov. LT has the capability of filling gaps in the initial guess over a range larger than the range of validity of the Rytov approximation (as shown in Figure 5.3). Moreover, even in planes in which the Rytov solution has been refocused, generally LT yields sharper images. We believe this is because multiple scattering is accounted for with LT. For objects that are thick, but weakly scattering, the Rytov solution can be quite close to the LT solution. How-

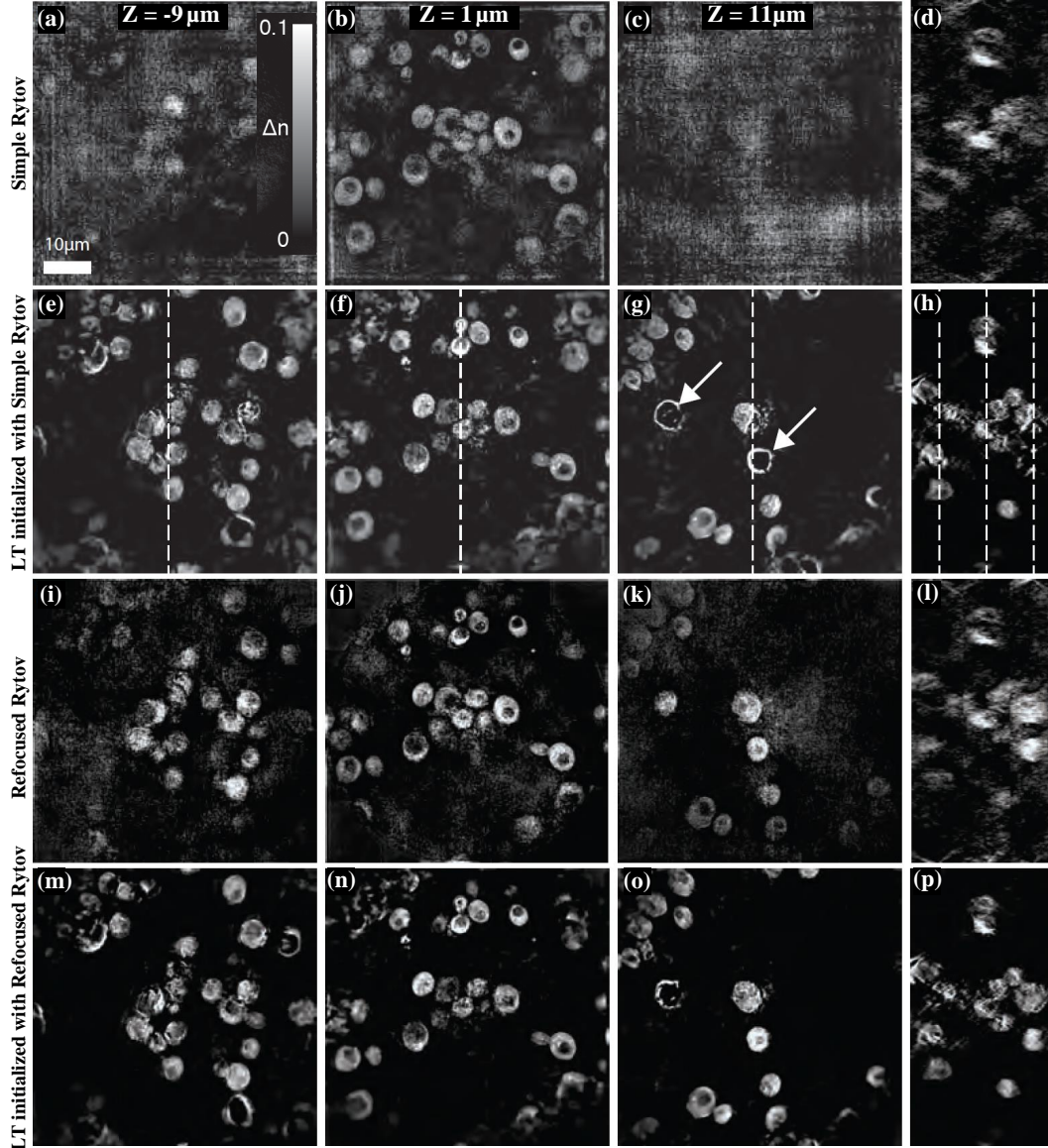


Figure 5.5: **Comparison for a 5 layer thick sample of the LT reconstructions starting from two different initial guesses.** (a-c) $x - y$ slices through the simple Rytov reconstruction at $z = -9, +1, +11$ microns, respectively (imaging plane at $z = 0$). (d) $z - y$ section through the simple Rytov reconstruction. (e-h) The same slices for the LT reconstruction initialized with the simple Rytov reconstruction. The vertical dashed lines showing the intersection of the $x - y$ section with the $z - y$ section. (i-l) The same sections through the stitched multi-domain refocused Rytov reconstruction, refocused in the displayed slices at $z = -9, +1, +11$ microns. (m-p) The same slices at the corresponding depths of the LT reconstruction initialized with the refocused Rytov reconstruction.

ever, for the Rytov reconstruction to be of comparable quality, the measurement needs to be refocused on at least one plane within the range of validity of the approximation, which is around 1 micron in this type of sample. In the case of the sample shown in Figure 5.5, we would thus need 30 refocused Rytov solutions. The phase unwrapping [21] that is part of each Rytov reconstruction generally dwarfs the computational cost of the optimization in the LT algorithm. Therefore, refocused Rytov is generally much more expensive in terms of computation time.

5.5 Bibliography

- [1] E. Wolf, "Three-dimensional structure determination of semi-transparent objects from holographic data," *Optics Communications*, vol. 1, no. 4, pp. 153–156, 1969.
- [2] V. Lauer, "New approach to optical diffraction tomography yielding a vector equation of diffraction tomography and a novel tomographic microscope," *Journal of Microscopy*, vol. 205, pp. 165–176, 2001.
- [3] F. Charrière, A. Marian, F. Montfort, J. Kuehn, T. Colomb, E. Cuhe, P. Marquet, and C. Depeursinge, "Cell refractive index tomography by digital holographic microscopy," *Optics Letters*, vol. 31, no. 2, pp. 178–180, 2006.
- [4] W. Choi, C. Fang-Yen, K. Badizadegan, S. Oh, N. Lue, R. R. Dasari, and M. S. Feld, "Tomographic phase microscopy," *Nature Methods*, vol. 4, pp. 717–719, 2007.
- [5] W. Choi, C. Fang-Yen, K. Badizadegan, R. R. Dasari, and M. S. Feld, "Tomographic phase microscopy," *Optics Letters*, vol. 33, no. 2, pp. 171–173, 2008.
- [6] Y. Sung, W. Choi, C. Fang-Yen, K. Badizadegan, R. R. Dasari, and M. S. Feld, "Optical diffraction tomography for high resolution live cell imaging," *Optics Express*, vol. 17, no. 1, pp. 266–277, 2009.
- [7] Y. Cotte, F. Toy, P. Jourdain, N. Pavillon, D. Boss, P. Magistretti, P. Marquet, and C. Depeursinge, "Marker-free phase nanoscopy," *Nature Photonics*, vol. 7, no. 2, pp. 113–117, 2013.
- [8] F. Merola, P. Memmolo, L. Miccio, R. Savoia, M. Mugnano, A. Fontana, G. D'Ippolito, A. Sardo, A. Iolascon, A. Gambale, and P. Ferraro, "Tomographic flow cytometry by digital holography," *Light: Science & Applications*, vol. 6, p. e16241, 2017.
- [9] K. Lee, K. Kim, J. Jung, J. Heo, S. Cho, S. Lee, G. Chang, Y. Jo, H. Park, and Y. Park, "Quantitative phase imaging techniques for the study of cell pathophysiology: From principles to applications," *Sensors*, vol. 13, no. 4, pp. 4170–4191, 2013.

- [10] A. J. Devaney, "Inverse-scattering theory within the rytov approximation," *Optics Letters*, vol. 6, no. 8, pp. 374–376, 1981.
- [11] P. Muller, M. Scharmann, and J. Guck, "The theory of diffraction tomography," *arXiv:1507.00466v3*, 2016.
- [12] J. Radon, "Über die bestimmung von funktionen durch ihre integralwerte langs gewisser mannigfaltigkeiten," *Berichte der Sachsischen Akademie der Wissenschaft*, vol. 69, pp. 262–277, 1917.
- [13] A. J. Devaney, *Mathematical Foundations of Imaging and Tomography and Wave-field Inversion*, Cambridge Univ. Press, 2012.
- [14] N. Sponheim, I. Johansen, and A. J. Devaney, "Initial testing of a clinical ultrasound mammograph," *Acoustical Imaging*, vol. 18, pp. 401–411, 1991.
- [15] J. Kostencka, T. Kozacki, A. Kus, B. Kemper, and M. Kujawinska, "Holographic tomography with scanning of illumination: space-domain reconstruction for spatially invariant accuracy," *Optics Express*, vol. 7, no. 10, pp. 4086–4101, 2016.
- [16] W. Choi, C. Fang-Yen, K. Badizadegan, R. R. Dasari, and M. S. Feld, "Extended depth of focus in tomographic phase microscopy using a propagation algorithm," *Optics Letters*, vol. 33, no. 2, pp. 171–173, 2008.
- [17] U. S. Kamilov, I. N. Papadopoulos, M. H. Shoreh, A. Goy, C. Vonesch, M. Unser, and D. Psaltis, "Learning approach to optical tomography," *Optica*, vol. 2, no. 6, pp. 517–522, 2015.
- [18] U. S. Kamilov, I. N. Papadopoulos, M. H. Shoreh, A. Goy, C. Vonesch, M. Unser, and D. Psaltis, "Optical tomographic image reconstruction based on beam propagation and sparse regularization," *IEEE Transactions on Computational Imaging*, vol. 2, no. 1, pp. 59–70, 2016.
- [19] L. Tian and L. Waller, "3d intensity and phase imaging from light field measurements in an led array microscope," *Optica*, vol. 2, no. 2, pp. 104–111, 2015.
- [20] J. Lim, A. Goy, M. H. Shoreh, M. Unser, and D. Psaltis, "Assessment of learning tomography using Mie theory," *arXiv:1705.10410*, 2017.
- [21] J. M. Bioucas-Dias and G. Valadão, "Phase unwrapping via graph cuts," *IEEE Transactions on Image Processing*, vol. 16, no. 3, pp. 698–709, 2007.

Initialization, Local Minima and Phase Unwrapping

Contents

6.1 Initialization and local minima	63
6.2 Phase unwrapping	67
6.3 Conclusion	70
6.4 Bibliography	70

Since the energy function in LT is generally non-convex, the solution it obtains is not guaranteed to be globally optimal. In this section, we investigate the influence of the initialization on the convergence of the algorithm. In particular, we show that proper initialization is essential for high-quality imaging in strongly scattering scenarios. We present the landscape of the cost function between the estimated and true solutions showing the local minima problem for two different accumulated phase scenarios with and without regularization. We provide experimental results for different initialization and show their convergences. At the end, we look into the phase unwrapping problem and compare different phase unwrapping methods for our experimental data.

6.1 Initialization and local minima

In this section, we examine the importance of the initial guess used to initiate the optimization. We illustrate the problem of local minima and show how we can avoid local minima by initiating using DT, as well. The LT algorithm has to find the point in the multi-dimensional space that minimizes the cost function. As in most nonlinear optimization problems, the solution is surrounded by many local minima. In this optimization problem, we observe empirically that the local minima are locally convex regions and that the gradient of the error function vanishes in them. Therefore, once the gradient descent algorithm fall into a local minima, cannot get out of it. However, the shape of the cost function that includes the regularizer is much smoother.

We carried out scattering simulation on a homogeneous 15-micron sphere embedded in a homogeneous material of refractive index $n_0 = 1.5$ refractive index background, illuminated at a wavelength of 532nm. We study two cases by tuning the refractive index of the object: in the first case, shown in the Figure 6.1 (a, c),

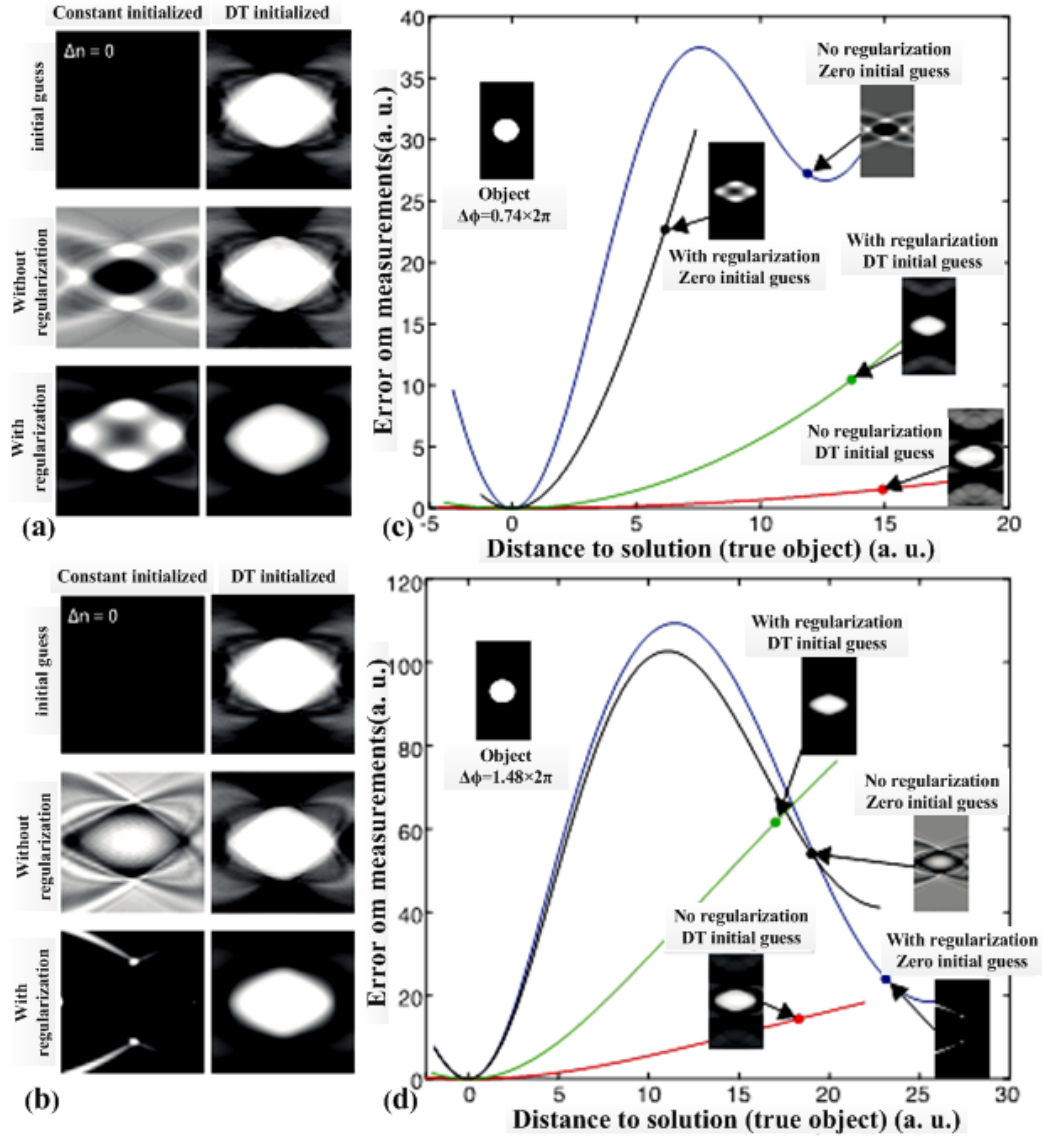


Figure 6.1: Illustrating the importance of the initial guess on the performance of the LT algorithm. All images are $y - z$ cross sections. The gray scale on each figure is the same and linear from black ($n = 1.5$) to white ($n = 1.55$). (a) The object has a refractive index contrast of $\delta n = 0.026$, which leads to a total phase shift of $0.76 \times 2\pi$. The top row shows the initial guesses, constant zero on the left and DT with Rytov approximation on the right. The second row shows the outcome of LT with no regularization (20 iterations). The third shows the outcome of LT with TV regularization at each step. (b) Same simulations as in (a) but with an object contrast of $\delta n = 0.052$, which leads to a total phase shift of $1.48 \times 2\pi$. (c, d) Cross sections through the measurement cost function for different initial conditions, with and without regularization, for the low contrast object of $0.76 \times 2\pi$ phase shift (c), and the high contrast object of $1.48 \times 2\pi$ (d). The horizontal axis is the distance to the solution expressed as the norm of the difference between the current digital model estimate and the true object. The position of the model estimates after 20 iterations of the LT algorithm is shown by the arrows. The cross sections displayed correspond to the landscape along linear interpolated positions in the configuration space between the model estimate and the true object.

the total optical phase shift induced by the object is less than a period (2π). In the second case, shown in Figure 6.1(b, d), the phase shift is larger than 2π . The linear algorithm used to produce the initial guess, in Figure 6.1 (a, b) is diffraction tomography under the Rytov approximation. This reconstruction suffers from severe artifacts that are suppressed by the regularized LT optimization. The result of the simulation as whether LT can approach the best solution, strongly depends on the total phase shift. For weak phase shifts, the algorithm can converge with the help of regularization and proper initialization. For larger phase shifts, the algorithm fails to converge even with regularization and hard constraint on the upper and lower bounds of the refractive index. We interpret this phenomenon as the expression of the phase wrapping. Phase wrapping (investigated in Section 6.2) induces an ambiguity in the measurements that correspond to deep local minima in the cost function. The depth of local minima can be estimated by looking at the landscape of the cost function between the estimated and true solutions. A natural way is to proceed in the configuration space along a straight line from the current model estimate toward the true solution, i.e. by performing a linear interpolation between the estimated and true solutions and calculate the cost function at each position in-between. In Figure 6.1(c) and (d), we show such cross sections in the cost function for the two objects of different contrast shown in Figure 6.1 (a) and (b), respectively. The starting point for each section (shown by an arrow in Figure 6.1 (c, d)) is the endpoint of the LT algorithm after 20 iterations for different initial guesses, with and without regularization. From these plots, we can draw the following qualitative conclusions:

- initialization using diffraction tomography reduces the measurement cost but may suffer from artifact due to the missing cone effect. In Figure 6.1 (c), after 20 iterations of LT, the model estimate is closer to the solution when regularization is used together with a constant initial guess than when the Rytov reconstruction is used as an initial guess. In fact, the cost function is much reduced when the Rytov initial guess is used, but then, it is likely that the LT algorithm converges more slowly after initialization using DT containing artifact.
- For Figure 6.1 (c), it is clear that regularization modifies the landscape of the cost function. With no regularization and a constant initial guess, the LT gets trapped in a local minima. This minima corresponds to a contrast inversion in the model estimate, which in fact is a manifestation of phase wrapping.
- Increasing the contrast of the object above 2π of total phase shift also has a dramatic effect on the cost function landscape. When using a constant zero initial guess, the LT falls in relatively much deeper local minima and regularization is not able to steer it out.

In Figure 6.2, we show reconstruction obtained with the LT algorithm from experimental measurements on a 5 micron polystyrene bead immersed in oil. We

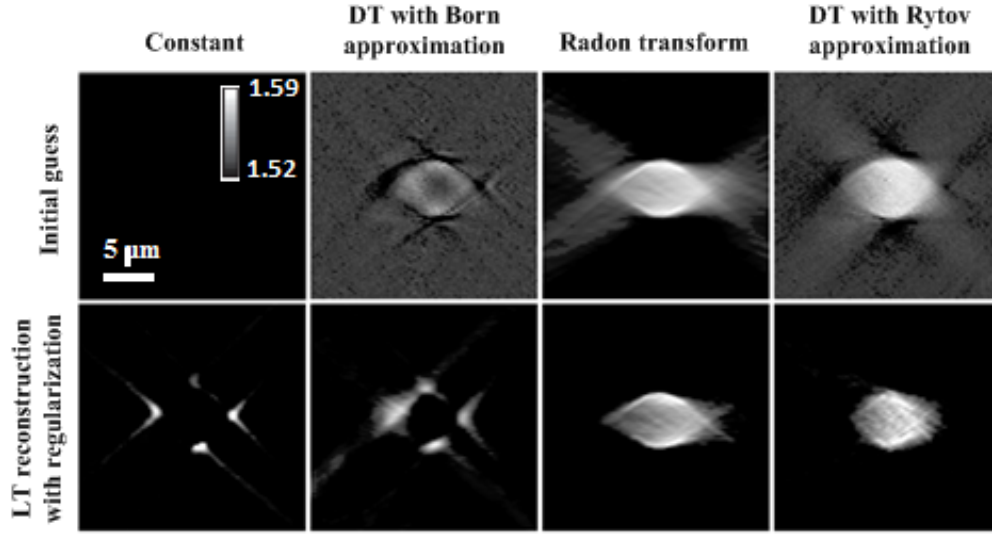


Figure 6.2: Experimental reconstruction of a 5 micron polystyrene bead obtained with the LT algorithm (second row) from four different initial guesses (first row, left to right): constant ($n_0 = 1.52$), Born [2], Radon [1], and Rytov [3].

show the reconstructions for four different initial guesses: constant refractive index, Radon transform [1], and diffraction tomography with Born [2] and Rytov [3] approximation. The experimental results essentially corroborate the simulations in the case of constant and Rytov approximation initial guesses. The total phase delay across the beads is above 2π , and the measurements have been unwrapped accordingly. Our simulation and experimental results also indicate that TV regularization together with a good initial guess are essential for obtaining the best possible LT reconstruction. In particular, for a weakly scattering object Figure 6.1 (a), LT with TV is able to reconstruct the bead even from zero initialization. The quality of the reconstruction is further improved by using the diffraction tomography initialization. On the other hand, for strongly scattering scenarios Figure 6.1 (b), TV regularization without DT initialization yields poor results. This highlights the fact that TV must be supplemented with a good initializer for obtaining the best results in strongly scattering scenarios.

To compare the performance with the leading methods, the result of different tomographic reconstructions methods is used to initialize the learning algorithm. Figure 6.3 presents the results, showing that diffraction tomography [3] and iterative Radon [4] initiation reduced the error compared to Radon reconstructions. It also illustrate that the learning algorithm reduces the error further in all cases which results in improving the quality of the reconstructed image. It is noteworthy to mention that all four runs corresponding to different initial conditions converge to the same final reconstruction after 100 iterations.

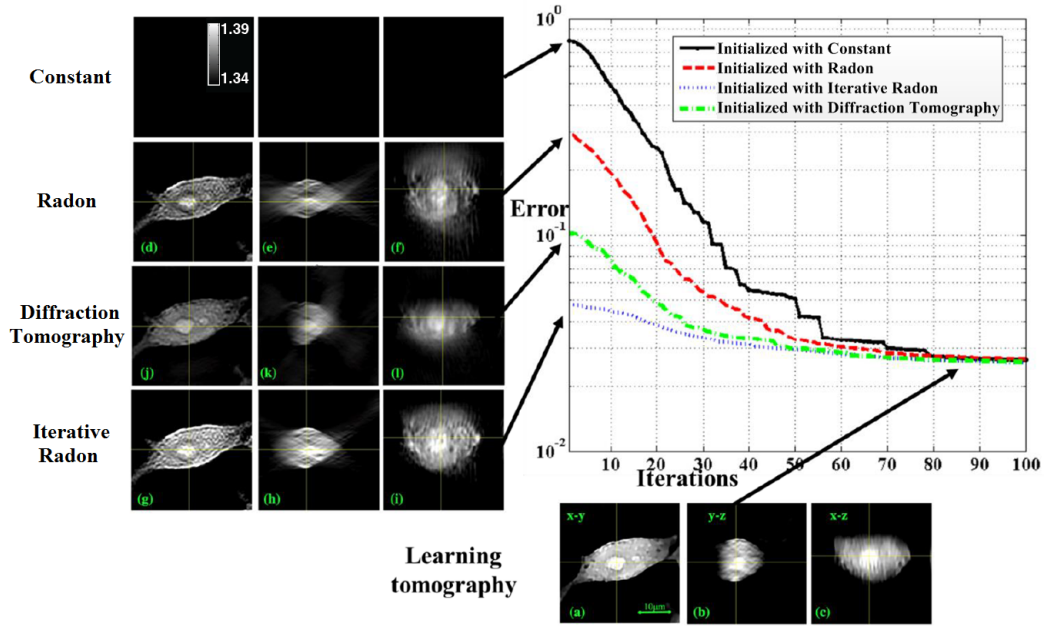


Figure 6.3: Error between the experimental measurement and the predictions of the computational model versus the number of iterations in four different initiation scenarios: constant value (black), the Radon reconstruction [1] (red), the diffraction tomography [3] (green), and the iterative Radon [4] (blue).

6.2 Phase unwrapping

Two-dimensional phase unwrapping is an essential component in a majority of techniques used for quantitative phase imaging. In tomographic phase microscopy, for near-plane wave illumination of a sample, the phase of the transmitted field can be well approximated as the integral of the refractive index along the path of beam propagation. However, for this approximation to hold, the phases extracted from the transmitted fields must be first unwrapped, which significantly limits the applications of the technique for imaging objects that are out of focus, large, or have high refractive index contrast. Once unwrapped, the phase image can simply be interpreted as the projection of refractive index, analogous to the projection of absorption in x-ray tomography.

To better illustrate this in Figure 6.4 two scenarios are proposed. The first one is a 6 micron polystyrene bead with refractive index contrast of 0.01 which leads to 0.44π accumulated phase. It is obvious that in the unwrapped phase there is no sign of singularity or imperfection (Figure 6.4 (a)). In this case, we announce the phase unwrapping procedure has passed. In the second scenario, a bead with the same size has refractive index contrast of 0.15 which will create 6.74π accumulated phase (Figure 6.4 (b)). In this case, the unwrapped phase has singularity or imperfection, hence, we announce the phase unwrapping has failed to unwrap the phase correctly. Figure 6.4 (c) presents simulation of phase unwrapping procedure (pass

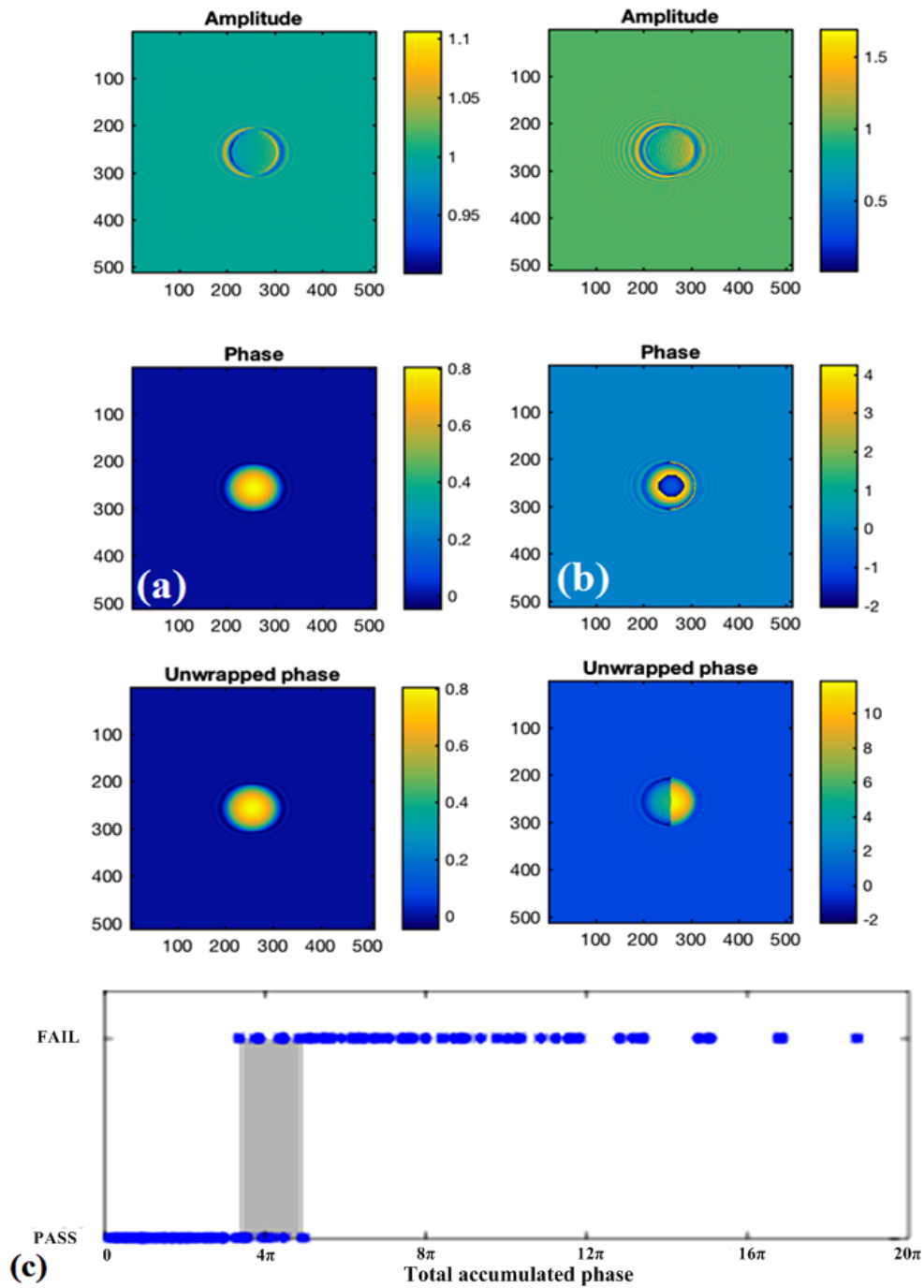


Figure 6.4: A 6 micron polystyrene bead with refractive index contrast of: (a) 0.01 which leads to 0.44π accumulated phase, (b) 0.15 which will create 6.74π accumulated phase. (c) Simulation of phase unwrapping procedure (pass or fail) for different accumulated phases showing 4π (the darker region) as the transition region from always pass to always fail.

or fail) for different accumulated phases. Obviously around 4π (the darker region in Figure 6.4 (c)) the phase unwrapping can fail or pass. For accumulated phase below this region the procedure is always passing and above this region is always failing. Considering this we can announce 4π as the maximum unwrap able phase for this algorithm. We used the widely spread Goldstein [5] phase unwrapping for this simulation.

To evaluate and choose the best phase unwrapping algorithms, we measured the refractive index tomograms of six polystyrene spheres (catalog no. 17135, Polysciences, refractive index $n=1.602$ at 561 nm) immersed in oil with a lower refractive index of 1.516. The wrapped phase image of size 512×512 is extracted from the transmitted field at angle 39° with respect to vertical axis. This phase data are difficult to unwrap because of numerous visible phase discontinuities that appear along the borders of the beads.

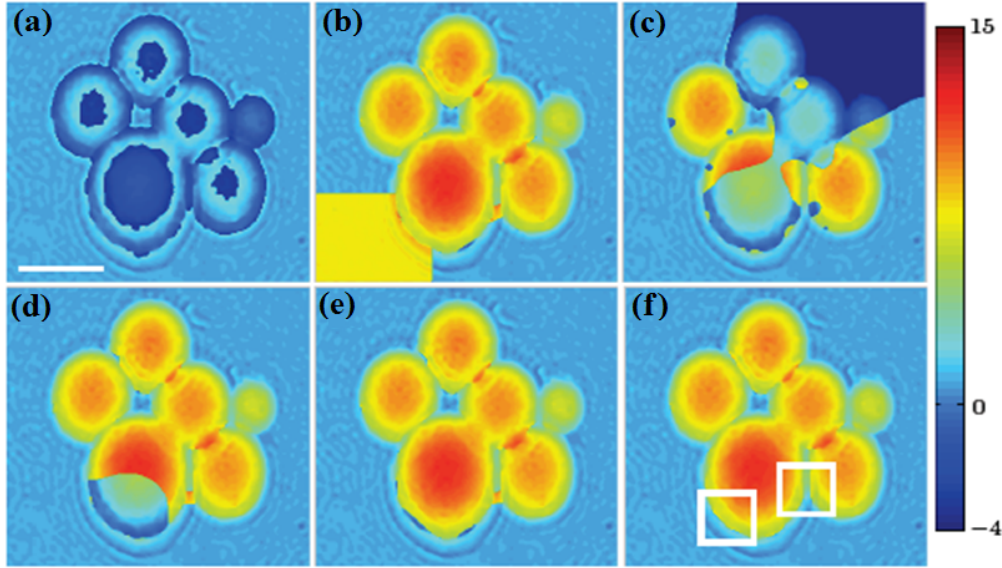


Figure 6.5: Phase unwrapping results for Beads image of size 512×512 obtained from the phase of the transmitted field. (a) wrapped phase, (b) Goldstein's Algorithm (GA) [5], (c) Least-Squares (LS) [6], (d) Iteratively Reweighted LS (IRLS) [7], (e) PUMA [8]; and (f) IRTV [9]. Scale bar, $5\mu\text{m}$.

Figure 6.5 illustrates the results of four standard unwrapping methods such as Goldstein's Algorithm (GA) [5], Least-Squares (LS) [6], Iteratively Reweighted LS (IRLS) with data-dependent weights that approximate the $l_0 - \text{norm}$ penalty [7] and PUMA [8]. Additionally the performance of a method coauthored by me [9] is presented in Figure 6.5 (f). As expected, all algorithms perform equally well in the continuous region of the image. On the other hand, our approach is the only one that accurately captures the discontinuous region of the unwrapped image. This is expected because of rotation invariance of our energy functional [9]. Additionally, we note that the LS method, which is also based on rotation invariant energy functional, fails to preserve the edge because of excessive smoothing.

The parameters of our IRTV method were chosen as in the synthetic experiments above with the exception of the regularization parameter that was set to $\tau = 0.1$ [9]. The results in Figure 6.5 illustrate the effectiveness of our method in unwrapping the phase, even in the most difficult regions of the image that contain strong phase discontinuities. Specifically, our method is the only one that was able to accurately unwrap the region between the two beads at the bottom of the image (see highlights in the Figure 6.5).

6.3 Conclusion

We went over the local minima problem and discussed ways to get out of them. The influence of the initialization on the convergence of the algorithm was investigated and its essentiality was shown for high-quality imaging in strongly scattering scenarios. We present the error landscape showing the local minima problem for two different accumulated phase scenarios with and without regularization. We provide experimental results for different initializations and show their convergences. At the end, we look into phase unwrapping problem and compare different phase unwrapping methods for our experimental data.

6.4 Bibliography

- [1] R. M. Lewitt, "Reconstruction algorithms: transform methods." *Proceedings of the IEEE*, vol. 71, no. 3 (1983): 390-408.
- [2] E. Wolf, "Three-dimensional structure determination of semi-transparent objects from holographic data," *Optics Communications* 1, no. 4 (1969): 153-156.
- [3] K. Kim, H. Yoon, M. Diez-Silva, M. Dao, R. R. Dasari, and Y. Park, "High-resolution three-dimensional imaging of red blood cells parasitized by *Plasmodium falciparum* and in situ hemozoin crystals using optical diffraction tomography," *J. Biomed. Opt.*, vol. 19, p. 011005, 2014
- [4] Y. Sung, W. Choi, N. Lue, R. R. Dasari, and Z. Yaqoob, "Stain-free quantification of chromosomes in live cells using regularized tomographic phase microscopy," *Plos One* 7(11), e49502 (2012).
- [5] R. M. Goldstein, H. A. Zebker, and C. L. Werner, "Satellite radar interferometry: two-dimensional phase unwrapping," *Radio Sci.* 23, 713-720 (1988).
- [6] D. C. Ghiglia and L. A. Romero, "Robust two-dimensional weighted and unweighted phase unwrapping that uses fast transforms and iterative methods," *J. Opt. Soc. Am.* 11, 107-117 (1994).
- [7] D. C. Ghiglia and L. A. Romero, "Minimum Lp-norm two-dimensional phase unwrapping," *J. Opt. Soc. Am. A* 13, 1999-2013 (1996).

-
- [8] J. M. Bioucas-Dias and G. Valadão, "Phase unwrapping via graph cuts," *IEEE Trans. Image Process.* 16, 698-709 (2007).
 - [9] U. S. Kamilov, I. N. Papadopoulos, M. H. Shoreh, D. Psaltis, and M. Unser, "Isotropic inverse-problem approach for two-dimensional phase unwrapping," *JOSA A* 32, no. 6 (2015): 1092-1100.

Multiple Scattering

Contents

7.1 Introduction	73
7.2 Results	74
7.3 Conclusion	78
7.4 Bibliography	78

In almost all microscopy techniques, including wide field and confocal imaging single scattering is assumed. This imposes strong limitations on the resolution that can be achieved, especially, in biological tissues that are highly scattering. Our proposed learning-based algorithm for optical tomography takes multiple scattering into account. In this chapter, we experimentally demonstrate that LT can handle multiple scattering and show cases where linear methods such as DT fail. We experimentally compare the reconstruction of the two beads stacked in z with the superposition of the individual beads added together which shows there is a significant left over due to multiple scattering for DT, whereas in the case of LT, the superposition of the individual reconstructions overlaps almost perfectly with the reconstruction of the two beads together.

7.1 Introduction

Optical inverse scattering has recently received great attention from the scientific community. One of the natural avenues to further improve optical microscopy is to account for multiple scattering. This is of particular importance in biological tissues because of the rise of biological applications and the fact that biological tissues can be strongly scattering. Moreover, the study of dynamical process requires minimally invasive in vivo imaging techniques. Optical tomography [1] has the advantage of being non-toxic and to allow for three-dimensional imaging. One of the criticisms is that tomography only helps in building a map of the refractive index of the sample and does not really allow for the tracking of dynamic processes as fluorescence does. However, the characterization of the spatial scattering properties of the sample is of crucial importance to all other microscopy methods, including fluorescence microscopy [2] that will take advantage of wavefront correction techniques [3].

Mapping the refractive index of a sample is now conventionally performed using optical DT [4]. The initial studies [5] were based on the first Born approxima-

tion that accounted for single scattering only, which implies a linear relationship between the scattering potential and the scattered field. Such a method is limited to weakly scattering objects though. Improvement in reconstruction accuracy was then brought by the Rytov approximation [6]. Both the Rytov and the first Born approximations provide direct formulas to solve the inverse scattering problem, i.e., the problem of going from the measurements of the scattered field to a model of the refractive index distribution within the sample. For multiple scattering, the problem becomes nonlinear and there is no known closed-form formula. The natural way of performing inverse scattering is through optimization techniques. Such techniques have been thoroughly investigated in many area of science [7].

In this chapter, first, the simulation of two cells stuck in z is investigated and it is shown that LT severely outperforms DT. Then comparison of DT versus LT in the term of the difference between the reconstruction of two cells stuck in z and the superposition of individual reconstructions of the same cells is presented. Comparison of DT versus LT in the reconstruction of three cells stuck in z for maximum accumulated phase of 3π and 1.5π is shown. Finally experimentally achieved performance comparison of the reconstruction of two beads stuck in z with the superposition of individual reconstructions of the same beads and the difference between these reconstructions for both method are presented.

7.2 Results

Comparison of the DT versus the LT in the reconstruction of the simulation of two cells stuck in z is presented in Figure 7.1. Since the Rytov approximation is not valid for this sample due to multiple scattering, the DT method is not capable of reconstructing the object accurately while the LT correctly reconstructs the object showing the capability of this method in dealing with multiple scattering. In Figure 7.1, we emphasize the same point by comparing the DT reconstruction of the simulation of two cells stuck in z with the LT reconstruction. The DT tries to fill the area between the two cells, however, the LT easily distinguishes the cells to two individual object separated with a specific distance.

Figure 7.2 compares the DT versus the LT in term of the difference between the reconstruction of two cells stuck in z and the superposition of individual reconstructions of the same cells. This is aimed to show that the DT is not taking into account the effect of multiple scattering. Hence, there is a significant difference between the reconstruction of two cells at the same time and the superposition of individual reconstructions of the same cells which shows the multiple scattering effects.

In Figure 7.3, we try to compare the DT versus the LT for three cells stuck in different z . Since the DT does not take into account multiple scattering, the DT reconstruction of this three cells is not promising and as the refractive index is increased twice, the DT completely fails while the LT can catch up using tricks like adding a DC initial guess and sparsity. When we go beyond 2π phase accumula-

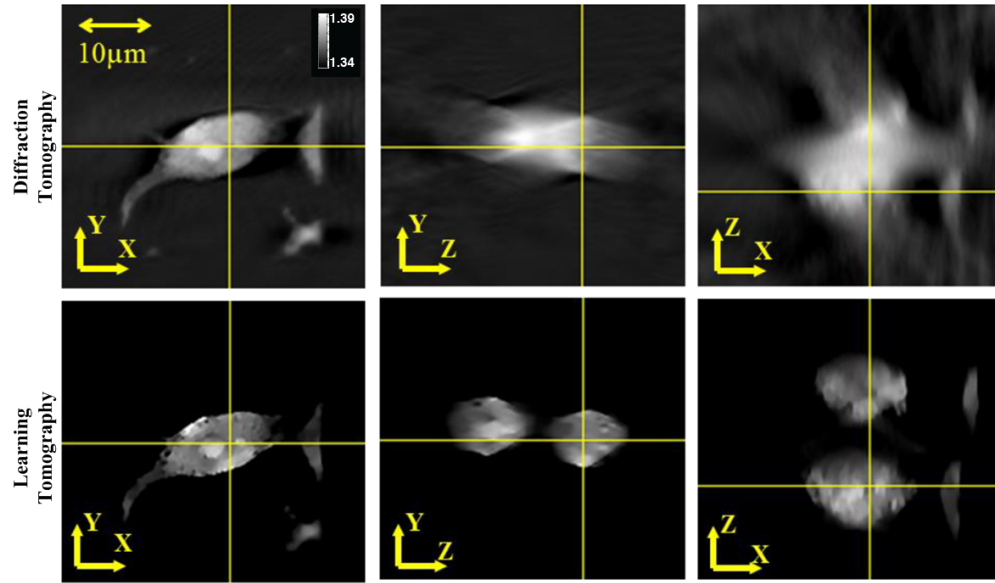


Figure 7.1: Comparison of the DT versus the LT in the reconstruction of the simulation of two cells stuck in z.

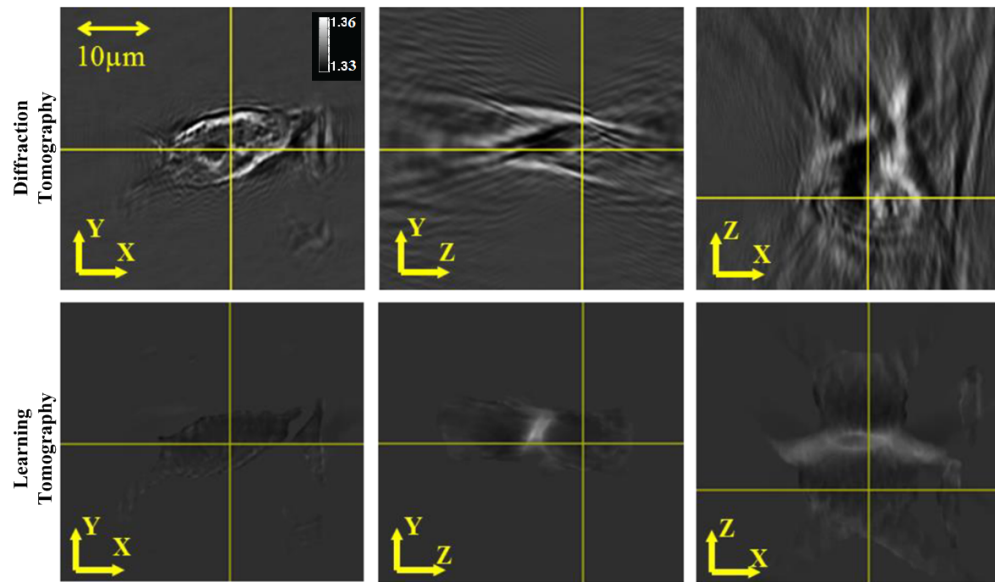


Figure 7.2: Comparison of the DT versus the LT in the term of the difference between the reconstruction of two cells stuck in z and the superposition of individual reconstructions of the same cells showing the multiple scattering effects.

tion, initiating with the radon or the DT will help. The first row of the Figure 7.3 shows the LT reconstruction on x-y, z-y and x-z for the maximum accumulated phase of 3π . The second row shows the DT reconstruction for the maximum accumulated phase of 1.5π and the third row shows the DT reconstruction when the maximum accumulated phase is 3π .

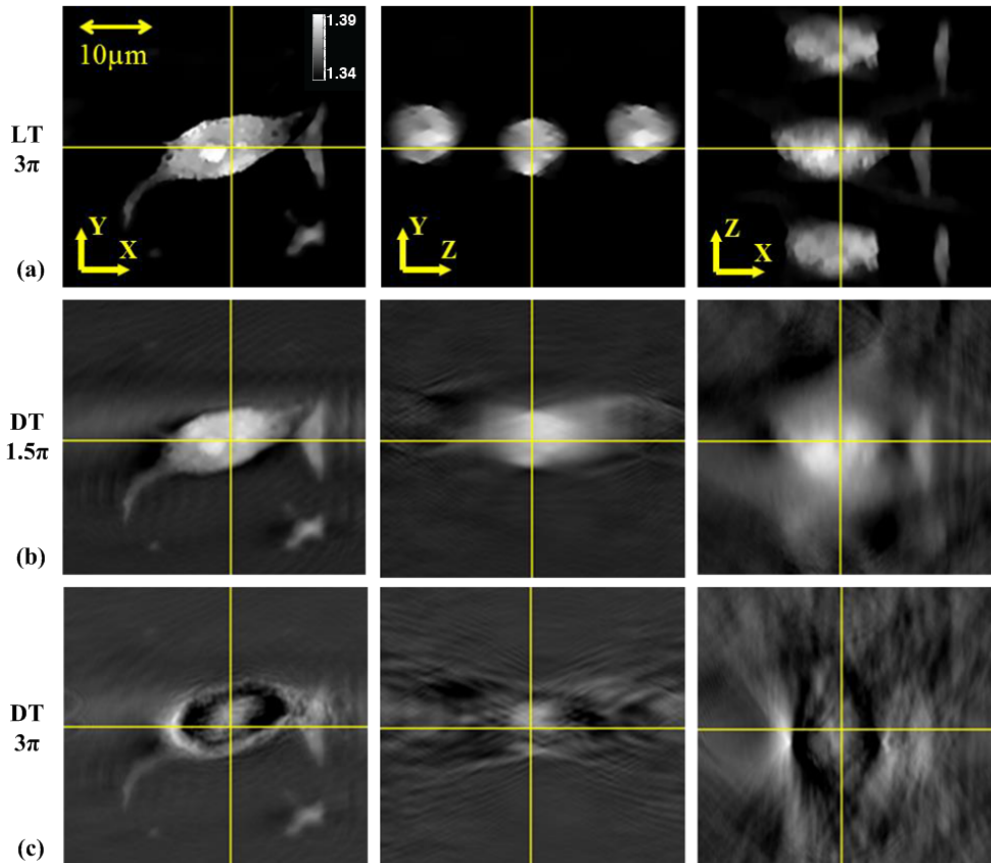


Figure 7.3: Comparison of the DT versus the LT in the reconstruction of three cells stuck in z (a) LT reconstruction for maximum accumulated phase of 3π . The DT reconstruction for maximum accumulated phase of (b) 1.5π and (c) 3π

The same concept presented in Figure 7.2, is experimentally validated with two 5 micron polystyrene spherical beads in Figure 7.4. The DT reconstruction (Figure 7.4 (a)) is compared to the LT reconstruction (Figure 7.4 (b)). In the first row, the reconstruction of the two beads stacked in z is presented. Second row presents the linear superposition of individual reconstructions of each bead. The third row shows the difference between the first and the second rows. For the DT, there is a significant left over for the difference which is due to multiple scattering, whereas in the case of the LT, apart from a slight misalignment, the superposition of the individual reconstructions overlap well with the reconstruction of the two beads together.

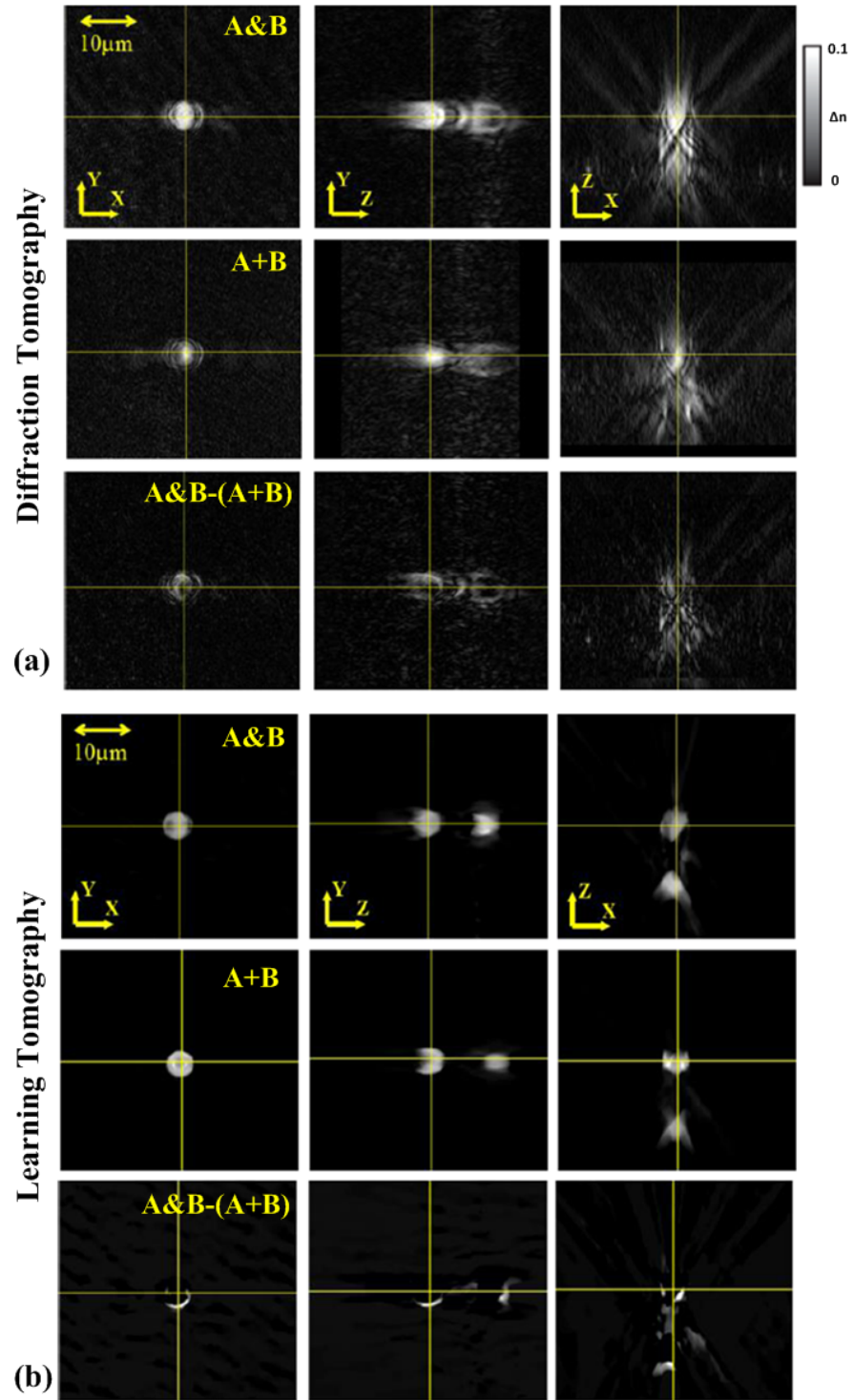


Figure 7.4: (a) DT versus (b) LT performance comparison of the reconstruction of two beads stuck in z (first rows), the superposition of individual reconstructions of the same beads (second row) and the difference between these two (third row).

7.3 Conclusion

It was experimentally presented that due to overcoming multiple scattering, the LT reconstruction greatly outperform the DT reconstruction when the sample contain two or more layers of cells or beads. We compare the reconstruction of the two beads (and cells) stacked in z with the superposition of the individual ones added together which shows there is a significant left over due to multiple scattering for the DT, whereas in the case of the LT, the residual is negligible.

7.4 Bibliography

- [1] Arridge, Simon R., "Optical tomography in medical imaging," *Inverse problems* 15, no. 2 (1999): R41.
- [2] Agard, David A., et al. "Fluorescence microscopy in three dimensions," *Methods in cell biology* 30 (1989): 353-377.
- [3] Jesacher, A., A. Schwaighofer, S. Frhapter, C. Maurer, S. Bernet, and M. Ritsch-Marte, "Wavefront correction of spatial light modulators using an optical vortex image," *Optics express* 15, no. 9 (2007): 5801-5808.
- [4] Sung, Yongjin, Wonshik Choi, Christopher Fang-Yen, Kamran Badizadegan, Ramachandra R. Dasari, and Michael S. Feld. "Optical diffraction tomography for high resolution live cell imaging," *Optics express* 17, no. 1 (2009): 266-277.
- [5] E. Wolf, "Three-dimensional structure determination of semi-transparent objects from holographic data," *Opt. Commun.* 1, 153-156 (1969).
- [6] Devaney, A. J. "Inverse-scattering theory within the Rytov approximation," *Optics letters* 6, no. 8 (1981): 374-376.
- [7] Ablowitz, Mark J., David J. Kaup, and Alan C. Newell. "The Inverse Scattering Transform Fourier Analysis for Nonlinear Problems," *Studies in Applied Mathematics* 53, no. 4 (1974): 249-315.
- [8] K. Kim, H. Yoon, M. Diez-Silva, M. Dao, R. R. Dasari, and Y. Park, "High-resolution three-dimensional imaging of red blood cells parasitized by *Plasmodium falciparum* and in situ hemozoin crystals using optical diffraction tomography," *J. Biomed. Opt.*, vol. 19, p. 011005, 2014

Other Results and Comparisons

Contents

8.1 Intensity measurments	79
8.2 3D movie reconstruction	80
8.3 Comparison with existing imaging techniques	82
8.4 Comparing with commercially available imaging techniques	85
8.5 Comparison of computation costs	87
8.6 Conclusion	89
8.7 Bibliography	89

In this chapter, first the LT technique based on intensity measurements is investigated on a previously presented HeLa cell. We also look into the procedure of a live MCF7 cells blebbing during apoptosis to illustrate the proposed method can be used for analyzing cell behavior in vivo-like systems. Then, some final comparisons with the existing techniques such as Born, Rytov, Refocused Rytov as well as the commercially available techniques such as florescent, reflection and transmission confocal is presented. At the end, the complexity and cost of the proposed LT method are investigated and compared with other existing methods.

8.1 Intensity measurments

In this section, the LT technique based on intensity measurements is investigated on HeLa cells. The use of intensity measurement for optical diffraction tomography reconstruction has been previously investigated [1–3]. In the intensity based LT, there is no need to measure the complex field so there is no need to have a reference beam. Therefor the reference beam is removed from the setup and measurements of the field intensity are conducted. In intensity measurement, incoherent light can be used, whereas, a laser is used here causing some speckle. The cells imaged here are primarily phase objects and therefore we expect knowing the complex field to be an advantage. To illustrate this, we carried out an experiment where we reconstruct the same HeLa cell as the one presented in Figure 3.5; except we use intensity detection rather than holographic recording. The intensity only reconstruction with the learning algorithm after 100 iterations with a constant initial guess is shown in Figure 8.1 (a). Figure 8.1 (b) presents the complex field measurement reconstruction, suggesting that for cells, coherent detection coupled with

the TV constraints yields better results. However, this is only a very preliminary result and further studies are needed to make a fair comparison. Since this work deals with measurement of the intensity, it would be interesting to know if the reconstruction with the complete field information, but without phase unwrapping has similar behavior as the reconstruction with only intensity. Clearly the preferable method will depend on the conditions of the imaging and its application.

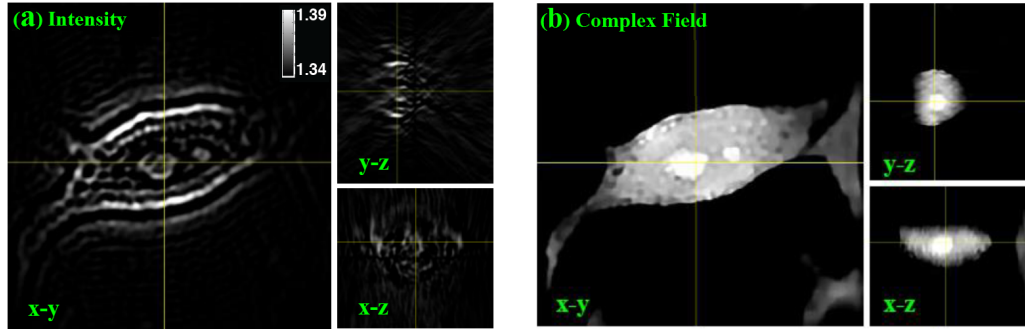


Figure 8.1: (a) Intensity only LT reconstruction after 100 iterations. (b) LT Reconstruction using the complex field measurement.

8.2 3D movie reconstruction

The proposed method is phase contrast and do not use any kind of staining, hence, it can be applied to the following situations

- Analyzing cell behavior in vivo-like systems
- Observing and measuring the effect of drugs in real-time
- studying cancer cells and immuno-oncology

3D movies of live cells can be used to monitor every second of the cell's life such as (1) division (2) death (3) nanoparticles internalization and localization inside cells (4) interaction among cells (cell-cell and host-pathogen) and measuring their reactions (5) the secrets of the smallest living organism like Bacteria, Yeast, Protozoa and Diatoms and studying their morphology and dynamics.

Figure 8.2 shows a 3D movie of refractive index reconstruction of an MCF7 cell during apoptosis. Each sub-figure shows the same cell after 500 seconds. The total time slap is around one hour. One is able to see that the bubbles surrounding the cell is growing during time. This is known as Blebbing in Biology and is a famous way of death in cells.

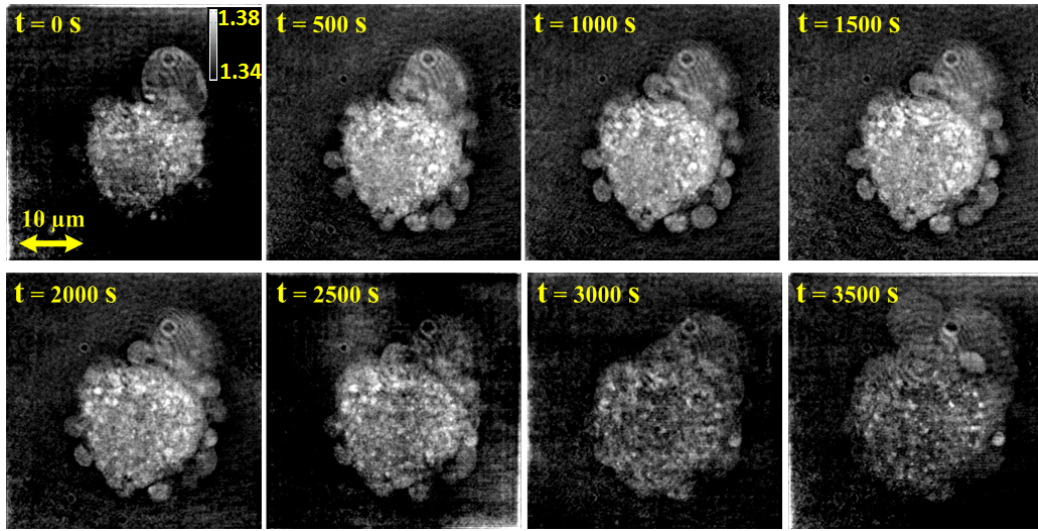


Figure 8.2: 3D refractive index reconstruction of MCF7 cell apoptosis. Each sub-figure shows the same cell after 500 seconds. The total time slap is around 1 hour.

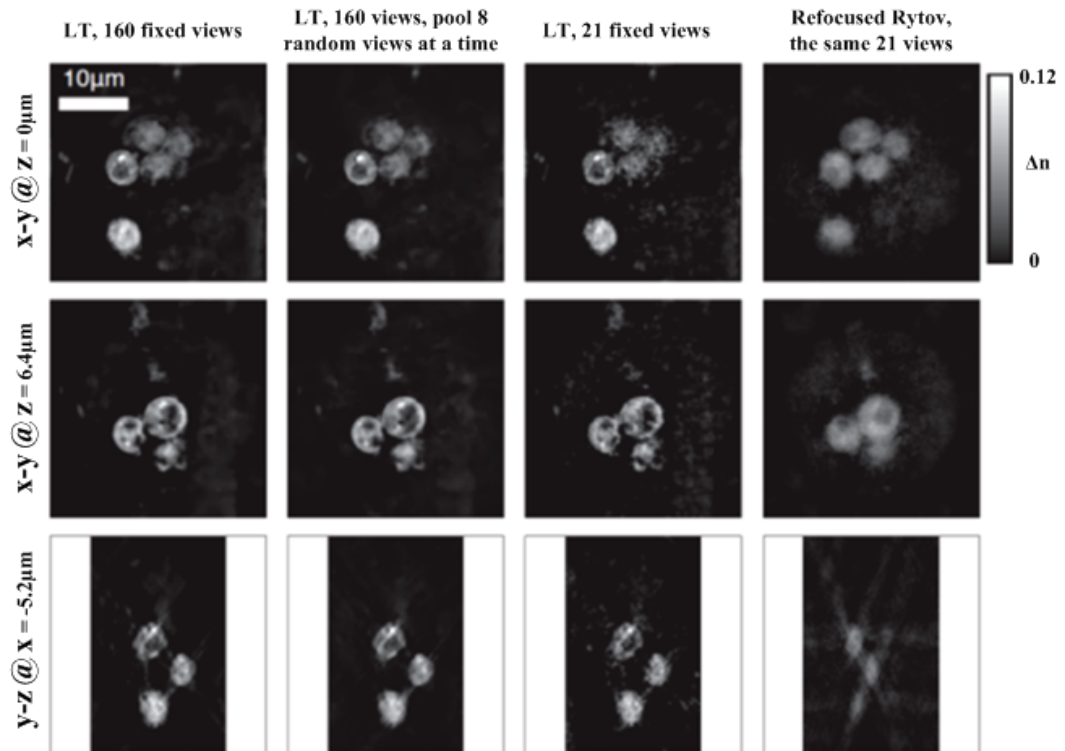


Figure 8.3: Iterative refocused Rytov and learning tomography reconstruction of two layers of Yeast cells for two different depths while the number of the angles used in reconstruction is reduced.

8.3 Comparison with existing imaging techniques

In this section, we present some final comparison with the existing techniques such as Born [4], Rytov [5], Refocused Rytov [6] as well as the commercially available techniques such as florescent [7], reflection [8] and transmission confocal [9]. In Figure 8.3, the first row presents $x - y$ section of the reconstruction. The first column shows learning tomography based on optimizing all 160 views in each iteration. In the second column, one can see LT for optimization over 8 randomly selected views in each iteration. LT using 21 fixed views is presented in the third column and refocused Rytov with 21 views is presented in the last column. The second row is the same scenario for the plan containing the other layer of cells (experimentally out of focus). And the last row shows the $y - z$ sections, respectively. One can see that Rytov performance severely degrades while using fewer views in reconstruction whereas LT degrades much less.

In order to assess the different tomographic methods, we prepared artificial tissue samples consisting in three-dimensional clusters of living yeast cells embedded in a transparent water-based agarose gel (see Figure 5.1). The concentration of the cells can be controlled in order to yield samples with different optical thicknesses and complexity. In Figure 8.4, for comparison, we show how each method performs on a sample consisting of a two-layer cell cluster.

The simplest tomography inversion method handling diffraction relies on the first Born approximation [4]. It is equivalent to the assumption of single scattering and, therefore, induces a linear mapping between the scattering potential and the scattered field. For each view, the far field scattered from the object is directly mapped to the three-dimensional Fourier transform of the object. The Born approximation requires the scattered field to be small and consequently degrades as the size of the object increases. In particular, this method suffers from phase wrapping as it can be seen in Figure 8.4. Some bright features, associated to a large refractive index in the cells, are visible in the Rytov reconstruction [5], but the corresponding feature in the Born reconstruction appear dark, that is, with a low index. Indeed, the refractive index of a region within the sample can be changed to a value that modifies the optical path of the rays going through it by an integer number of wavelength. Such an index change alters the measurement mostly in region where diffraction is significant, such as close to interfaces. The phase measured within extended areas such as the cell nucleus or vacuoles will only be altered minimally. This leads to an ambiguity in the value of the refractive index. This example illustrate that the Born approximation breaks down very early such as for the example shown in Figure 8.4.

Part of the phase wrapping problem can be solved by resorting to the Rytov approximation. In that case, the optical field is expressed as a complex phase factor. It happens to be possible to use this phase to perform the reconstruction instead of the field used for the Born reconstruction. The crucial advantage of this approach is that the phase of each measurement can be unwrapped explicitly, for example with the PUMA algorithm [10]. In Figure 8.4, we can see that the proper contrast

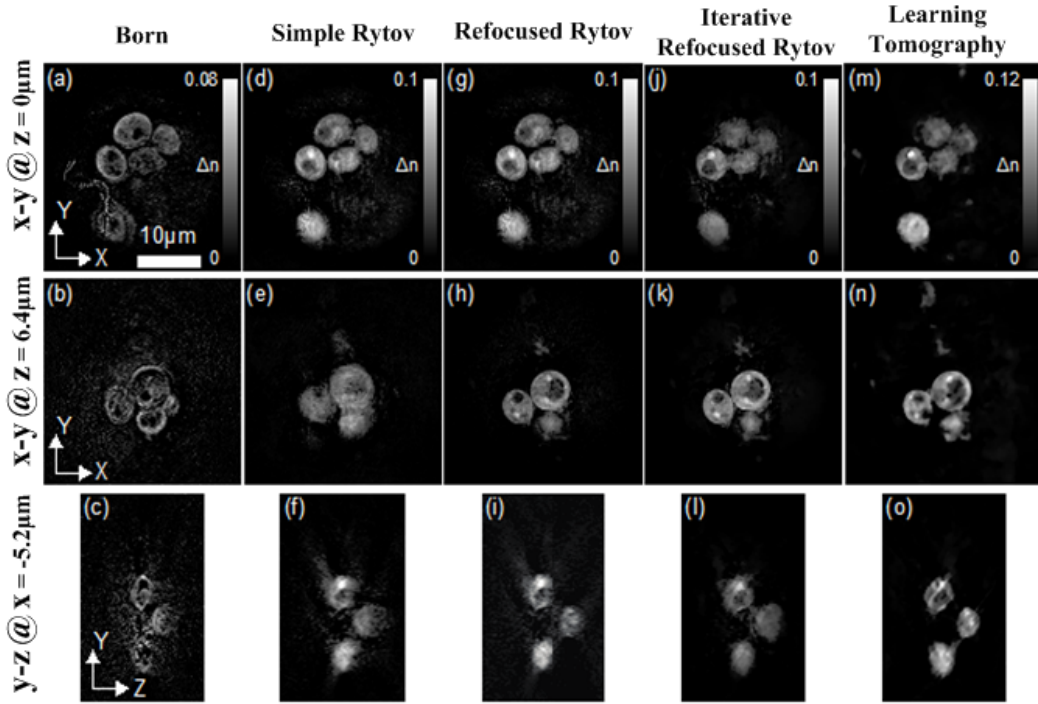


Figure 8.4: Reconstruction of the refractive index distribution of a two-layer yeast cells cluster using different methods: (a-c) Wolf transform with Born approximation [4]. (d-f) Wolf transform with Rytov approximation [5]. (g-i) Wolf transform with Rytov approximation refocused on two different $x - y$ planes (g,h) [6]. (j-l) Iterative linear algorithm based on Rytov approximation with TV regularization. (m-o) LT reconstruction with TV regularization. In (a-c), the phase wrapping leading to a refractive index contrast inversion is clearly visible. The effect of refocusing can be seen by comparing the slice in the plane $z = 6.4 \mu m$ without refocusing (e) and with refocusing (h). LT is automatically focused on all slices.

is restored. However, in the case of Rytov approximation, the reconstruction gets blurred for planes away from the image plane, which is the plane in which the field was measured and unwrapped. This is clear from Figure 8.4 (e). This phenomenon can be explained by the fact that the quantity we use for the reconstruction, namely the phase of the field instead of the field itself, does not obey the wave equation. In other words, the phase does not propagate like the field and the inversion formula valid in the case of Born approximation is only valid at the image plane in the case of Rytov approximation. This issue can be solved by digitally refocusing each view on the plane of interest within the sample [6]. As the Rytov reconstruction only gradually blurs out away from the image plane it may not be necessary to operate such a refocusing for all the layer in the reconstruction. It is however recommended that the refocusing be performed on every plane containing prominent features. In the example shown in Figure 8.4, we refocused on the two layers of cells overlapping each other. Both layers shown in Figure 8.4 (g, h) are in focus now. Because the refocusing involves a propagation step, the phase of the field wraps again. For each refocused plane, all the views need to be unwrapped again. This operation may be time consuming especially if the phase pattern is complex, which is the case when several layers of cells overlap.

A further improvement in reconstruction quality can be obtained by using LT which is based on a nonlinear scattering model more accurate than the single scattering assumption of Born and Rytov approximation. As such, the method is expected to handle multiple scattering and to extend the reach of tomography to thicker and more complex samples. The cost function that is minimized, contains a measurement error term and a regularization term. The regularization term is an operator representing prior knowledge about the sample. In the case of the cell cluster presented here, we use a total variation regularization that yield piecewise constant refractive index distributions, which is what we naturally expect in cells. The refocusing problem encountered in the Rytov method is naturally solved in LT as it makes use of a Fresnel propagation model. LT being an iterative method, an initial guess is required to start the optimization. In general, the closer the initial guess is to the solution, the less likely is the algorithm to fall in local minima. The reconstruction shown in Figure 8.4 (m-o) was initialized with a constant refractive index value. In that case, because the sample was relatively simple, with a total phase shift rarely exceeding 2π , the LT converged to the correct index distribution. We will see below that, for more complex sample with larger accumulated phase, a better initial guess is required.

Finally, we devised an iterative (refocused) Rytov method [6] containing a regularization step as well in order to have a fair comparison with the LT reconstruction. In essence, the only difference between the LT and the iterative Rytov is the forward model, which, for the latter, is the linear Wolf transform, the regularization step being identical. In Figure 8.4 (j-l), we show the iterative Rytov reconstruction. Even though the cost function has been minimized, the improvement in image quality over the direct Rytov inversion is very marginal. This is in general the case for that type of sample. Note that the iterative Rytov is still a linear method

and, even though it benefits from prior information through the regularization, it does not account for multiple scattering and is thus inherently limited.

In Figure 8.5, we show several slices through index reconstructions of the sample consisting of up to five layers of cells. The phase delay induced by the cells is of the order of 4π on average. The refractive index contrast of the cells above the background value ($n_0 = 1.34$) is of 0.07 on average. In that case, the Born reconstruction is very strongly impaired by phase wrapping and the overlapping cells cannot be distinguished from each other. The Rytov reconstruction in Figure 8.5 (a-f) shows most of the cells close to the image plane thanks to the successful unwrapping of the measurements. However, the cells farther from the image plane are barely visible as shown in Figure 8.5(a) and (e). Refocusing the measurement on the planes corresponding to each one of the five displayed sections restores the missing cells.

In the case of such a thick sample, the unwrapping is a necessary step for tomographic imaging as far as the methods presented here are concerned. The LT algorithm from a constant initial guess (flat refractive index distribution) did not converge. We therefore initialized it with the refocused Rytov solution (Figure 8.5 center column), which is closer to the local minima. Note that, in general, Rytov tomography suffers from the missing cone problem, i.e. from the fact that the viewing angle is limited by the detection optics (numerical aperture of the imaging objective). As a consequence of missing areas in the Fourier spectrum, the refractive index is slightly underestimated, which explains the different scale color bars in Figure 8.5. LT is able to restore the proper index contrast as the initial was close enough to the global minima. In the LT reconstruction, cells close to the edge of the image were not present in the initial guess. LT put them back; hence, the combination of refocused Rytov reconstruction and further improvement by LT is important to achieve accurate imaging of thick samples.

8.4 Comparing with commercially available imaging techniques

In this section, we compare Rytov, Refocused Rytov, LT, Florescent, Transmission and Reflection Confocal for a thick sample containing several layers of Yeast cells. From Figure 8.6 one can conclude that in the Rytov reconstruction, there is lots of background noise and missing cone artifact which is strongly reduced in Refocused Rytov. LT gets rid of almost all of this noise and artifact. In Reflection Confocal, the reconstruction is better in the sections closer to light source but strongly degrades after some layers of cells which is due to the fact that the reflected light gets weaker and weaker. In the fluorescent reconstruction, there is lots of background noise and also the signal is weaker in the part containing multiple layers of cells. Transmission Confocal also cannot perform a good reconstruction for the places containing several layers of cells. Hence, LT reconstruction is the best method with a clearly visible outperformance in the case of multiple layered cells.

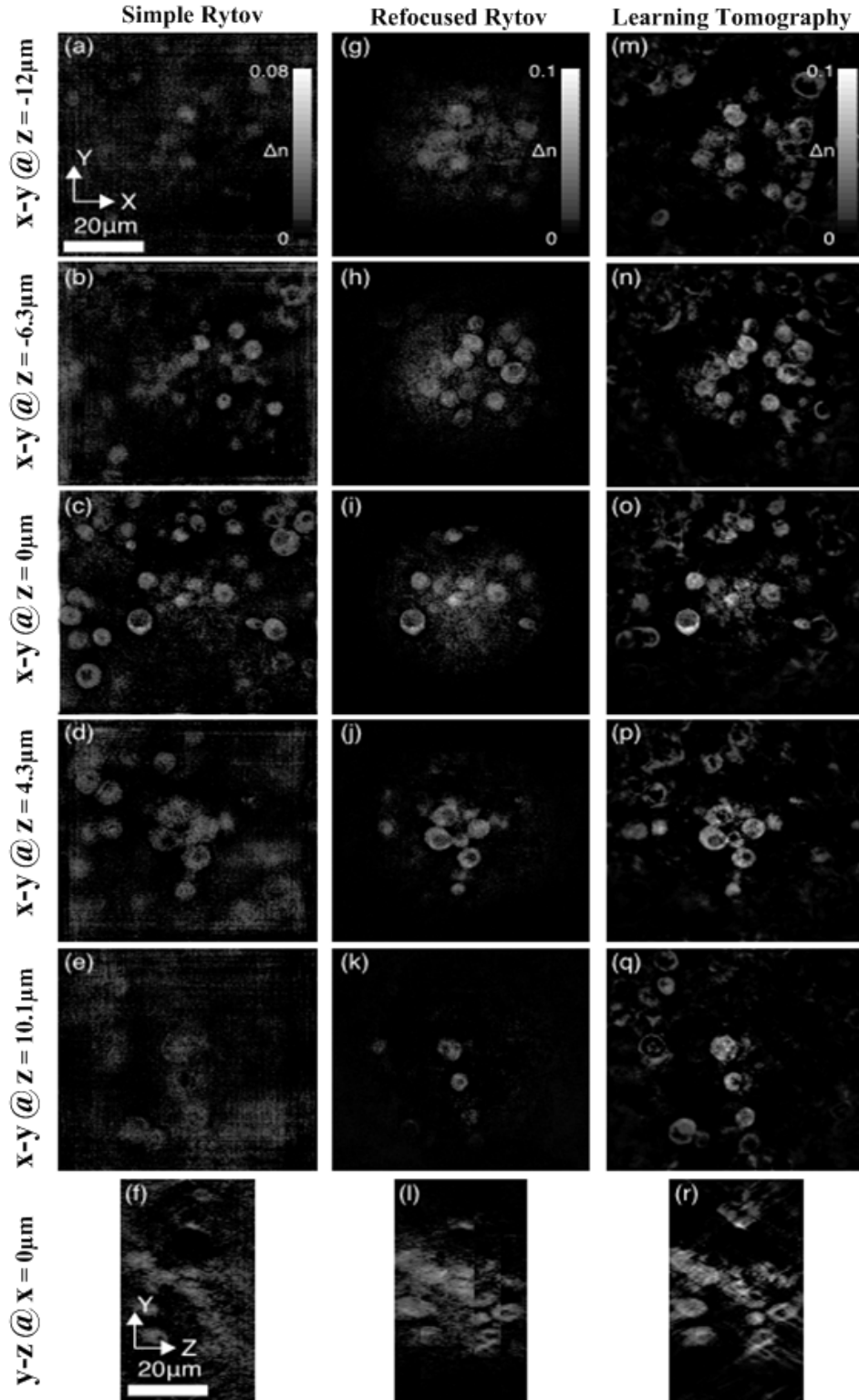


Figure 8.5: Refractive index reconstruction of a cluster with five layers of cells. (a-e) $x - y$ slices through the simple Rytov reconstruction at increasing depths ((f) $y - z$ slice). (g-k) $x - y$ slices through the refocused Rytov reconstruction ((l) $y - z$ slice). The stitching between the five refocused regions is clearly visible. (m-r) Corresponding slices through the LT reconstruction. The initial guess for the LT algorithm in this case was the refocused Rytov reconstruction in the central column.

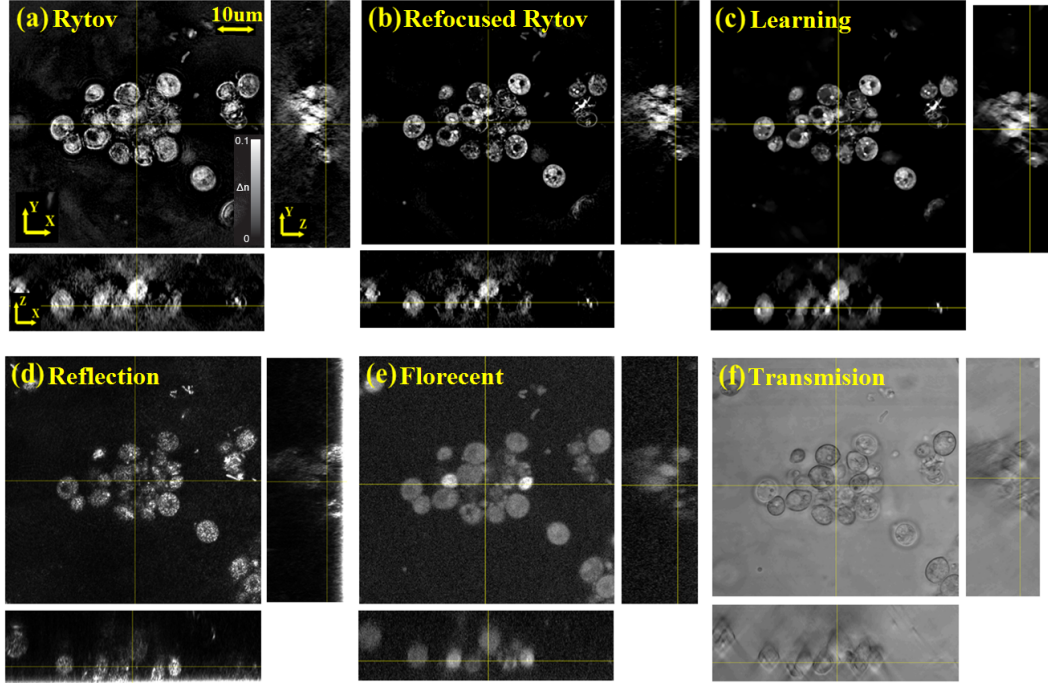


Figure 8.6: comparison of the proposed method with existing and commercially available imaging techniques

8.5 Comparison of computation costs

In this section, we compare the computation costs for the different methods described previously. Two processes have a significant impact on the execution time, namely regularization and phase unwrapping of the measurement. The execution time of regularization and phase unwrapping is given in Table 8.1 for two examples. The total execution is thus strongly impacted depending on whether an iterative method with regularization is used and whether refocusing is required. In particular, the LT and refocused Rytov yield similar image quality in the planes where Rytov measurements have been refocused. The question is then, on how many planes we need to refocus Rytov measurements in order to get a global reconstruction with a quality similar to that of LT. For the cluster of cell shown above, single-plane Rytov is clearly not enough. For the five-layer sample, the version with five refocused planes is better but globally, the LT has lower background noise and was, in that case, faster to process. In Table 8.1, we compare the computation costs and execution time for all the described methods. The computation costs are given as the required number of operations, simple point-by-point multiplications being neglected. The cost are calculated for two examples, with the corresponding measured processing time by running the MATLAB software

on an Intel Core i7 processor running at 2.8GHz, single thread. The algorithm used for phase unwrapping is PUMA [10]. TV regularization is performed using an iterative optimization for which we performed 20 iterations in each case. The total execution times shown in Table 8.1 were extrapolated from the measured timing of elementary blocks multiplied by the number of views and iterations. For the TV regularization, the function with 20 iterations was timed as a whole. The execution times can be reduced through parallelization. The most straightforward parallelization can be implemented on the LT algorithm by processing the views separately. Massive parallelization of the Fourier transform is also possible through the use of dedicated graphic processing units.

Method	Approximate theoretical computational cost	Example 1 execution time ⁽²⁾	Example 2 execution time
Born	$C_{\text{Born}} = N_v \times N_x^2 \log(N_x^2) + N_x^2 N_z \log(N_x^2 N_z)$	3.5s	3.5s
Rytov	$C_{\text{Rytov}} = C_{\text{Born}} + N_v \times C_{\text{unwrap}}$	5min42s	5min42s
Refocused Rytov	$C_{\text{refoc}} = N_{\text{refoc}} \times [C_{\text{Rytov}} + N_v \times N_x^2 \log(N_x^2)]$	11min	28min
Iterative refocused Rytov	$C_{\text{itlin}} = N_{\text{refoc}} \times N_{\text{iter}} \times (2N_x^2 N_z \log(N_x^2 N_z) + C_{\text{reg}}) + C_{\text{refoc}}$	3h38min	16h45min
Learning Tomography	$C_{\text{LT}} = N_{\text{iter}} \times (N_{v,\text{eff}} \times 6N_z N_x^2 \log(N_x^2) + C_{\text{reg}}) + C_{\text{refoc}}^{(1)}$	5h47min	6h04min
TV regularization in 20 iterations	$C_{\text{reg}} = N_x^{3.36}$ (real-valued function) execution time (s) = $N_x^{3.36} \times 4.9 \times 10^{-7}$	4min57s (3h18min) ⁽³⁾	4min57s (3h18min) ⁽³⁾
Phase unwrapping with PUMA	$C_{\text{unwrap}} = N_x^{2.81}$, execution time (s) = $N_x^{2.81} \times 5.1 \times 10^{-8}$	2.1s (5min35s) ⁽³⁾	2.1s (28min) ⁽³⁾

(1) In example 1, the algorithm is started from a constant index distribution and this last term is suppressed.

(2) Execution time not including the time required to read the data from the disk.

(3) We indicate in parenthesis the total time considering the number of iterations and the number of refocused planes.

Table 8.1: Computation cost and execution times of the different methods for two examples.

Example 1: Data set shown in Figure 8.4, with $N_v = 160$, $N_{v,\text{eff}} = 8$, $N_x = 512$, $N_z = 265$, $N_{\text{iter}} = 40$, $N_{\text{refoc}} = 1$, $C_{\text{unwrap}} = N \times 2.81$. Example 2: Data set shown in Figure 8.5, with $N_v = 160$, $N_{v,\text{eff}} = 8$, $N_x = 512$, $N_z = 265$, $N_{\text{iter}} = 40$, $N_{\text{refoc}} = 5$, $C_{\text{unwrap}} = N \times 2.81$.

Note that the measurement time for tomography is only dependent on the number of views, which is limited by the frame rate of the detector and the photon budget. The use of regularization allows us to use a lesser number of views, typically 20. The current frame rate of the detector is 40fps, which allows us to produce 2 three-dimensional reconstructions per second. This already enables imaging of dynamical biological processes.

8.6 Conclusion

LT technique based on intensity measurements was investigated on the already presented HeLa cells. We investigate a live MCF7 cells blebbing as it is dying to illustrate that since the proposed method is phase contrast base and does not need any kind of staining it is useful for live cell imaging. Then some final comparisons with the existing techniques such as Born, Rytov, Refocused Rytov as well as the commercially available techniques such as florescent, reflection and transmission confocal was presented. At the end, we compare and investigate the complexity and cost of the proposed LT with existing methods.

8.7 Bibliography

- [1] M. H. Maleki, and A. J. Devaney. "Phase-retrieval and intensity-only reconstruction algorithms for optical diffraction tomography." *JOSA A* 10, no. 5 (1993): 1086-1092.
- [2] G. Gbur, and E. Wolf. "Diffraction tomography without phase information." *Optics letters* 27, no. 21 (2002): 1890-1892.
- [3] G. Gbur, M. A. Anastasio, Y. Huang, and D. Shi. "Spherical-wave intensity diffraction tomography." *JOSA A* 22, no. 2 (2005): 230-238.
- [4] E. Wolf, "Three-dimensional structure determination of semi-transparent objects from holographic data," *Opt. Commun.* 1, 153-156 (1969).
- [5] Devaney, A. J., "Inverse-scattering theory within the Rytov approximation," *Optics letters* 6, no. 8 (1981): 374-376.
- [6] Alexandre Goy, Morteza H. Shoreh, JooWon Lim, Michael Unser, and Demetri Psaltis, "Imaging thick samples with optical tomography." *arXiv preprint arXiv:1711.03714* (2017).
- [7] W. Denk, J. H. Strickler, and W. W. Webb, "Two-photon laser scanning fluorescence microscopy," *Science* 248, no. 4951 (1990): 73-76.
- [8] A. Diaspro, "Confocal and two-photon microscopy: foundations, applications and advances," by Alberto Diaspro (Editor), pp. 576. ISBN 0-471-40920-0. Wiley-VCH, November 2001. (2001): 576.
- [9] J. B. Pawley, "Fundamental limits in confocal microscopy," In *Handbook of biological confocal microscopy*, pp. 20-42. Springer US, 2006.
- [10] J. M. Bioucas-Dias and G. Valadão, "Phase unwrapping via graph cuts," *IEEE Trans. Image Process.* 16, 698-709 (2007).

Conclusions and Future Works

Contents

9.1 Conclusions	92
9.2 Future works	93

In conclusion, we went over some of the newest optical reconstruction techniques that exist in the technical literature, and discussed some of the base and leading ideas and papers. Then, we proposed a neural-network-inspired algorithm to solve the optical phase tomography problem which we applied on to synthetic and biological samples. A conventional phase tomography with coherent light and off axis recording was performed. The scattering of the sample was modeled as a neural network. BPM was used to model scattering and each x-y plane was modeled by a layer of neurons. The network's output (simulated data) was compared with the experimental measurements, and the error was used for correcting the weights which are refractive index of each node in the neurons using standard error back-propagation techniques. It was shown that compared to other exiting algorithm the result of ours have better quality. In particular, parasitic angular structures and the missing cone artifact was removed. Overall, although the perspectives of our approach are pretty rich for high-resolution tomographic imaging in a range of practical setups. There are some limitations that can be addressed in future works. Even though, there were not any convergence problems, the nonlinear nature of the forward model makes it difficult to analyze the theoretical convergence of the method. Another possibility would be using arbitrary illumination patterns and wavefront shaping instead of just changing the angle of illumination. This makes the proposed method more general than its linear counterparts based on Radon or on diffraction tomography. Another interesting idea would be investigation of the proposed method for different and less standard illumination patterns. The resolution conserving regularization was discussed and a method for selecting regularization parameters was proposed. It was shown that LT achieves better performance with smaller number of measurements than other techniques, such as, DT. The rule of regularization in obtaining higher fidelity images without losing resolution was discussed. It was experimentally illustrated that due to overcoming multiple scattering the LT reconstruction greatly outperform the DT reconstruction while the sample contain two or more layers of cells or beads. Initialization, local minima and phase unwrapping problems were discussed and some solution to avoid them was investigated. An example of reconstruction using intensity measurement was provided. 3D reconstruction of a live cell during oapoptosis was presented in a 3D time-lapse format. At the end, we provided a final comparison with existing and commercially available systems.

9.1 Conclusions

The **First Chapter** provides an overview of the following chapters, their relationship and their contribution to the fulfillment of the desired goal. In **Chapter 2**, we investigated some of the newest optical reconstruction techniques that exist in the technical literature, and discussed some of the base and leading ideas and papers in more details.

In **Chapter 3**, we demonstrated a neural-network based algorithm to solve the optical phase tomography problem which is applied to biological (HeLa and hTERT-RPE1 cells) and synthetic (polystyrene beads) samples. The experimental measurements were performed with a conventional phase tomography setup, using coherent collimated illumination and off-axis holography. The sample scattering potential was modeled as a neural network implemented by a forward beam propagation method. The network is organized in layers of neurons, each representing an x-y plane in the BPM. The network's output is compared to the experimental measurements and the error is used to correct the weights of the neurons (representing the refractive index contrast) using standard error back propagation techniques. The algorithm yields images of better quality than other tomographic reconstruction methods. In particular, the missing cone artifact is efficiently reduced, as well as parasitic granular structures. The results indicate that whether starting from a constant initial guess for the refractive index or with a conventional Radon tomographic image, the method essentially converges to the same result after around 100 iterations. This approach opens rich perspectives for active correction of scattering in biological samples; in particular, it has the potential of increasing the resolution and the contrast in fluorescent and two-photon imaging.

In **Chapter 4**, the novel algorithm for estimating the refractive index distribution of a 3D object from the transmitted light-field measurements was presented. The proposed method relies on a nonlinear forward model, which is based on simulating the physical propagation of electromagnetic waves with BPM. We compensated the ill-posedness of the inverse problem, by imposing positivity as well as the gradient-sparsity to the solution. The method is computationally efficient due to the time-reversal scheme for computing the gradients and evaluating only a subset of gradients at each iteration. Overall, we believe that our approach opens rich perspectives for high-resolution tomographic imaging in a range of practical setups. It was demonstrated that even when the number of measurements is severely restricted, the proposed method can recover 3D objects with surprisingly high-quality.

In **Chapter 5**, the capabilities of the refocused Rytov and the Learning Tomography algorithms in 3D reconstruction of thick samples consisting of yeast cell clusters was experimentally explored. The LT algorithm yields satisfactory results in terms of sharpness and background noise when starting from the Rytov. We concluded that LT has the capability of filling gaps in the initial guess over a range larger than the range of validity of the Rytov approximation. Moreover, even in planes in which the Rytov solution has been refocused, generally LT yields sharper

images. We believe that this is because of accounting for multiple scattering. For thick but weakly scattering objects, the Rytov solution can be quite close to the LT solution. However, for the Rytov reconstruction to be of comparable quality, the measurement needs to be refocused on at least one plane within the range of validity of the approximation, which is roughly 1 micron in this type of sample. For a 30 micron sample, we would need 30 refocused Rytov solutions. The phase unwrapping that is part of each Rytov reconstruction generally dwarfs the computational cost of the optimization in the LT algorithm. Therefore, refocused Rytov is generally much more expensive in terms of computation time.

Chapter 6 went over the local minima problem and discussed ways of getting out of them. We investigated the influence of the initialization on the convergence of the algorithm and concluded that is essential for high-quality imaging in strongly scattering scenarios. The error landscape was presented showing the local minima problem for two different accumulated phase scenarios with and without regularization. Experimental results for different initializations was provided and their convergences were investigated. At the end, we discussed phase unwrapping problem and compared different phase unwrapping methods for our experimental data.

In **Chapter 7**, it was experimentally illustrated that due to overcoming multiple scattering the LT reconstruction greatly outperform the DT when the sample contains two or more layers of cells or beads. The reconstruction of the two beads stacked in z was compared with the superposition of the individual beads showing a significant left over due to multiple scattering for DT, whereas in the case of LT, the superposition of the individual reconstructions overlaps well with the reconstruction of the two beads together.

In **Chapter 8**, LT technique based on intensity measurements was investigated on the previously presented HeLa cell. We also investigate a live MCF7 cells blebbing during apoptosis to illustrate the proposed method can be used to analyze cell behavior in vivo-like systems. Then, some final comparisons with the existing techniques such as Born, Rytov, Refocused Rytov as well as the commercially available techniques such as florescent, reflection and transmission confocal was presented. At the end, the complexity and cost of different methods were compared and discussed.

Chapter 9 presents the conclusion of the results and potential research and development threads for the future studies. Some of these threads are being pursued by other Lab members.

9.2 Future works

Although this project has excellent outcome until now, resulting in several high impact journal publication, the future path for it can be even more flourishing. First, our forward model can handle arbitrary illumination patterns. This makes it much more general than its linear counterparts that are based on Radon or diffrac-

tion tomography. Accordingly, one avenue of work would be investigating the performance of the proposed method under different and less standard types of illumination. Second, it is possible to consider reflection as well and try to combine the information of the transmission and reflection to get higher accuracy. Combining phase unwrapping with the learning algorithm would be another hot area of research. Another important area of work could be reconstructing based on intensity measurements instead of phase. Transport of intensity or multi wavelength measurements can be used to extract the phase out of intensity measurements as well. Although, in practice, we did not encounter any convergence problems, the nonlinear nature of the forward model makes the theoretical convergence of the method difficult to analyze. Theoretical convergence analysis can be investigated resulting in a strong publication. Combining with methods such as florescent, STED, etc. will open a whole new area of research as well.

Appendix

Contents

A.1 Comparison between different methods	95
A.1.1 Limited angles reconstruction	95
A.2 Fourier Beam-Propagation Method	98
A.2.1 Paraxial Helmholtz equation	99
A.2.2 Fourier beam-propagation	100
A.3 Total variation minimization	101
A.3.1 Two variants of TV	102
A.3.2 Minimization of TV	103
A.4 Bibliography	105

A.1 Comparison between different methods

The images shown in Figure A.1 correspond to the four different tomographic reconstruction methods that were investigated in Figure 3.6. The top row shows the image obtained by LT after 100 iterations. Figure A.1 (a, b, c) are the x-y, y-z and x-z cross-sections, respectively. The initial condition in this case was a constant. The same reconstruction was obtained with the learning algorithm with each of the other three initial conditions that are included in Figure 3.6. These three initial conditions are shown in the bottom three rows in Figure A.1. The second row shows the Radon reconstruction, the third is the iterative Radon [1], and the bottom row is DT [2] reconstruction. The error reduction due to the learning algorithm translates in a clear image quality improvement compared to all the other cases in this figure.

A.1.1 Limited angles reconstruction

Figure A.2 shows similar results except in this case, only 40 equally spaced illumination angles were used for all the tomographic reconstructions rather than the 80 angles used in obtaining the results in Figure A.1. In other words, the angular range of the illumination was reduced to half of the range of Figure A.1. The second, third and fourth rows in Figure A.2 are the Radon, iterative Radon, and DT reconstruction as in Figure A.1 except with only 40 illumination angles. As

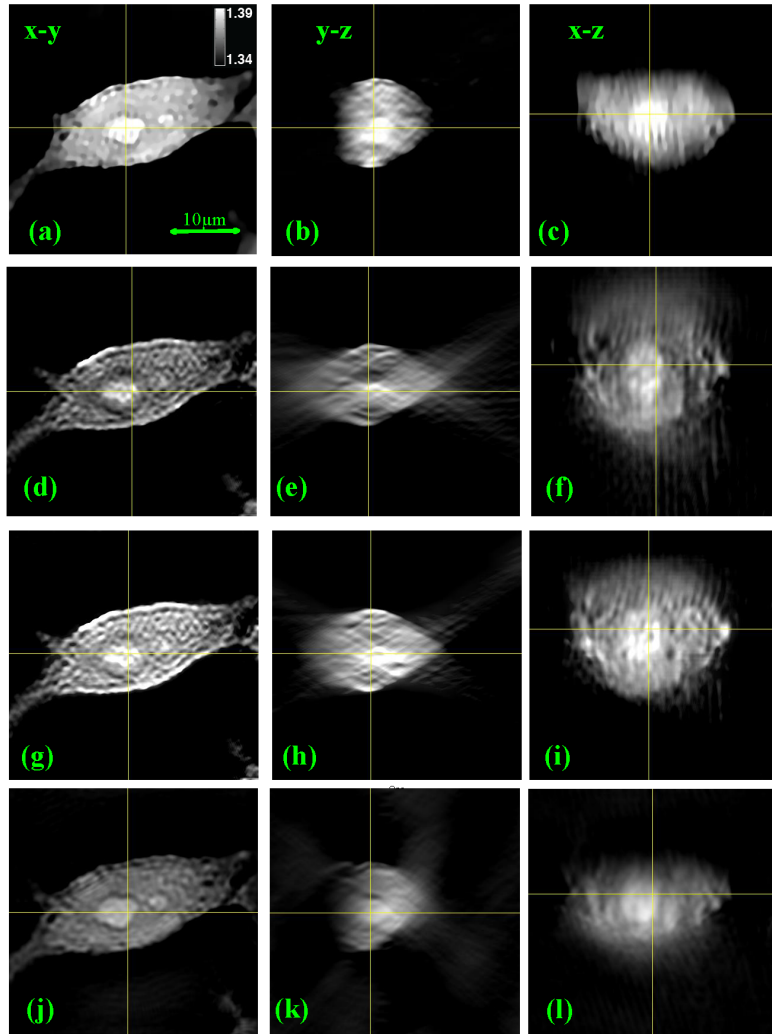


Figure A.1: Comparison of the cross-sectional reconstruction on the x-y, x-z, y-z planes for (a)-(c) LT reconstruction with zero initialization, (d)-(f) Radon reconstruction [1], (g)-(i) Iterative Radon reconstruction [1], (a)-(c) Optical DT reconstruction [2] for full angle illumination (80 angle).

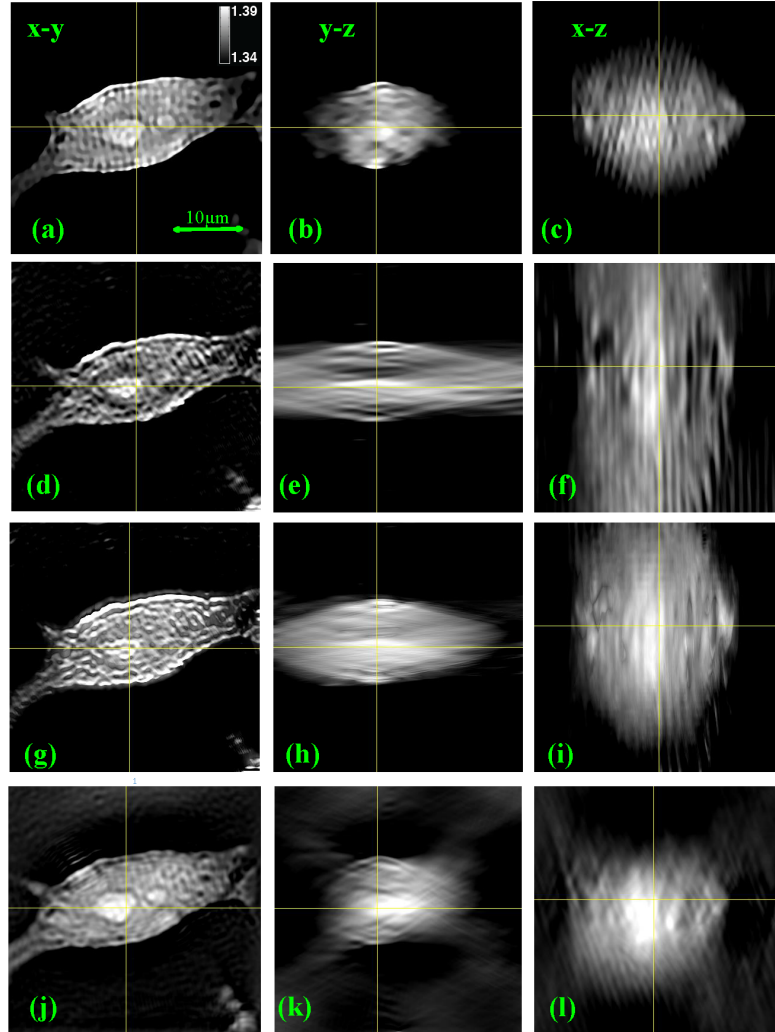


Figure A.2: Comparison of the cross-sectional reconstruction on the x-y, x-z, y-z planes for (a)-(c) LT reconstruction with DT initialization, (d)-(f) Radon reconstruction [1], (g)-(i) Iterative Radon reconstruction [1], (j)-(l) Optical DT reconstruction [2] for half angle illumination (40 angle).

expected, there is evident deterioration in resolution in z and some loss of image quality in the x - y cross-sections (the mean squared error is larger). The top row in Figure A.1 is the tomographic reconstruction obtained after 100 iterations with the learning algorithm. The initial condition in this case was DT reconstruction in Figure A.2. The error minimized by the learning algorithm is plotted in Figure A.3 as a function of iteration number. Inspection of the top and bottom rows of Figure A.2 confirms that the reduction in mean square error by the learning algorithm translates in an improvement of image quality. We also ran the learning algorithm with a constant initial condition for the case of 40 angles of incidence and the resulting error is also plotted in Figure A.3 as a function of iteration number. The image at which the LT algorithm converges has lower error than DT reconstruction. However, after fifty iterations the error for constant initialization remains larger than the error of the image produced when the system was initialized with the DT reconstruction.

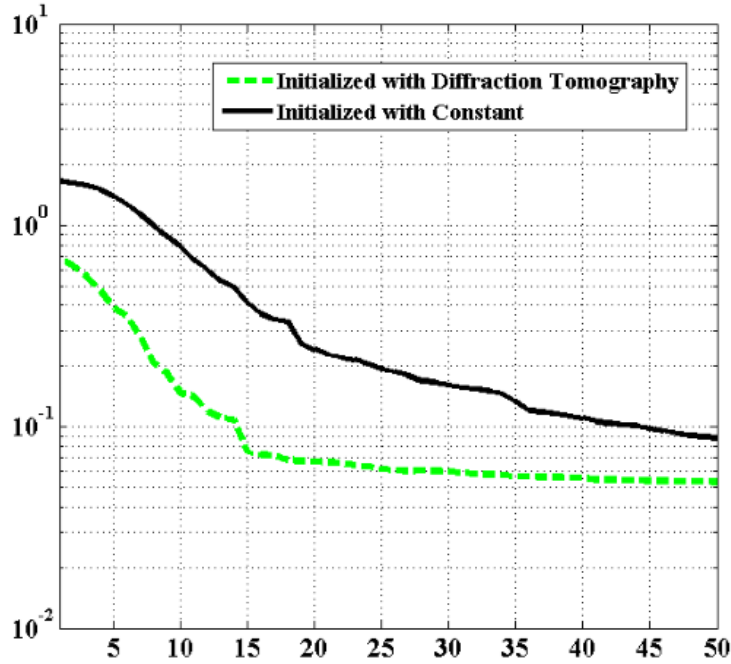


Figure A.3: The error between the experimental measurements and the predictions of the computational model plotted as a function of the number of iterations for 40 angles of illumination and two different initial conditions: Constant index (black), DT [2] (green).

A.2 Fourier Beam-Propagation Method

In this section, we present the full derivation that supports the use of BPM as a forward model. We start by introducing the inhomogeneous Helmholtz equa-

tion that completely characterizes the light field at all spatial positions in a time-independent form [3]. We then describe the important paraxial simplification of the Helmholtz equation, which is often used for describing the propagation of electromagnetic waves. Note that the derivations here are based on the paraxial version of BPM, which is simpler to derive, but is slightly less accurate than the nonparaxial version [4] used in (4.3). While an extensive discussion on the merits and drawbacks of either version is beyond the scope of this thesis, both versions are sufficiently accurate to be used in the experiments presented in this thesis.

A.2.1 Paraxial Helmholtz equation

Our starting point is the scalar inhomogeneous Helmholtz equation

$$(\Delta + k^2(\mathbf{r})\mathbf{I}) u(\mathbf{r}) = 0,$$

where $\mathbf{r} = (x, y, z)$ denotes a spatial position, u is the total light-field at \mathbf{r} , $\Delta = (\partial^2/\partial x^2 + \partial^2/\partial y^2 + \partial^2/\partial z^2)$ is the Laplacian, \mathbf{I} is the identity operator, and $k(\mathbf{r}) = \omega/c(\mathbf{r})$ is the wavenumber of the light field at \mathbf{r} . Equation (4.1) implicitly describes the relationship between the refractive index and the light field everywhere in space. The spatial dependence of the wavenumber k is due to variations of the speed of light c induced by the inhomogeneous nature of the medium under consideration. Specifically, the wavenumber in (4.1) can be decomposed as follows

$$k(\mathbf{r}) = k_0 n(\mathbf{r}) = k_0(n_0 + \delta n(\mathbf{r})),$$

where $k_0 = \omega/c_0$ is the wavenumber in the free space, with $c_0 \approx 3 \times 10^8$ m/s being the speed of light in free space. The quantity n is the spatially varying refractive index of the sample, which we have written in terms of the refractive index of the medium n_0 and the perturbation δn due to inhomogeneities. We next develop the paraxial Helmholtz equation for the complex envelope $a(\mathbf{r})$ of the paraxial wave¹

$$u(\mathbf{r}) = a(\mathbf{r})e^{jk_0 n_0 z}. \quad (\text{A.1})$$

One way to interpret (A.1) is to say that it corresponds to a plane wave propagating along z in the medium, modulated by the complex amplitude a . Now consider

$$\begin{aligned} \frac{\partial^2}{\partial z^2} u(\mathbf{r}) &= \frac{\partial}{\partial z} \left(\left(\frac{\partial a(\mathbf{r})}{\partial z} \right) e^{jk_0 n_0 z} + jk_0 n_0 a(\mathbf{r}) e^{jk_0 n_0 z} \right) \\ &= e^{jk_0 n_0 z} \left(\frac{\partial^2 a(\mathbf{r})}{\partial z^2} + 2jk_0 n_0 \left(\frac{\partial a(\mathbf{r})}{\partial z} \right) - k_0^2 n_0^2 a(\mathbf{r}) \right). \end{aligned} \quad (\text{A.2})$$

¹A wave is said to be paraxial if its wavefront normals are paraxial rays (i.e. when $\sin(\theta) \approx \theta$ is valid). The variation of a with position must be slow within the distance of a wavelength, so that the wave approximately maintains its underlying plane-wave nature.

By using this expression and substituting (A.1) into (4.1), we obtain

$$\begin{aligned}
 & (\Delta + k^2(\mathbf{r})\mathbf{I}) u(\mathbf{r}) \\
 &= \left(\Delta_{\perp} + \frac{\partial^2}{\partial z^2} + 2jk_0 n_0 \frac{\partial}{\partial z} - k_0^2 n_0^2 \mathbf{I} + k^2(\mathbf{r})\mathbf{I} \right) \\
 & \quad \times a(\mathbf{r}) e^{jk_0 n_0 z} \\
 &= \left(\Delta_{\perp} + \frac{\partial^2}{\partial z^2} + 2jk_0 n_0 \frac{\partial}{\partial z} + 2k_0^2 n_0 \delta n(\mathbf{r})\mathbf{I} + k_0^2 (\delta n(\mathbf{r}))^2 \mathbf{I} \right) \\
 & \quad \times a(\mathbf{r}) e^{jk_0 n_0 z} \\
 &= 0,
 \end{aligned} \tag{A.3}$$

where $\Delta_{\perp} = (\partial^2/\partial x^2 + \partial^2/\partial y^2)$ is the transverse Laplacian. We now introduce two simplifications. The first is the slowly varying envelope approximation (SVEA), which is valid when $|(\partial^2/\partial z^2)a| \ll |k_0 n_0 (\partial/\partial z)a|$ and which allows us to suppress the second derivative of a in z [3, 5]. In the second simplification, we ignore the term $(\delta n)^2$. Thus, we obtain

$$\frac{\partial}{\partial z} a(\mathbf{r}) = \left(j \frac{1}{2k_0 n_0} \Delta_{\perp} + jk_0 \delta n(\mathbf{r})\mathbf{I} \right) a(\mathbf{r}). \tag{A.4}$$

Equation (A.4) is the slowly varying envelope approximation of the Helmholtz equation and is often referred to as the paraxial Helmholtz equation [5].

A.2.2 Fourier beam-propagation

BPM is a class of algorithms designed for calculating the optical field distribution in space or in time given initial conditions [6]. The paraxial Helmholtz equation (A.4) is an evolution equation in which the space coordinate z plays the role of evolution parameter.

We start by rewriting (A.4) in the operator form

$$\frac{\partial}{\partial z} a(\mathbf{r}) = D\{a\}(\mathbf{r}) + N\{a\}(\mathbf{r}), \tag{A.5}$$

where

$$D \triangleq j \frac{1}{2k_0 n_0} \Delta_{\perp} \quad \text{and} \quad N \triangleq jk_0 \delta n(\mathbf{r})\mathbf{I}.$$

Note that the operator D is linear and translation-invariant (LTI), while the operator N corresponds to a pointwise multiplication. The solution of (A.5) at a sufficiently small $z = \delta z$ may be written formally as a complex exponential²

$$a(x, y, \delta z) = e^{(D+N)\delta z} a(x, y, 0). \tag{A.6}$$

²Note that for an operator T , we define a new operator e^{Tz} in terms of series expansion $e^{Tz} \triangleq \sum_{n=0}^{\infty} \frac{z^n}{n!} T^n$. Hence, for $a(\mathbf{r})$, we write $e^{Tz}\{a\}(\mathbf{r}) = \sum_{n=0}^{\infty} \frac{z^n}{n!} T^n\{a\}(\mathbf{r})$.

The operators $\exp(Dz)$ and $\exp(Nz)$ do a priori not commute; however, Baker-Campbell-Hausdorff formula [7] can be applied to show that the error from treating them as if they do will be of order δz^2 , if we are taking a small but a finite z step δz . This suggests the following approximation

$$a(x, y, z + \delta z) = e^{N\delta z} e^{D\delta z} a(x, y, z). \quad (\text{A.7})$$

Now, it is possible to get explicit expressions for the diffraction $\exp(D\delta z)$ and refraction $\exp(N\delta z)$ operators, since they are independent. Diffraction is handled in the Fourier domain as

$$a(\omega_x, \omega_y, z + \delta z) = e^{-j \frac{\omega_x^2 + \omega_y^2}{2k_0 n_0} \delta z} a(\omega_x, \omega_y, z), \quad (\text{A.8})$$

which can also be expressed, for a fixed z , with a 2D Fourier filtering formula

$$\begin{aligned} a(x, y, z + \delta z) \\ = \mathcal{F}^{-1} \left\{ \mathcal{F} \{a(\cdot, \cdot, z)\} \times e^{-j \frac{\omega_x^2 + \omega_y^2}{2k_0 n_0} \delta z} \right\}. \end{aligned} \quad (\text{A.9})$$

For refraction, we get

$$a(x, y, z + \delta z) = e^{jk_0(\delta n(r))\delta z} a(x, y, z), \quad (\text{A.10})$$

which amounts to a simple multiplication with a phase mask in the spatial domain.

A more refined version of BPM for simulating waves propagating at larger angles was derived by Feit and Flack [4]. By relying on their results, we can replace the diffraction step (A.9) by a more accurate alternative

$$\begin{aligned} a(x, y, z + \delta z) \\ = \mathcal{F}^{-1} \left\{ \mathcal{F} \{a(\cdot, \cdot, z)\} \times e^{-j \left(\frac{\omega_x^2 + \omega_y^2}{k_0 n_0 + \sqrt{k_0^2 n_0^2 - \omega_x^2 - \omega_y^2}} \right) \delta z} \right\}. \end{aligned} \quad (\text{A.11})$$

Our practical implementation in Section 4.2.2 relies on this *nonparaxial* version of BPM.

A.3 Total variation minimization

In this section, we discuss the concepts and algorithms behind total variation (TV) regularized image reconstruction (4.5). The material presented here is a review of the ideas that were originally developed by Beck and Teboulle in [8].

A.3.1 Two variants of TV

Two common variants of TV are *anisotropic* TV regularizer

$$\mathcal{R}(\mathbf{x}) \triangleq \sum_{n=1}^N \|[\mathbf{D}\mathbf{x}]_n\|_{\ell_1} \quad (\text{A.12a})$$

$$= \sum_{n=1}^N (|[\mathbf{D}_x\mathbf{x}]_n| + |[\mathbf{D}_y\mathbf{x}]_n| + |[\mathbf{D}_z\mathbf{x}]_n|) \quad (\text{A.12b})$$

and *isotropic* TV regularizer

$$\mathcal{R}(\mathbf{x}) \triangleq \sum_{n=1}^N \|[\mathbf{D}\mathbf{x}]_n\|_{\ell_2} \quad (\text{A.13a})$$

$$= \sum_{n=1}^N \sqrt{([\mathbf{D}_x\mathbf{x}]_n)^2 + ([\mathbf{D}_y\mathbf{x}]_n)^2 + ([\mathbf{D}_z\mathbf{x}]_n)^2} \quad (\text{A.13b})$$

Here, $\mathbf{D} : \mathbb{R}^N \rightarrow \mathbb{R}^{N \times 3}$ is the discrete gradient operator, with matrices \mathbf{D}_x , \mathbf{D}_y , and \mathbf{D}_z denoting the finite difference operators along x , y , and z , respectively. Assuming column-wise vectorization of a 3D matrix of size $N_y \times N_x \times N_z$, which represents the 3D image, the gradient of \mathbf{x} at position $n \in [1, \dots, N]$ is given by

$$[\mathbf{D}\mathbf{x}]_n = \begin{pmatrix} [\mathbf{D}_x\mathbf{x}]_n \\ [\mathbf{D}_y\mathbf{x}]_n \\ [\mathbf{D}_z\mathbf{x}]_n \end{pmatrix} = \begin{pmatrix} \frac{x_{n+N_y} - x_n}{\delta x} \\ \frac{x_{n+1} - x_n}{\delta y} \\ \frac{x_{n+N_x N_y} - x_n}{\delta z} \end{pmatrix}, \quad (\text{A.14})$$

with appropriate boundary conditions (periodization, Neumann boundary conditions, etc.). The constants δx , δy , and δz denote sampling intervals along x , y , and z directions, respectively. Practical implementations of TV, often assume uniform sampling by setting $\delta x = \delta y = \delta z$.

The anisotropic TV regularizer (A.12) can be interpreted as a sparsity-promoting ℓ_1 -penalty on the image gradient, while its isotropic counterpart (A.13) as an ℓ_1 -penalty on the *magnitudes* of the image gradient, which can also be viewed as a penalty promoting joint-sparsity of the gradient components. By promoting signals with sparse gradients, TV minimization recovers images that are piecewise-smooth, which means that they consist of smooth regions separated by sharp edges. Isotropic TV regularizer (A.13) is rotation invariant, which makes it preferable in the context of image reconstruction.

One must note that similar to other regularization schemes, there is, unfortunately, no theoretically optimal way of setting τ ; its optimal value might depend on a number of parameters including the sample, forward model, and noise. Generally, higher levels of τ imply stronger regularization during the reconstruction and the optimal value of τ , in our experiments, was in the range $[10^{-2}, 10^1]$ for the configurations considered.

Algorithm 3 FISTA

input: light-field data $\{\mathbf{y}^\ell\}_{\ell \in [1 \dots L]}$, initial guess $\hat{\mathbf{x}}^0$, step $\gamma > 0$, and regularization parameter $\tau > 0$.
set: $t \leftarrow 1, \mathbf{s}^0 \leftarrow \hat{\mathbf{x}}^0, q_0 \leftarrow 1$
repeat
 $\mathbf{z}^t \leftarrow \mathbf{s}^{t-1} - \gamma \nabla \mathcal{D}(\mathbf{s}^{t-1})$
 $\hat{\mathbf{x}}^t \leftarrow \text{prox}_{\mathcal{R}}(\mathbf{z}^t, \gamma \tau)$
 $q_t \leftarrow \frac{1}{2} \left(1 + \sqrt{1 + 4q_{t-1}^2} \right)$
 $\mathbf{s}^t \leftarrow \hat{\mathbf{x}}^t + ((q_{t-1} - 1)/q_t)(\hat{\mathbf{x}}^t - \hat{\mathbf{x}}^{t-1})$
 $t \leftarrow t + 1$
until stopping criterion
return estimate of the refractive index $\hat{\mathbf{x}}^t$

Algorithm 4 FGP for evaluating $\mathbf{x} = \text{prox}_{\mathcal{R}}(\mathbf{z}, \tau)$.

input: $\mathbf{z} \in \mathbb{R}^N, \tau > 0$.
set: $t \leftarrow 1, \mathbf{d}^0 \leftarrow \mathbf{g}^0, q_0 \leftarrow 1, \gamma \leftarrow 1/(12\tau)$
repeat
 $\mathbf{g}^t \leftarrow \text{proj}_{\mathcal{G}}(\mathbf{d}^{t-1} + \gamma \mathbf{D}(\text{proj}_{\mathcal{X}}(\mathbf{z} - \tau \mathbf{D}^T \mathbf{d}^{t-1})))$
 $\mathbf{x}^t = \text{proj}_{\mathcal{X}}(\mathbf{z} - \tau \mathbf{D}^T \mathbf{g}^t)$
 $q_t \leftarrow \frac{1}{2} \left(1 + \sqrt{1 + 4q_{t-1}^2} \right)$
 $\mathbf{d}^t \leftarrow \mathbf{g}^t + ((q_{t-1} - 1)/q_t)(\mathbf{g}^t - \mathbf{g}^{t-1})$
 $t \leftarrow t + 1$
until stopping criterion
return \mathbf{x}^t

A.3.2 Minimization of TV

Fast iterative shrinkage/thresholding algorithm (FISTA), summarized in Algorithm 3, is one of the most popular approaches for solving (4.5). FISTA relies on the efficient evaluation of the gradient $\nabla \mathcal{D}$ and of the proximal operator (4.16). Time-reversal scheme, in Algorithm 1, makes application of FISTA straightforward for solving (4.5) with regularizers that admit closed form proximal operators such as ℓ_1 -penalty. However, some regularizers including TV do not have closed form proximals and require an additional iterative algorithm for solving (4.16).

In our implementation, we solve (4.16) with the dual approach that was proposed by Beck and Teboulle in [8]. The approach, summarized in Algorithm 4, is based on iterative solving of the dual optimization problem

$$\hat{\mathbf{g}} = \arg \min_{\mathbf{g} \in \mathcal{G}} \{ \mathcal{Q}(\mathbf{g}) \}, \quad (\text{A.15})$$

where

$$\mathcal{Q}(\mathbf{g}) \triangleq -\frac{1}{2}\|\mathbf{z} - \tau\mathbf{D}^T\mathbf{g} - \text{proj}_{\mathcal{X}}(\mathbf{z} - \tau\mathbf{D}^T\mathbf{g})\|_{\ell_2}^2 \quad (\text{A.16})$$

$$+ \frac{1}{2}\|\mathbf{z} - \tau\mathbf{D}^T\mathbf{g}\|_{\ell_2}^2. \quad (\text{A.17})$$

Given the dual iterate \mathbf{g}^t , the corresponding primal iterate can be computed as

$$\mathbf{x}^t = \text{proj}_{\mathcal{X}}(\mathbf{z} - \tau\mathbf{D}^T\mathbf{g}^t). \quad (\text{A.18})$$

The operator $\text{proj}_{\mathcal{X}}$ represents an orthogonal projection onto the convex set \mathcal{X} . For example, a projection onto N -dimensional cube

$$\mathcal{X} \triangleq \left\{ \mathbf{x} \in \mathbb{R}^N : a \leq x_n \leq b, \forall n \in [1, \dots, N] \right\}, \quad (\text{A.19})$$

with bounds $a, b > 0$, is given by

$$[\text{proj}_{\mathcal{X}}(\mathbf{x})]_n = \begin{cases} a & \text{if } x_n < a \\ x_n & \text{if } a \leq x_n \leq b \\ b & \text{if } x_n > b, \end{cases} \quad (\text{A.20})$$

for all $n \in [1, \dots, N]$.

The set $\mathcal{G} \subseteq \mathbb{R}^{N \times 3}$ in (A.15) depends on the variant of TV used for regularization. For anisotropic TV (A.12), the set corresponds to

$$\mathcal{G} \triangleq \{\mathbf{g} \in \mathbb{R}^{N \times 3} : \|[\mathbf{g}]_n\|_{\ell_\infty} \leq 1, \forall n \in [1, \dots, N]\} \quad (\text{A.21})$$

with the corresponding projection

$$[\text{proj}_{\mathcal{G}}(\mathbf{g})]_n = \begin{pmatrix} \frac{[\mathbf{g}_x]_n}{\max(1, |[\mathbf{g}_x]_n|)} \\ \frac{[\mathbf{g}_y]_n}{\max(1, |[\mathbf{g}_y]_n|)} \\ \frac{[\mathbf{g}_z]_n}{\max(1, |[\mathbf{g}_z]_n|)} \end{pmatrix}, \quad (\text{A.22})$$

for all $n \in [1, \dots, N]$. Similarly, for isotropic TV (A.13), the set corresponds to

$$\mathcal{G} \triangleq \{\mathbf{g} \in \mathbb{R}^{N \times 3} : \|[\mathbf{g}]_n\|_{\ell_2} \leq 1, \forall n \in [1, \dots, N]\} \quad (\text{A.23})$$

with the corresponding projection

$$[\text{proj}_{\mathcal{G}}(\mathbf{g})]_n = \frac{[\mathbf{g}]_n}{\max(1, \|[\mathbf{g}]_n\|_{\ell_2})}, \quad (\text{A.24})$$

for all $n \in [1, \dots, N]$.

While the theoretical convergence of FISTA requires the full convergence of inner Algorithm 4, in practice, it is sufficient to run about 5-10 iterations with an initializer that corresponds to the dual variable from the previous outer iteration. In our implementation, we thus fix the maximal number of inner iterations to $t_{\text{in}} = 10$ and enforce an additional stopping criterion based on measuring the relative change of the solution in two successive iterations as $\|\mathbf{g}^t - \mathbf{g}^{t-1}\|_{\ell_2} / \|\mathbf{g}^{t-1}\|_{\ell_2} \leq \delta_{\text{in}}$, where $\delta_{\text{in}} = 10^{-4}$ in all the experiments here.

A.4 Bibliography

- [1] W. Choi, C. Fang-Yen, K. Badizadegan, S. Oh, N. Lue, R. R. Dasari, and M. S. Feld, "Tomographic phase microscopy," *Nat. Methods*, vol. 4, (2007): 717-719.
- [2] K. Kim, H. Yoon, M. Diez-Silva, M. Dao, R. R. Dasari, and Y. Park, "High-resolution three-dimensional imaging of red blood cells parasitized by *Plasmodium falciparum* and in situ hemozoin crystals using optical diffraction tomography," *J. Biomed. Opt.*, vol. 19, p. 011005, 2014
- [3] J. W. Goodman, "*Introduction to Fourier Optics*," 2nd ed. McGraw-Hill, 1996.
- [4] M. D. Feit and J. A. Fleck, "Beam nonparaxiality, filament formation, and beam breakup in the self-focusing of optical beams," *J. Opt. Soc. Am. B*, vol. 5, no. 3, pp. 633–640, March 1988.
- [5] B. Saleh and M. Teich, "*Fundamentals of Photonics*," 2nd ed. John Wiley & Sons, 2007.
- [6] A. Goy, "Imaging and microscopy in linear and nonlinear media using digital holography," Ph.D. dissertation, École polytechnique fédérale de Lausanne, January 2013, thesis number 5617.
- [7] R. Gilmore, "Baker-Campbell-Hausdorff formulas," *J. Math. Phys.*, vol. 15, pp. 2090–2092, 1974.
- [8] A. Beck and M. Teboulle, "Fast gradient-based algorithm for constrained total variation image denoising and deblurring problems," *IEEE Trans. Image Process.*, vol. 18, no. 11, pp. 2419–2434, November 2009.



Morteza Hasani Shoreh

Birth: 9th of Jan. 1988, Iran
 Avenue de la poste 27, 1020 Renens,
 VD, Switzerland,
 Phone: (+41)787476145,
 Email: morteza.hasanishoreh@epfl.ch

Education:

- PhD Candidate in Photonics, **École Polytechnique Fédérale de Lausanne (EPFL)**, Switzerland, (2015- now) (will be graduated by the end of June), thesis entitled as; "**3D Reconstruction of Optical Diffraction Tomography Based on a Machine Learning Neural Network Model.**"
- Ms. in Optical Communication Systems, **Sharif University of Technology**, Tehran, Iran (2010-2013), thesis entitled as; "**Study and Performance Evaluation of Nonlinear Compensation Methods in Coherent Optical OFDM Systems.**"

Honors and Awards:

- **Ranked 8th/ 30,000 (Electrical Engineering)** National M.S. Studies Entrance Exam, 2010
- Fellowship from **Sharif University of Technology** for graduate studies
- **Ranked 167th/ 400,000 (Mathematics)** Nationwide University Entrance Exam, 2006
- Fellowship from **University of Tehran** for undergraduate studies
- Runner-up in the last stage of nationwide **Physic Olympiad**. 2004
- Runner-up in the last stage of nationwide **Math Olympiad**. 2004

Research Interests:

- **Imaging Optics, 3D Tomographic Reconstructions, 3D video reconstruction of cell cultures**
- **Machine learning, deep learning algorithms and implementations**
- **Linear and nonlinear Optimization, Invers-problems, computational methods**
- **Coding and computer simulation of experimental works (MATLAB), Hardware interface coding (Labview)**

Selected Publications:

- Ulugbek S. Kamilov, Ioannis N. Papadopoulos, **Morteza H. Shoreh**, Alexandre Goy, Cedric Vonesch, Michael Unser, and Demetri Psaltis, "Learning approach to optical tomography," *Optica* 2, 517-522 (2015)
- Ulugbek S. Kamilov, Ioannis N. Papadopoulos, **Morteza H. Shoreh**, Alexandre Goy, Cedric Vonesch, Michael Unser, and Demetri Psaltis, "Optical Tomographic Image Reconstruction Based on Beam Propagation and Sparse Regularization," in *IEEE Transactions on Computational Imaging*, vol. 2, no. 1, pp. 59-70, March 2016
- **Morteza H. Shoreh**, A. Goy, J. Lim, U. Kamilov, M. Unser, and D. Psaltis. "Imaging cell clusters and tissue using learning tomography." In *Optical Methods for Inspection, Characterization, and Imaging of Biomaterials III*, vol. 10333, p. 1033306. *International Society for Optics and Photonics*, 2017.
- **Morteza H. Shoreh**, Alexandre Goy, JooWon Lim, Ulugbek Kamilov, Michael Unser, and Demetri Psaltis. "Optical Tomography based on a nonlinear model that handles multiple scattering." In *Acoustics, Speech and Signal Processing (ICASSP), 2017 IEEE International Conference on*, pp. 6220-6224. IEEE, 2017.
- H. Qiao, J. Wu, X. Li, **Morteza H. Shoreh**, J. Fan, and Q. Dai. "GPU-based deep convolutional neural network for tomographic phase microscopy with l₁ fitting and regularization." *Journal of Biomedical Optics* 23, no. 6 (2018): 066003.
- Lim, JooWon, Alexandre Goy, **Morteza H. Shoreh**, Michael Unser, and Demetri Psaltis. "Assessment of learning tomography using Mie theory." *arXiv preprint arXiv:1705.10410* (2017).
- Ulugbek S. Kamilov, Ioannis N. Papadopoulos, **Morteza H. Shoreh**, Demetri Psaltis, and Michael Unser, "Isotropic inverse-problem approach for two-dimensional phase unwrapping," *J. Opt. Soc. Am. A* 32, 1092–1100 (2015).
- **Morteza H. Shoreh**, "Compensation of Nonlinearity Impairments in Coherent Optical OFDM Systems Using Multiple Optical Phase Conjugate Modules," *J. Opt. Commun. Netw.* 6, 549-558 (2014)
- **Morteza H. Shoreh**, Ahmad Fallahpour, and Jawad A. Salehi, "Design Concepts and Performance Analysis of Multicarrier CDMA for Indoor Visible Light Communications," *J. Opt. Commun. Netw.* 7, 554-562 (2015).
- **Morteza. H. Shoreh**, H. Hosseinianfar, F. Akhouni, E. Yazdian, M. Farhang and J. A. Salehi, "Design and Implementation of Spectrally-Encoded Spread-Time CDMA Transceiver," in *IEEE Communications Letters*, vol. 18, no. 5, pp. 741-744, May 2014.
- **Morteza H. Shoreh**, Hamzeh Beyranvand, and Jawad A. Salehi. "Performance evaluation of asynchronous multi-carrier code division multiple access for next-generation long-reach fibre optic access networks." *IET Optoelectronics* 9.6 (2015): 325-332.

Selected Research Experience:

Optics Laboratory, École Polytechnique Fédérale de Lausanne, (April 2015 – June. 2018), 3D Reconstruction of Optical Coherence Tomography Based on a Machine Learning Neural Network Model, Under Supervision of **Prof. Demetri Psaltis** (PhD studies), mainly on the following topics:

- **3D Reconstruction of Optical Coherence Tomography Based on Machine Learning Neural Network Model**
- **Structured Illumination Tomography implementation and Machine Learning based 3D Reconstruction**
- **Systematic experiments presenting success of our proposed method on multiple scattering scenarios.**
- **3D reconstruction of artificially build multiple layered cells to illustrate the proposed method benefits.**
- **Reconstruction of 3D movies of cells dividing and apoptosis procedures.**

Optics Laboratory, École Polytechnique Fédérale de Lausanne, (Sep.2014 – Mar. 2015), Tomographic Reconstruction Using Iterative Algorithms, Under Supervision of **Prof. Demetri Psaltis** (as Internship),

Optical Network Research Laboratory (ONRL), Sharif University of Technology (Sep.2011-Sep.2014), under supervision of **Prof. Jawad A. Salehi** (as Research Assistant), mainly on the following topics:

- **Optical OFDM and Multicarrier-CDMA Modulations**
- **Laboratory LAN Access Providing via Visible Light**
- **Fiber Optics, Nonlinear Impairments and Nonlinearity Compensation Methods**

Active Optical Devices Laboratory (AODL), Shahid Beheshti University (Jun.2012- Sep.2014), working on Optical Testing Devices, Under Supervision of **Prof. Ezodin Mohajerani** (as Technical Manager), mainly on the following topics:

- **Teaching Testing Methods to Undergraduate Students**
- **Designing Active Optical Devices Tests**

Selected Graduate Courses:

- | | |
|--|---|
| • Advanced biomedical imaging methods & instrumentation | • Convex Optimization |
| • Nonlinear fiber optics | • Optical Simulation Methods |
| • Optical waves propagation | • Machine learning algorithms |
| • Photonics for Engineers | • Introduction to Fourier Optics |
| • Machine Vision | • Image processing I, II |

Key Skills:

- | | |
|---|---|
| • Experienced in cell culture, microscopy, biomedical optics and tomography | • Hard working, able to handle pressure |
| • Super strong mathematical and physics background | • Resourceful and management skills |
| • Super-fast learner, self-motivated, enthusiastic | • Strong teaching abilities and patient educator |
| • Strong social communication and team playing | • Self-organization, responsibility and multi-tasking |
| • strong in coding and computational works | • Strong team leading experience and self confidence |
| • Experienced in deep learning, Inverse problems and algorithms | • Easily adopting to new situation, adventurous |

Computer Skills:

- | | |
|-------------------|---------------|
| • MATLAB | • C++ |
| • Lab View | • Java |
| • Python | |

Language Skills:

- | | |
|-------------------------------------|----------------------------------|
| • English : Fluent (C2) | • Italian : beginner (A1) |
| • French : Advance (B2) | • Arabic : Intermediate |
| • German : Intermediate (B1) | • Persian : Native |

Hobbies and Interests:

- | | |
|---|----------|
| • Swimming | • Chess |
| • Playing Guitar | • skiing |
| • Hiking and Camping in nature especially in mountains or river banks | |

References:

- **Prof. Demetri Psaltis**, Professor of Optics, Dean of Engineering, École Polytechnique Fédérale de Lausanne, Switzerland, Tel: +41 21 69-37795, Email: demetri.psaltis@epfl.ch
- **Prof. Michael Unser**, Professor and Director of Biomedical Imaging Group, École Polytechnique Fédérale de Lausanne, Switzerland, Tel: +41 21 693 11 85, Email: michael.unser@epfl.ch
- **Prof. Javad A. Salehi**, Electrical Engineering Department, Sharif University of Technology, Tehran, Iran Tel: +98 21 66164334, Email: jasalehi@sharif.edu
- **Prof. Ezodin Mohajerani**, Laser And Plasma Research Institute, Shahid Beheshti University, Tehran, Iran, Tel: +98 21 2990 2598, Email: e-mohajerani@sbu.ac.ir